Analytical and Computational Modeling of Interfacial Properties and Nucleation Process in Methane Hydrates Materials

Sina Mirzaeifard
Department of Chemical Engineering
McGill University, Montreal

October 2019

A thesis submitted to McGill University in partial fulfillment of the requirements of the degree of Doctor of Philosophy

Dedication

To my lovely parents, Mohammad Hassan Mirzaeifard and Farkhondeh Hamidi
The ones who have wholeheartedly supported me since when I took my very first breath in this world

Contributions of the Authors

The author chooses the manuscript-based thesis option following the guidelines stipulated by the Faculty of Graduate and Postdoctoral Studies:
https://www.mcgill.ca/gps/thesis/guidelines/preparation

The contents of Chapters 2-5 of the present thesis are adopted from articles published in or to-be submitted to scientific journals under the normal supervision of my research supervisor, Prof. Alejandro D. Rey, and co-supervisor, Prof. Phillip Servio, who are also co-authors. All the theoretical and computational work described in this thesis has been done by the present author.

Acknowledgements

I would like to candidly thank my both supervisors, Prof. Alejandro D. Rey and Prof. Phillip Servio, for all their technical and emotional supports, insights, and dedications during my PhD program. Without their guidance, my research and dissertation would not have been possible. I was pleased and honored to work under their great supervisions. During this period, I had the opportunity to learn a lot from their enthusiasm towards exploring new ideas, determination to work to the highest quality, and kindness and patience. Moreover, I truly appreciate their valuable time they spent reviewing my work.

I am thankful to financial supports from the McGill Engineering Doctoral Award (MEDA) program, the James McGill Professorship appointment (ADR), and Natural Science and Engineering Research Council of Canada (NSERC). I am also grateful to Compute Canada and Calcul Québec for the access to the supercomputers Graham and Cedar.

I take this opportunity to thank my present and past fellows in the Materials Modeling Research Group (MMRG): Samuel Mathews, Ziheng Wang, Shaden Daghash, Jonathan Monahan, Pardis Rofouieeraghi, Zeina Jendi, Oscar Aguilar Gutiérrez, Mahdi Roohnikan, Hang Hu, Estela Mayoral, Emilio Herrera Valencia, and Isaak Daniels, for providing a warm and friendly workplace. I am especially grateful to Sayyed Ahmad Khadem, Oscar Matus Rivas, and Thomas Vlasic for all the great conversations and insightful discussions during these three years. In addition to our group, I cannot forget the unending and timely help received from the people in the Wong building: Lou, Kevin, Louise, Anna, and Lisa.

Last but not least, I wish to express my deepest gratitude to my compassionate father Hassan, my sweet mother Farkhondeh, my lovely sister Sara, and my happy brother-in-law Alireza for their continued support, endless love, encouragement, confidence in me, regardless of geographical distance. In particular, my beautiful niece Bahar who brought great joy and love to my life with her birth during my study. I would also like to thank my close friends: Masih Aminbeidokhti, Iman Bagheri, and Negin Esmaeili who helped me both intellectually and emotionally during my PhD program. Special thanks to Rafooneh Jafarian Bahri, who persuaded me to apply to McGill and choose Montreal, Canada as my next stop in life.

However I could write a thesis only on the acknowledgement section to thank the people who have blessed me and shaped my life, I stop here and will leave room for the dissertation.

Abstract

Solutions of liquid water and methane gas at low temperatures and high pressures lead to the nucleation and growth of ice-like methane hydrates crystals. The formation might occur in the solution's bulk or at the solution-gas or solution-substrate interface, thus evolving into different material morphologies. Since the experimental techniques are largely unable to explain such nanoscale stochastic phenomena, a complete material characterization and molecular-scale understanding of probable formation sites and morphologies is required to inhibit or promote crystallization depending on the particular application or process objective. Therefore, we use accurate and efficient computational simulations in combination with analytical theory to calculate the interfacial tension and supersaturation as the main factors in methane hydrate formation process according to the classical nucleation theory (CNT). We employ deterministic molecular dynamics (MD) techniques to obtain thermodynamic and mechanical properties in order to analyze the bulk and interfacial phenomena in the most important mixtures: water-methane gas, water-methane hydrate, and methane hydrate-gas. We report the interfacial tension at all possible interfaces in the solutions, and explore the crucial effects of temperature and pressure on the interface physics using descriptors such as the hydrogen bonding, charge distribution, molecular structure and orientation, and composition.

We find that the interfacial tension at water-gas interface decreases with temperature, while the tension at hydrate-water interface increases with temperature. The effect of temperature on hydrate-gas interface is infinitesimal. The pressure change follows the classical thermodynamic behavior so that the interfacial tension of all these interfaces decreases with pressure. We calculate the methane hydrate nucleation work from the supersaturation and interfacial tension dataset, conclude that the formation forms in the ranked order of film-shaped, cap-shaped, lens-shaped, and homogeneous. We postulate that the presence of an intermediate liquid-like layer at the hydrate-gas interface works in favor of the formation at the liquid-gas interface compared to the solution's bulk. However, a negligible difference in the interfacial energy contribution between lens-shaped and homogeneous formations specifies that the high concentration of gas and water molecules at the interface is the main reason underlying the lens-shaped clustering in the formation process of methane hydrates.

Résumé

Les solutions d'eau liquide et de gaz méthane à basse température et à haute pression conduisent à la nucléation de cristaux d'hydrates de méthane de type glace. La formation peut se produire dans la masse de la solution ou à l'interface solution-gaz ou solution-substrat, évoluant dans différentes morphologies. Comme les techniques expérimentales ne permettent pas d'expliquer ces phénomènes stochastiques à l'échelle nanométrique, une caractérisation complète des matériaux et une compréhension à l'échelle moléculaire des sites de formation et des morphologies probables sont nécessaires pour inhiber ou favoriser la cristallisation selon l'application. Par conséquent, nous utilisons des simulations informatiques en combinaison avec la théorie analytique pour calculer la tension interfaciale et la sursaturation comme principaux facteurs dans le processus de formation des hydrates de méthane selon la théorie classique de nucléation. Nous utilisons des techniques de dynamique moléculaire déterministe pour obtenir des propriétés thermodynamiques et mécaniques afin d'analyser les phénomènes volumiques et interfaciaux dans différents mélanges: gaz eau-méthane, hydrate d'eau-méthane et gaz-hydrate de méthane. Nous signalons la tension interfaciale à toutes les interfaces possibles dans les solutions et explorons l'effet de la température et de la pression sur l'interface en ce qui concerne la liaison hydrogène, la distribution des charges, la structure moléculaire, l'orientation et la composition.

Nous constatons que la tension interfaciale à l'interface eau-gaz diminue avec la température, tandis que la tension à l'interface hydrate-eau augmente avec la température. L'effet de la température sur l'interface hydrate-gaz est infime. Le changement de pression suit le comportement thermodynamique classique de sorte que la tension interfaciale de toutes ces interfaces diminue avec la pression. Nous calculons le travail de nucléation des hydrates de méthane à partir des données de sursaturation et de tension interfaciale et concluons que la formation se forme dans l'ordre suivant: en forme de film, en forme de bouchon, en forme de lentille, et homogène. Nous postulons que la présence d'une couche intermédiaire de type liquide à l'interface hydrate-gaz favorise la formation à l'interface liquide-gaz par rapport au volume de la solution. Cependant, une différence négligeable dans la contribution énergétique interfaciale entre les formations en forme de lentille et les formations homogènes spécifie que la concentration élevée de molécules de gaz et d'eau à l'interface est la principale raison sous-jacente au regroupement en forme de lentille dans le processus de formation des hydrates de méthane.

Table of Contents

Chapter 1. General Introduction 1

1.1. Thesis Motivation 2

1.2. Background and Literature Review 5

1.2.1. Gas Hydrate Structures 5

1.2.2. Gas Hydrate Formation 7

1.2.3. Modeling and Simulation 16

1.3. Thesis Objectives 19

1.4. Thesis Organization 20

1.5. References 22

Chapter 2. Molecular Dynamics Characterization of Temperature and Pressure Effects on the Water-Methane Interface 28

2.1. Preface 29

2.2. Abstract 29

2.3. Keywords 29

2.4. Introduction 29

2.5. Model and Simulation Methods 33

2.6. Results and Discussion 37

2.7. Conclusions 45

2.8. Acknowledgements 45

2.9. References 46

Chapter 3. Molecular Dynamics Characterization of the Water-Methane, Ethane, and Propane Gas Mixture Interfaces 50

3.1. Preface 51

3.2. Abstract 51

3.3. Keywords 52

3.4. Introduction 52

3.4.1. Motivation 53

3.4.2. Computational Challenges 55

3.5. Model and Simulation Methods 57
3.6. Results and Discussion 61
3.7. Conclusions 73
3.8. Acknowledgements 74
3.9. References 74

Chapter 4. Modeling and Simulation of Water and Methane Hydrate Crystal Interface... 80

4.1. Preface 81
4.2. Abstract 81
4.3. Keywords 81
4.4. Introduction 82
4.5. Methodology 85
  4.5.1. Model and Computational Methods 85
  4.5.2. Interfacial Tension 87
4.6. Results and Discussion 88
4.7. Conclusions 98
4.8. Acknowledgments 99
4.9. References 99

Chapter 5. Characterization of Nucleation of Methane Hydrate Crystals: Interfacial Theory and Molecular Simulation 107

5.1. Preface 108
5.2. Abstract 108
5.3. Keywords 109
5.4. Introduction 109
  5.4.1. Motivation 111
5.5. Methodology 113
  5.5.1. Model 114
  5.5.2. Simulation 116
  5.5.3. Analytical Theory 117
5.6. Results and Discussion 119
5.7. Summary and Conclusions 133
5.8. Acknowledgements 135

5.9. References 135

Chapter 6. Conclusions and Contributions to Original Knowledge 143

6.1. Conclusions 144

6.1.1. Molecular Dynamics Characterization of Temperature and Pressure Effects on the Water-Methane Interface 144

6.1.2. Molecular Dynamics Characterization of the Water-Methane, Ethane, and Propane Gas Mixture Interfaces 145

6.1.3. Modeling and Simulation of Water and Methane Hydrate Crystal Interface 146

6.1.4. Characterization of Nucleation of Methane Hydrate Crystals: Interfacial Theory and Molecular Simulation 147

6.2. Contributions to Original Knowledge 149

6.3. Recommendations for Future Works 150

List of Figures

Figure 1.1. Schematic of a methane hydrate. Circles and lines are representative of atoms and chemical bonds, respectively [11]. 2

Figure 1.2. Removing a gas hydrate plug from a pipeline [4]. 3

Figure 1.3. Gas hydrates resource map. Filled and open circles show inferred and recovered resources, respectively, in global distribution of gas hydrate deposits [4]. 4

Figure 1.4. Visualization the various gas hydrates structures and geometries. Atoms shown by points are connected together by hydrogen bonds to form repeating crystal structures of water cages for gas hydrate structures sI, sII, and sH [4]. 7

Figure 1.5. Conceptual gas consumption diagram for hydrate formation [1]. 8

Figure 1.6. Schematic model of hydrate nucleation. Guest molecules (filled black circles) encompassed by water cages agglomerate to form hydrate clusters [1]. 9

Figure 1.7. Schematic of crystal growth of gas hydrates. Clusters are attached to the hydrate interface. Guest molecules (black circles) join the surface and water molecules (gray circles) can either join or diffuse away [1]. 10

Figure 1.8. Morphology of gas hydrate at the liquid-gas interface in different subcooling conditions [20]. 11

Figure 1.9. Mechanism of the hydrate shell growth around a water droplet. Hydrate formation begins with a thin porous shell around the droplet. The shell thickens until the entire droplet turns into a hydrate compound [1]. 11

Figure 1.10. Schematic nucleation theory of gas hydrates in the solution (left), the substrate-solution interface (middle), the solution-gas interface (right) [33]. 13

Figure 1.11. Gas hydrate stability region with and without the presence of the thermodynamic inhibitor in a submerged oil and gas pipeline [4]. 15

Figure 1.12. Thesis organization chart connecting the objectives and chapters 2-5. 21

Figure 2.1. (a) Schematic showing one grey zone containing the water molecules and two white zones containing the methane molecules to form the liquid and gas phases, respectively. (b) Initial configuration of the system. The green, red, and white particles represent the methane molecules, the oxygen atoms, and the hydrogen atoms, respectively. Two brown regions represent the interfaces between the liquid and gas phases. 35

Figure 2.2. Choosing different size for the slabs changes the difference of the normal and tangential pressures (reported in units of mN/m^2). This change might even lead to unreliable surface tension values. Blue and black lines represent the simulations with the slab lengths of 0.1Å and 6Å (as example) in the z dimension, respectively. The pressure of the system is 10 MPa and the temperatures are 25^oC (a) and 105^oC (b). In addition, the blue line in plot (b) clearly shows how increasing temperature damps the two negative edge peaks associated with compression [30,32]. 38

Figure 2.3. The plots depict the values for the local density (g/cm^3) of the water (a) and methane (b) molecules at the interface versus the temperature (^oC) of the system. When the system is exposed to a temperature upturn, a sudden decrease is observed for the local density of both components, especially in the systems with higher pressure regime (>30 MPa). 39

Figure 2.4. Surface tension (mN/m) at the temperature of 25^oC with increasing the system pressure (MPa). The plus sign, triangle, circle, and square markers denote the data obtained from the experiments by Sachs et al. and Sun et al., simulation, and present work (with blue fitting curve), respectively [36-38]. 40

Figure 2.5. Increasing the temperature reveals an increase in interfacial thickness *t* (a) and, more effectively, L_z (b) at 10, 20, 30, 40, and 50 MPa. The systems at higher temperatures better manifest the box length elongation. 41

Figure 2.6. The plot (a) depicts the inverse behavior of the interfacial tension (mN/m) versus temperature (^oC). Blue and red lines in the plot (b) display the linear and quadratic master curves, respectively, which fit the interfacial tension at 10 MPa and different temperatures (K) and whose slopes estimate the surface entropy 42

Figure 2.7. Water (solid line) and methane (dashed line) mass fractions. The pressure and temperature are subject to change in the plots (a) and (b), respectively. The system temperature for the plot (a) is 25^oC. Blue and red lines denote the pressure of 10 and 50 MPa, respectively. Increasing the water mass fraction, consequently, decreasing the methane mass fraction in the liquid phase exhibits a dramatic decrease in the potential energy and increase in the hydrogen bond quantity at the interface as shown in the insets. Dashed line in the inset (a) represents the interface center obtained from the inflection point of fitted density profiles. Blue and red lines in the plot (b) denote the temperature of 25^oC and 105^oC at 10 MPa, respectively. The insets demonstrate how the mass fractions remain constant in the liquid phase but slightly change in the gas phase

when the system experiences a temperature difference so that the water molecules might enter the gas phase more frequently at high-temperature regime. 44

Figure 3.1. (a) Introducing different clathrate formation processes. γ is the interfacial tension of the homogeneous formation of gas hydrates. γlg, γhg, and γlh denote the interfacial tension between the liquid-gas phases, the hydrate-gas phases, and the liquid-hydrate phases, respectively. In this work, we study γlg where the liquid is water. (b) Geometric configuration of structure II hydrates alongside a snapshot of propane hydrate. The purple, red, and white particles denote the propane molecules, the oxygen atoms, and the hydrogen atoms, respectively. The blue dashed lines represent the hydrogen bonding network. 54

Figure 3.2. (a) Schematic showing the water and gas molecules in grey and white zones to represent the liquid and gas phases, respectively. (b) Snapshot of the initial configuration of the system. The green, blue, purple, red, and white particles denote the methane molecules, the ethane molecules, the propane molecules, the oxygen atoms, and the hydrogen atoms, respectively. The brown regions define the interfaces separating the gas and liquid phases. 58

Figure 3.3. Local density profiles (g/cm3) of the water-gas mixture with (a) and without (b) the propane molecules near the interface at 298.15 K and 10 MPa. The triangle, circle, and square markers denote the methane, ethane, and the propane concentrations, respectively. When the system contains large hydrocarbons, the gas adsorption onto the water surface sequentially occurs from large to small molecules. Please note that the interface center is -50 Å, which is obtained from the inflection point of fitted density profiles. 62

Figure 3.4. The plot (a) shows the mass fractions of water (red), methane (green), ethane (blue), and propane (purple) molecules at 298.15 K and 10 MPa. The plot (b) enlarges the mass fractions of the gas molecules in the liquid phase to illustrate the minor solubility of the methane molecules and the infinitesimal penetrations of the ethane and propane molecules inside the liquid water phase. Please note that the centers of the left and right interfaces are -50 Å and 62 Å, respectively, which are obtained from the inflection points of fitted density profiles. 64

Figure 3.5. Potential energy (kcal/mol) of a system at 298.15 K and 10 MPa. As the mass fraction of the gas molecules decreases, consequently, the water mass fraction increases so that the system reveals a dramatic decrease in its local potential energy. 65

Figure 3.6. Radial pair distribution functions of the system at (a) 298.15 K and (b) 275.15 K, and 10 MPa. The plots present the multilayer adsorption of gas molecules onto the water surface. The adsorption enhances once the system experiences lower temperature as shown in the plot (b)... 66

Figure 3.7. The plot (a) depicts the hydrogen bond quantity at the interface. The plus sign and circle markers represent the water-methane mixture and the water-natural gas mixture, respectively. Dashed line defines the interface center obtained from the inflection point of fitted density profiles. The plot shows that the presence of large hydrocarbons consolidates the interfacial hydrogen bonding. The temperature of the system is subject to change in the plot (b) to show the hydrogen bonding network near the interface is intensified in lower temperature regimes. The plus sign and circle markers denote the temperature of 275.15 K and 298.15 K, respectively. 67

Figure 3.8. Interfacial tension (mN/m) of the water-natural gas mixture with increasing the system pressure (MPa) at the temperature of 293.15 K (a) and 298.15 K (b). The plot (c) shows the interfacial tension of the water-pure methane mixture at 298.15 K [54]. The square and plus sign markers represent the data obtained from the experiments by Hayama *et al.* and present work (with blue fitting curve), respectively [29]. The plots explicitly demonstrate that the interfacial tension decreases when the system is exposed to a pressure upturn, especially in the systems in the lower pressure regime (< 10 MPa)... 69

Figure 3.9. The temperature upturn triggers an increase in the physical interfacial thickness *d* (a) and L_z (b) at 10, 20, 30, 40, and 50 MPa represented by plus sign, circle, star, square, and triangle markers, respectively. High temperature regime further manifests the elongation of the box length. 71

Figure 3.10. The plot (a) displays the inverse behavior of the interfacial tension (mN/m) with the temperature (K) upturn at 10 (plus signs), 20 (circles), 30 (stars), 40 (squares), and 50 (triangles) MPa. Blue line in the plot (b) depicts the linear master curves fitting the interfacial tension at 10 MPa. The slope of this line is the surface entropy. 72

Figure 4.1. Schematic of water/hydrate interfaces under different nucleation conditions. γ denotes the interfacial tension of this interface. 83

Figure 4.2. Simulation template showing the red, white, and green particles as oxygen atoms, hydrogen atoms, and methane molecules, respectively. The brown regions on both sides denote the interfacial zones, which separate the liquid and crystal phases. 86

Figure 4.3. Local density profiles (g/cm^3) of the water-methane hydrate mixture along the simulation box at 10 MPa and different temperatures. The plus sign, circle, star, cross, square, diamond, and triangle markers represent the system temperatures of 271, 273, 275, 277, 279, 281, and 283 K, respectively.......... 88

Figure 4.4. Potential energy (kcal/mol) of the system along the z direction at 10 MPa and 275 K. The potential exhibits a sudden upturn from the liquid water phase to the methane hydrate crystal phase. 89

Figure 4.5. Representative pressure oscillations of the methane hydrate-liquid water mixture at 10 MPa and 275 K. In (a), the blue line shows the measured pressure without a damping constant or averaging method. The red line represents the pressure for a system with the use of sufficient damping constant and moving average method. In (b), there is a depiction the intense pressure fluctuations when a short slab length is used. The blue and red represent the local pressure with slab lengths of 0.5 and 12 Å, respectively. 90

Figure 4.6. Different slab lengths change the difference between the normal and tangential pressures multiplied by the unit length. The temperature of the system is 275 K, and the pressure is 10 MPa. Red plus signs, green circles, purple stars, and black squares represent slab lengths of 3, 6, 9, and 12 Å, respectively.......... 90

Figure 4.7. (a) Depiction of the interfacial energy decreases with the system temperature at different pressures. (b) Variation of the interfacial energy under elastic deformation. The plus sign, circle, star, square, diamond, and triangle markers represent system pressures of 5, 10, 15, 20, 25, and 30 MPa, respectively.......... 91

Figure 4.8. Interfacial tension values (mN/m) for the mixture of water and methane hydrate with increasing system temperature (a) and pressure (b). In (b) there are the results of a mixture at 275 K. The plus sign, circle, star, square, diamond, and triangle markers denote pressures of 5, 10, 15, 20, 25, and 30 MPa, respectively. The blue line presents the fitting curve for the system at 10 MPa. 92

Figure 4.9. Excess enthalpy (kcal/mol) of the system with systematic change of temperature (a) and pressure (b). The system temperature for the results shown in (b) is 275 K. The excess enthalpy increases as the temperature increases or the pressure decreases. The plus sign, circle, star, square, diamond, and triangle markers are systems with pressures of 5, 10, 15, 20, 25, and 30 MPa, respectively. 93

Figure 4.10. Interfacial excess entropy decreases as the temperature increases. The plus sign and circle markers represent the data obtained from theory and computational thermodynamics, respectively. 94

Figure 4.11. Local density profile of the water molecules demonstrates the interfacial adsorption. The molecular adsorption at the interface vanishes as the temperature increases and the pressure decreases. Please note that the interfacial center exists at z ≈ 66 Å with the liquid water phase on the left and the crystalline methane hydrate phase on the right side. The blue, red, and green lines in (a) represent system temperatures of 271, 275, and 289 K, respectively, at 10 MPa. The blue and red lines in (b) denote system pressures of 15 and 10 MPa, respectively, at 275 K. 95

Figure 4.12. (a) Radial pair distribution function between the oxygen atoms in the water bulk (the solid blue line), interface (the dashed red line), and methane hydrate bulk (the dotted green line). (b) Radial pair distribution function between the methane molecules and the oxygen atoms (the solid blue line) and the methane molecules and the hydrogen atoms (the dashed red line) at the interface. The temperature and pressure of the mixture are 275 K and 10 MPa. 96

Figure 4.13. Hydrogen bond density profiles across the simulation box averaged over 1000 configurations at equilibrium at different system temperatures (a) and pressures (b). The interfacial center exists at z ≈ 184 Å with the liquid water phase on the left and the crystalline methane hydrate phase on the right side. In (a), the plus sign, circle, and square markers represent temperatures of 271, 275, and 289 K, respectively, at 10 MPa. In (b), the circle and triangle markers denote pressures of 10 and 15 MPa, respectively, at 275 K. 97

Figure 4.14. Interfacial charge distribution in units of electron charge at different temperatures (a) and pressures (b). The center of the interface is at z ≈ 66 Å with the water and hydrate phases on the left and right sides, respectively. The blue, red, and green lines in (a) denote the mixtures at 10 MPa and temperatures of 271, 275, and 289 K, respectively. The red and blue lines in (b) represent the mixtures at 275 K and pressures of 10 and 15 MPa, respectively. The charge density profiles are enlarged in the insets to better distinguish the lines. 98

Figure 5.1. Schematics of different hydrate formation morphologies. γ represents the interfacial tension for the homogeneous (HON) formation of methane gas hydrate. γlg, γhl, γhg, γls, and γhs indicate the interfacial tension at the liquid-gas, hydrate-liquid, hydrate-gas, liquid-solid, and hydrate-solid interfaces, respectively. 111

Figure 5.2. Schematic showing the simulation template including the methane gas, water, and methane hydrate molecules to represent the gas, liquid, and hydrate phases, respectively. The red, white, and green particles denote the oxygen and hydrogen atoms, and methane molecules, respectively. 115

Figure 5.3. Characterization factor versus wetting angle with values between 0 to 180° for cap-shaped clusters. 119

Figure 5.4. The interfacial tension at different temperature (a) and pressure (b). The triangle, circle, plus sign, and square markers represent γlg, γhl, γhg, and γhg*. The interfacial energy associated with the interface between the methane hydrate and gas phases are obtained from the direct computation (γhg) and Antonow's rule (γhg*). 122

Figure 5.5. Snapshot of a mixture configuration composed of methane hydrate and gas phases. The green, red, and white particles represent the methane molecules, oxygen atoms, and hydrogen atoms, respectively. The red lines denote the hydrogen bonding between the water molecules forming the structure I methane hydrate. The transitional liquid-like phase can be readily distinguished at the methane hydrate-gas interface. 123

Figure 5.6. The plot (a) shows the charge and local density across the hydrate-gas interface at 275 K and 10 MPa to determine the quasi-liquid layer thickness. The blue and red lines represent the local density of water and methane molecules, respectively. The thickness of the intermediate quasi-liquid layer (b) formed between the methane gas and hydrate phases at different pressure (circle signs) and subcooling level (plus signs). The blue and red data are for the systems at constant 10 MPa and 275 K, respectively. This thickness decreases with pressure and subcooling. 125

Figure 5.7. The disjoining pressure at different pressure (circle signs) and temperature (plus signs) regimes. The blue and red data are for the systems at constant 10 MPa and 275 K, respectively. High pressure or subcooling drops this pressure. 126

Figure 5.8. Work of methane hydrate nucleation under different formation scenarios and thermodynamic conditions. The plot (a) is for a system at 275 K (blue line) and 281 K (red line) with the constant pressure of 10 MPa. The green line shows the work for the cap-shaped clustering with θ of 120º. The formation work increases as the system temperature increases. The film-shaped, cap-shaped, and lens-shaped nucleation lower the work of formation compared to the homogeneous case. The plot (b) distinguishes the difference between homogeneous (solid) and

lens-shape (dashed) nucleation work. The plot (c) is for a system at 10 MPa (blue line) and 15 MPa (red line) with the constant temperature of 275 K. The work of formation decreases with pressure. The plot (d) magnifies the variation between the work of lens-shape (dashed) and homogeneous (solid) formation. 129

Figure 5.9. Maximum formation work and its corresponding number of crystal unit cells depend on the cluster formation shape (homogenous or heterogeneous), temperature (a and b) at 10 MPa, and pressure (c and d) at 275 K. The system with high pressure, low temperature, and heterogeneous clustering with a small wetting angle requires lower work of formation. Furthermore, lens-shaped heterogeneous formation is narrowly favorable compared to the homogeneous nucleation.. 130

Figure 5.10. The maximum formation work in units of k_BT (a) and critical number of crystal unit cells (b) for homogeneous nucleation at different pressure and temperature. Low temperature and high-pressure thermodynamic conditions require minimum formation work and critical size, which vastly facilitate the hydrate nucleation process. 131

Figure 5.11. Gas hydrate nucleation rate in different temperature (a) and pressure (b) regimes with (dashed) or without (solid) additives. The constant pressure of plot (a) and temperature of plot (b) are 10 MPa and 275 K, respectively. A is assumed to be 10^{35} and 4×10^{26} $1/m^3s$ for HON and HEN nucleation processes, respectively [19]. Blue, red, green, and black lines represent the lens-shaped, film-shaped, cap-shaped, and homogeneous forms of clustering, respectively. In this work, we adopt the arbitrary values of 10^{-18} m^3 and 10^{25} $1/m^3$ for k_n and C_a, respectively........ 132

Figure 5.12. The formation nucleation rate using the interfacial tension of methane hydrate-water (solid line) and ice-water (dashed line) at 275 K. The rate is prodigiously higher when the ice-water properties are applied. 133

List of Tables

Table 2.1. Simulation parameters including: partial electron charges, distance and angles between atoms or charge sites, and Lennard-Johns potential well depth (ε) and finite distance (σ).......... 34

Table 3.1. Molecular weights, distance and angles between atoms or charge sites, partial electron charges, and Lennard-Johns potential well depth (ε) and finite distance (σ) determine the simulation parameters. 59

Table 3.2. Interfacial excess of the water-gas mixture with and without the propane molecules at 298.15 K and 10 MPa. 62

Table 4.1. Interfacial tension at the water-methane hydrate interface 93

Table 5.1. Number of molecules for the initial configuration.. 115

Table 5.2. Simulation parameters including the molecular and structural properties of the water and methane molecules 116

Table 5.3. The available interfacial tension at the water-methane gas and methane hydrate-water interfaces 121

Chapter 1. General Introduction

1.1. Thesis Motivation

Clathrate hydrates, also known as gas hydrates, or simply hydrates are ice-like crystalline solids that consist of water molecules encapsulating gas molecules [1, 2]. Gas hydrates were discovered years ago by Sir Humphery Davy who first reported the existence and structure of chlorine hydrate in 1810. In the twentieth century, driven by significant progress in the gas industry, the critical importance of hydrate formation to avoid blockages in pipelines was established [3, 4].

In gas hydrates water molecules are linked together by hydrogen bonds (4 bonds per each water molecule) to create cages (cavities) that are called hosts [5]. The gas molecule, which is effectively compressed inside of the water cage is recognized as the guest or hydrate former [6]. A variety of compounds (more than 130) such as light hydrocarbons, noble gasses, oxygen, nitrogen, hydrogen, carbon dioxide, and hydrogen sulfide can form hydrates (see Figure 1.1) [7]. Clathrate hydrates are non-stoichiometric compounds in a manner that some water cages are empty, while each of the other cages hosts a gas molecule inside [8, 9]. Clathrate hosts might also contain gas molecules, not only water molecules, to form compounds known as semi-clathrates [10].

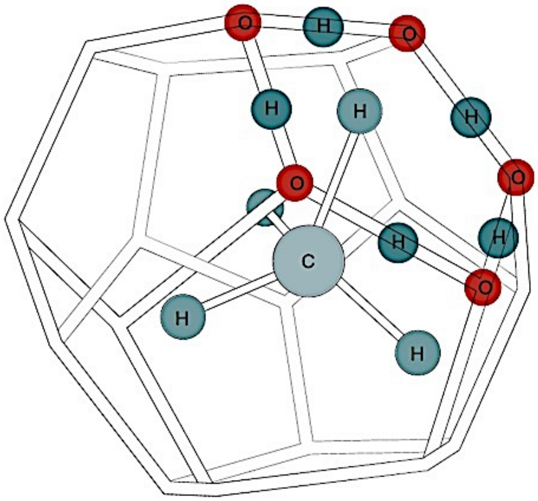

Figure 1.1. Schematic of a methane hydrate. Circles and lines are representative of atoms and chemical bonds, respectively [11].

The presence of a hydrophobic gas molecule inside of the water cage adjusts the hydrogen bonding network to stabilize the structure under the thermodynamically favorable conditions which are low temperatures and sufficiently high pressures, depending on the specific gas compounds [4]. The guest gas molecules interact with the encompassing water molecules by van der Waals forces (i.e., only physical, not chemical interactions) to avoid the cage self-collapse [8, 9]. Therefore, water molecules can form a solid state instead of liquid at the specific thermodynamic conditions [12]. For instance, a mixture of propane and methane forms relatively more stable hydrate than empty or methane hydrate at low pressure conditions [4].

Gas hydrates have a wide range of practical engineering applications in different industries. Hydrates play a very important role in flow assurance (i.e., management of fluid transportation in multiphase flow) as the pipelines, mostly in deep oceans, provide favorable conditions (low temperature and high pressure) for gas hydrates formation, consequently, blockage in pipelines (see Figure 1.2) [8, 9]. The blockage can be costly as it follows with a shutdown in the entire oil and gas processing that might take days or weeks to be resolved. Unfortunately, the current techniques that are being used in industry to avoid the blockage are costly and environmentally damaging.

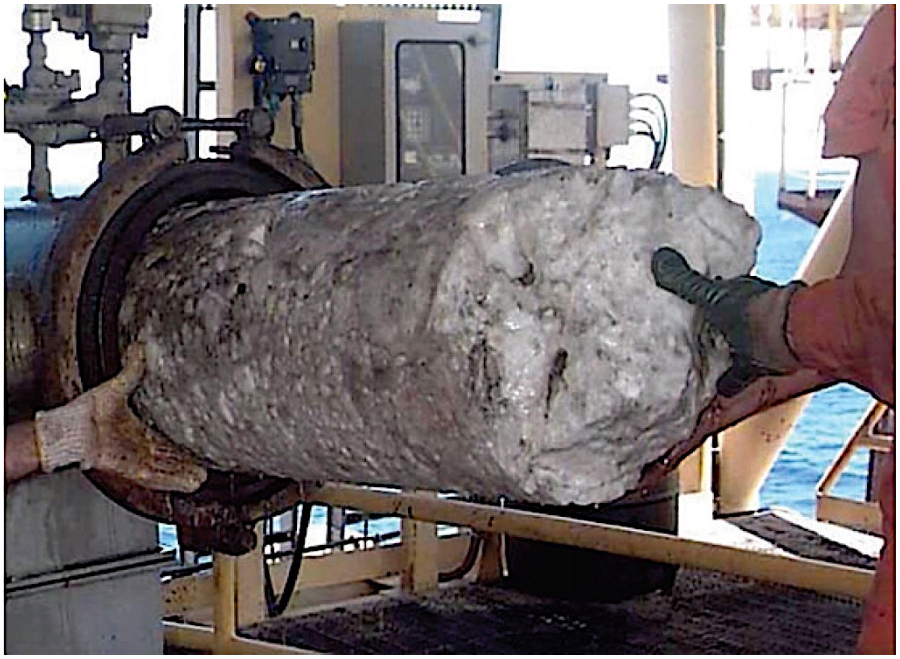

Figure 1.2. Removing a gas hydrate plug from a pipeline [4].

One volume of gas hydrate contains 164 volumes of gas at standard temperature and pressure condition [1]. Therefore, hydrates can be considered a vastly available and clean resource of energy and as well as a potential transportation medium for other materials [1]. In addition, self-preservation is a unique property of gas hydrates that increases and prolongs the stability condition which is desirable for future gas storage applications [4]. Methane hydrates are found to be the most common hydrates formed naturally by biogenic methane in marine sediments and sediments under permafrost with the twice and three orders of magnitude amount of energy that of global fossil fuels and natural gas reserves, respectively (see Figure 1.3) [4, 8, 9, 13, 14].

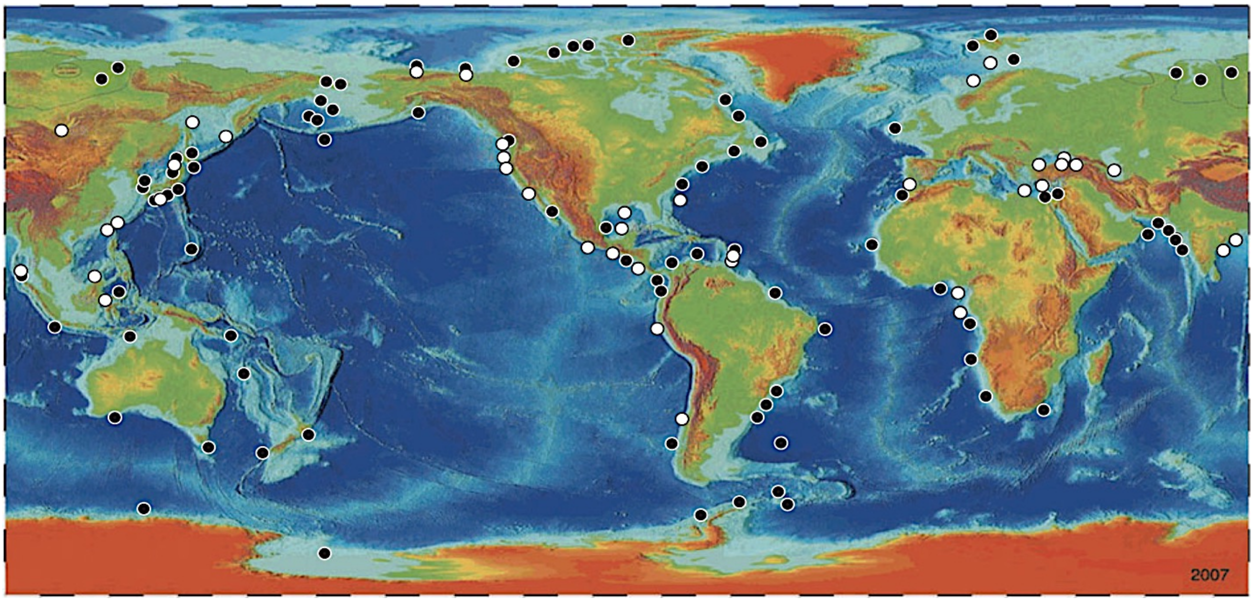

Figure 1.3. Gas hydrates resource map. Filled and open circles show inferred and recovered resources, respectively, in global distribution of gas hydrate deposits [4].

On the other hand, methane hydrates could be a vital source of global warming if they are released to the oceans' surfaces. So, the significance of gas hydrates in environmental applications have been increasingly discussed. Along with other efforts to fight global warming, carbon dioxide sequestration is another example of hydrates application to bury a great amount of a greenhouse gas deep in the ocean [13].

Natural gas hydrate resources formed under permafrost in sediments along the continental margins can be detected by seismic reflection surveys, bottom simulating reflectors (BSRs), or electromagnetics utilizing physical properties: primary-wave (P-wave), velocity, and electrical resistivity, respectively [8]. While, other methods such as X-ray diffraction, Raman spectroscopy, and nuclear magnetic resonance (NMR) spectroscopy are used in characterization laboratories to find the cavity structure, the cage occupancy, and more quantitative information, respectively [4].

1.2. Background and Literature Review

In this section, we introduce some relevant basic facts and principles regarding gas hydrate structures and formation conditions. Gas hydrates begin to form once 90% of the cages are filled. One might expect that ice has a similar physical and thermodynamic behavior of gas as in the case of full occupancy of cages, where 85 mol% of the crystalline is still made of water molecules [6]. In spite of many similarities, some properties such as mechanical strength, heat capacity, and thermal conductivity are different [4, 8, 9]. Therefore, we need to investigate the thermodynamics and material properties of gas hydrates regardless of any analogy with other substances.

First, we need to understand under which circumstances water molecules form crystalline ice-like solids above its freezing point. The formation process consists of thermodynamic and kinetic contributions. Thermodynamic (time-independent) behavior of gas hydrates can be well understood owing to a large amount of experimental and theoretical work performed during past decades. However, gas hydrate formation is a stochastic time-dependent process [15]. Therefore, the kinetic behavior plays an important role that is still unknown and cannot be ignored in study of gas clathrates [6]. Later in this thesis, we present novel, accurate, and efficient computational methods in order to investigate both kinetic and thermodynamic behaviors of such system.

1.2.1. Gas Hydrate Structures

Clathrate hydrates can be formed in different crystalline structures depending on many factors such as the number of water molecules, number and size of the guest molecules, guest-water molecules repulsions, and thermodynamic conditions [1, 4, 6]. The motions of guest molecules include more rotation and vibration than translation as a result of the cage confinement [6]. There are three well-defined structures (sI, sII, and sH) that have been discovered. The first type recognized as sI which is the simplest structure of hydrate and naturally exists. This hydrate consists of two different cages: dodecahedron as the small cage and tetrakaidecahedron as the large cage. Dodecahedron (5^{12}) consists of twelve pentagonal sides to form the most common cage in all hydrate structures [1]. As dodecahedrons cannot efficiently pack, two hexagonal sides are added into dodecahedrons and form tetrakaidecahedrons ($5^{12}6^{2}$) to fill the space between 5^{12} cages preventing hydrogen bonds from straining and breaking [6, 12]. In the cubic structure of sI, the entire crystal consists of small repeating units of a crystalline structure called unit cells with the composition of two dodecahedrons and six tetrakaidecahedrons ($2.5^{12}+6.5^{12}6^{2}$). Each unit cell contains 46 water molecules and guest molecules such as methane, ethane, H_2S, and CO_2 depending on the size of the cage and molecule. For instance, ethane molecules can only occupy the large cages of sI hydrate owing to its large size of molecules. The cavities of sI hydrate can generally accept guests with diameters in the range of 0.4-0.55 nm [1].

The second abundant hydrate structure is known as sII with the unit cell structure of $16.5^{12}+8.5^{12}6^{4}$ comprising of 136 water molecules. In this cubic structure, the crystals contain sixteen dodecahedrons as the small cavities and eight hexakaidecahedron ($5^{12}6^{4}$) as the large cavities. Hexakaidecahedron is a 16-sided polyhedron that has two hexagonal sides added to tetrakaidecahedron (large cage of sI hydrate) [16]. The sII hydrate material can exist in artificial environments such as pipelines in oil and gas industries. This gas hydrate structure is relatively energetically less stable than sI, while it can accommodate larger molecules (0.6-0.7 nm diameter) such as propane, nitrogen, and isobutane in the large cages [5]. This variable size ratio of gas molecule to cage determines occupancy and thermodynamic properties of the hydrate [6]. Generally, each cage encapsulates only one guest molecule. However, in high pressure conditions (GPa range), multiple molecules occupancy might occur in large cavities of sII structures [7]. Please note that because of the large presence of propane, isobutane, and even heavier hydrocarbons, sII is the most common structure in flow assurance [4]. However, sI and a mixture of sI and sII can coexist in gas pipelines [17, 18].

The other type of gas hydrates that exists in both natural and man-made environments is known as sH. The sH hydrate structure is found to be hexagonal with the ability of containing guest molecules with the mixture of both small (0.4-0.55 nm) and large (0.8-0.9 nm) diameters such as cyclooctane, cyclohepthane, and ethylcyclopentane. The unit cell includes 34 water molecules with a geometrical structure of $3.5^{12}+2.4^{3}5^{6}6^{3}+1.5^{12}6^{8}$ [19]. As the components of sH hydrate do not exist in natural gas, the formation of sH hydrates is assumed to be less probable in gas flowlines [1, 19].

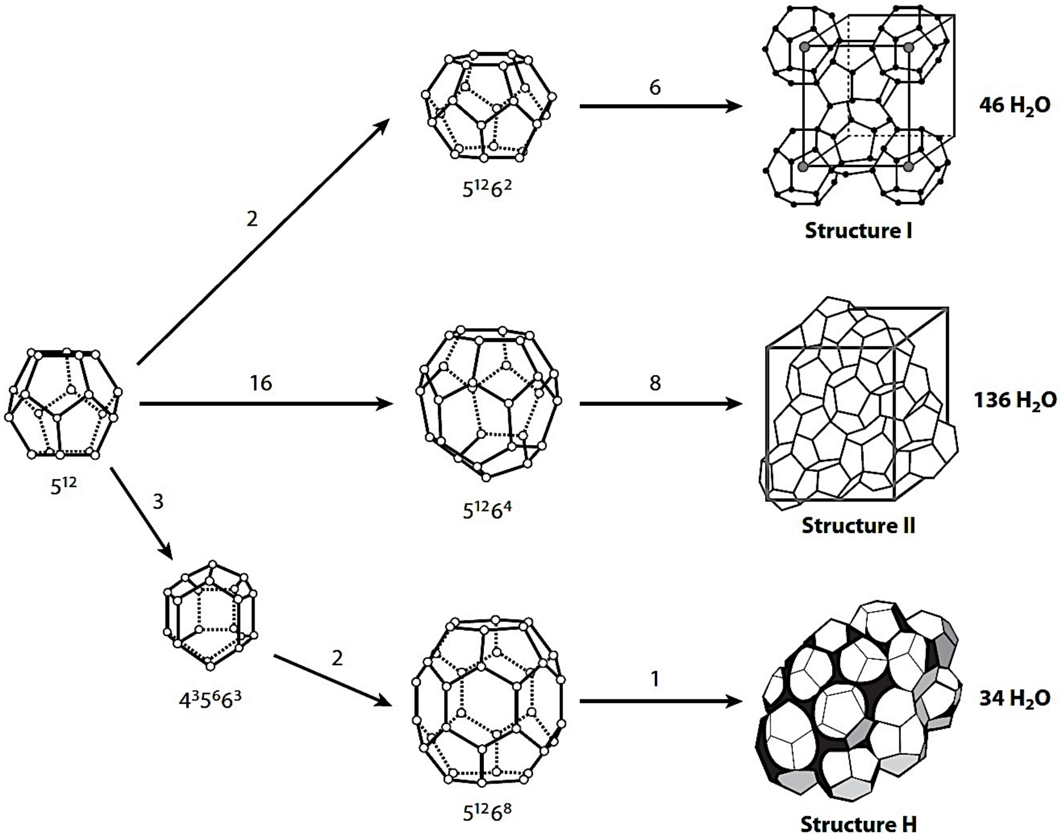

Figure 1.4. Visualization the various gas hydrates structures and geometries. Atoms shown by points are connected together by hydrogen bonds to form repeating crystal structures of water cages for gas hydrate structures sI, sII, and sH [4].

1.2.2. Gas Hydrate Formation

Formation of gas hydrates that includes nucleation and growth process as the onset of hydrate plugs in flow assurance has been studied for years, however, there is much yet to know. Gas hydrates precursors need to be at favorable conditions in order to begin the formation process. The proper thermodynamic pressure (> 0.6 MPa) and temperature (< 323 K) [4, 6], presence of guest molecule as the hydrate former, and sufficient amount of water are necessary for such process. Some conditions such as turbulence generated by high velocity or agitation, the presence of nucleation sites, and free water might enhance the gas hydrate formation rate [16]. As the existence of gas hydrates is unfavorable to flow assurance, researchers search to minimize hydrate formation by eliminating one of the main three necessary parameters mentioned above. The absence of guest molecule is not possible since it is the desired product. Other mitigating approaches such as pigging, dehydration, heat tracing, depressurizing, and chemical inhibitors have been applied in gas industry for safety and for saving large amounts of down-time and money by achieving blockage avoidance [4, 6, 16].

1.2.2.1. Nucleation and Growth

Gas hydrate formation consists of three main steps: induction time, growth, and dissociation. Nucleation of gas hydrates begins at the liquid-gas interface during the induction or lag time (region 1 in Figure 1.5), which is the elapsed time until the hydrates can be detected macroscopically (tens to thousands of molecules) [1]. At this stage, gas molecules dissolve in water to form labile clusters. As new clusters are forming, the cluster assemblies share faces eventually turning into sI and sII structures, consequently, increase system disorder (see Figure 1.6) [3]. The thermodynamic temperature and pressure conditions are in the region of hydrate stability. In general, for a pair of solute-solvent, there exists a relationship for concentration and temperature that defines the metastable limit. This relationship is formally called thermodynamic spinodal to represent the supersaturation limit. However, the formation of metastable hydrates is restrained due to high entropy condition until the cluster agglomerate reaches critical crystal nucleus size for steady growth [1].

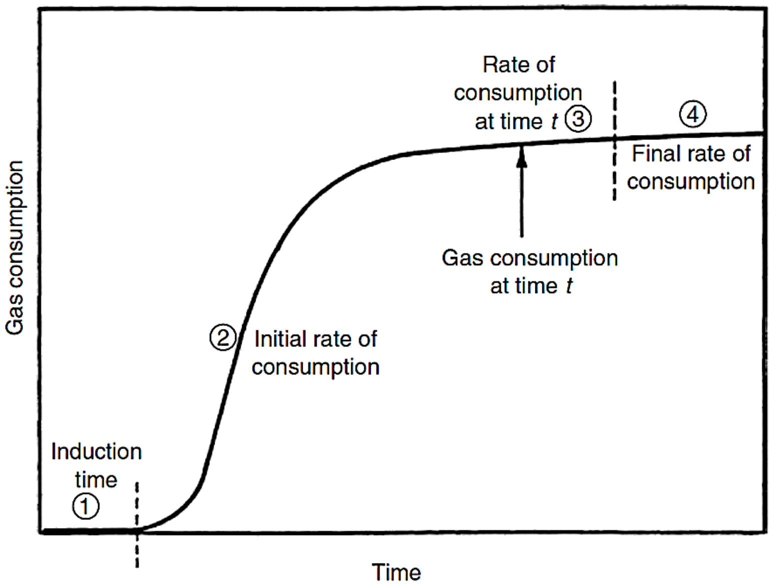

Figure 1.5. Conceptual gas consumption diagram for hydrate formation [1].

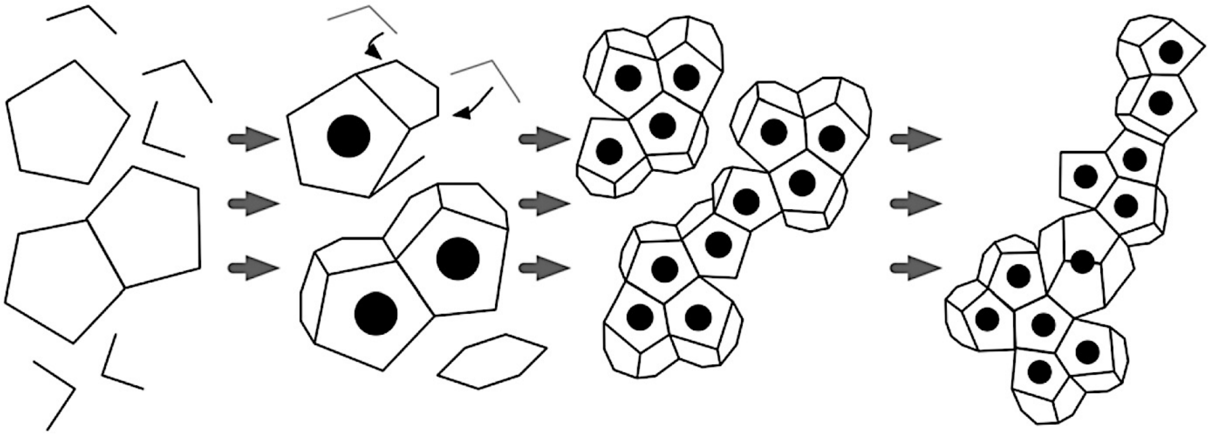

Figure 1.6. Schematic model of hydrate nucleation. Guest molecules (filled black circles) encompassed by water cages agglomerate to form hydrate clusters [1].

Gas hydrate nucleation time differs in a set of experiments with the same conditions since the nucleation is a stochastic process that relies on different driving forces such as: subcooling (i.e., the difference between the equilibrium and system temperatures) [20], supersaturation (i.e., chemical potential difference), Gibbs free energy difference [21], and fugacity ratio [4, 7, 22-26]. Better driving force conditions may reduce the induction time and randomness of nucleation process [1].

Supersaturated systems can create a new phase either in bulk (homogenous) or at a surface in contact with the bulk (heterogeneous). Homogenous nucleation does not naturally occur since the hydrocarbon flow always carries impurities. Conceptual molecular models of hydrate nucleation suggest that the hydrate formation initially occurs at the vapor-liquid interface as the interface lowers the Gibbs free energy of nucleation. Additionally, the interface has higher concentrations of both water and guest molecules, while the water mole fraction in gas phase and gas mole fraction in aqueous phase are less than 0.05 and 0.001, respectively [1]. Therefore, the labile hydrate clusters are adsorbed and agglomerated on the vapor-liquid interface to form local structures of nucleation [27].

Once the induction period is completed, the rapid growth (region 2 in Figure 1.5) of gas hydrates is initiated from the critical crystal nuclei. Nucleation conditions still matter during the growth period [1]. Figure 1.7 shows a hypothetical general growth mechanisms that also applies for gas hydrates. Briefly, the hydrate clusters first interact with the surface of the solid hydrate crystal (i). The clusters might either attach to (ii) or move along the surface (iii) with an attempt of attachment to the crystalline step (iv) or a defects (v). Water molecules can be either incorporated into the solid hydrate phase or diffused back into the fluid phase (ii, iv, vi) [3]. As the clusters are being added to the hydrate crystal structure, as a result, the concentrations of free gas and water molecules at the interface are decreasing. Therefore, the gas consumption rate reaches a plateau (regions 3 and 4 in Figure 1.5).

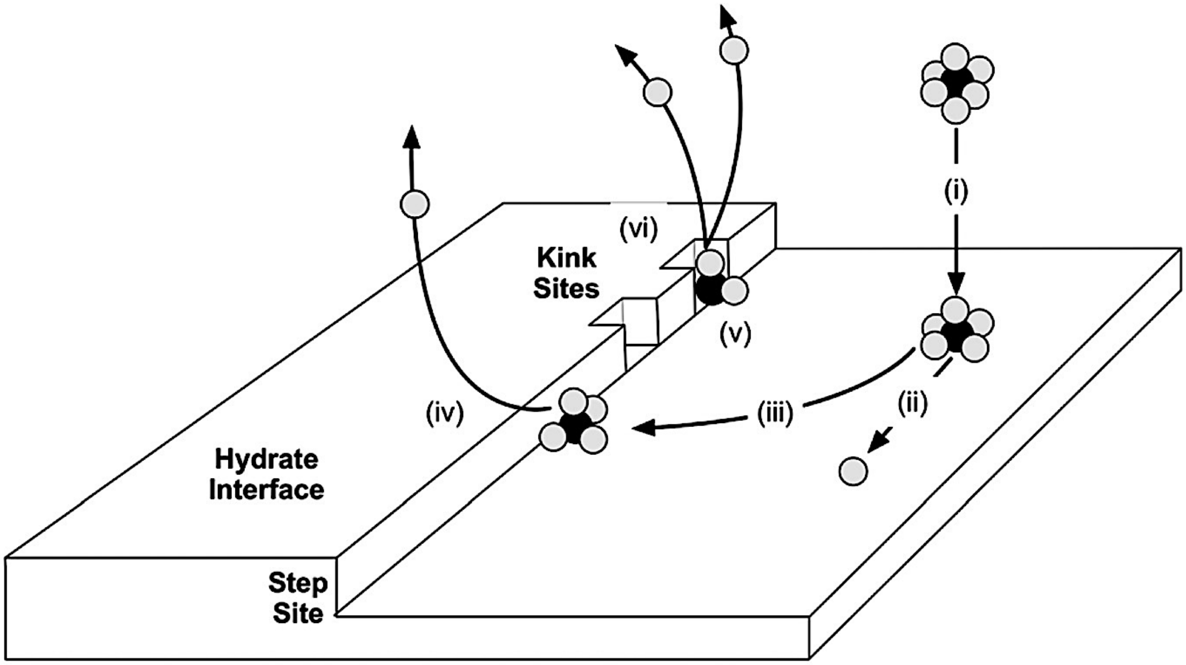

Figure 1.7. Schematic of crystal growth of gas hydrates. Clusters are attached to the hydrate interface. Guest molecules (black circles) join the surface and water molecules (gray circles) can either join or diffuse away [1].

The process of hydrate crystal growth is controlled by three major factors: intrinsic growth kinetics (growth rate of hydrates which is less effective than other factors), mass transfer (gas diffusion through the hydrate surface), and heat transfer (exothermic heat of hydrate formation [13]). Intrinsic growth kinetics is only presented in real systems (as in turbulent pipeline flow) for sI hydrates [1].

The morphology of crystalline hydrate is virtually independent of hydrate formers and system pressure [20], and depends on the growth period, which is influenced by the driving forces [28]. The subcooling degree regulates the size of the individual hydrate crystals. Figure 1.8 shows a single droplet of hydrate crystals formed under different driving force conditions. At low degree of subcooling, small numbers of large hydrate crystals form. On the contrary, multiple crystal growths occur with high subcooling or in an agitated system. Hydrate crystals are likely to nucleate and grow at many different locations with an initiation needle-like shape that will eventually collapse onto the interface [1, 20, 29].

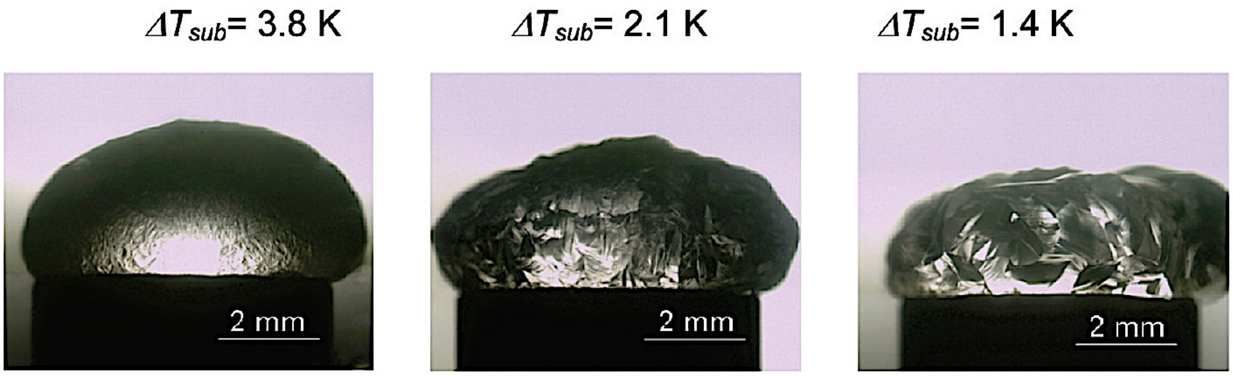

Figure 1.8. Morphology of gas hydrate at the liquid-gas interface in different subcooling conditions [20].

Hydrate shell (film) growth mechanism at the water-hydrocarbon interface is initiated at some random points on the surface of a water droplet [20]. As more clusters with a mixture of sI and sII structures join the existing hydrate phase, the internal water droplet volume shrinks (see Figure 1.9). Interfacial tension and shear stress from fluid stabilize this water droplet [3, 30].

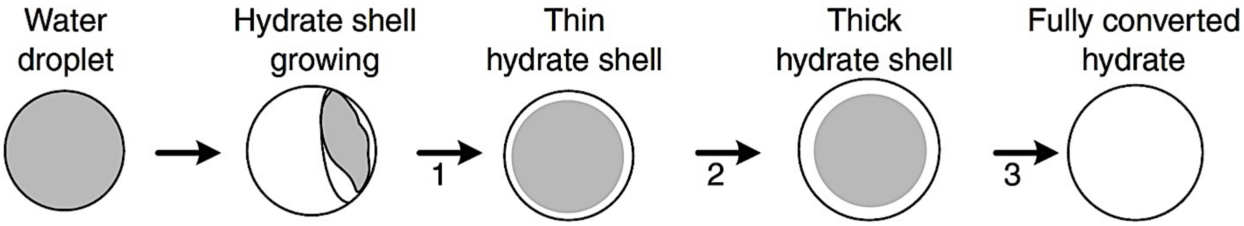

Figure 1.9. Mechanism of the hydrate shell growth around a water droplet. Hydrate formation begins with a thin porous shell around the droplet. The shell thickens until the entire droplet turns into a hydrate compound [1].

Hydrate formation rate is about 1 mm^3/s for an initial thickness of 3,000 to 18,000 times the unit crystal length of sII [31]. Gas and water molecules might diffuse inside of the bulk interior droplet away from the hydrate shell-water interface and from interior to outer shell surface, respectively. This extra diffusion does not affect the shrinking core process. However, as permeability of the hydrate later decreases, this molecular transport becomes more difficult, and surface renewal is necessary [6]. High driving force may assist the hydrate shell to increase the thickness. Nevertheless, the chemical species and guest-in-water solubility of the entrapped gas molecule mainly govern this thickness [20]. Water droplets with a diameter of larger than 40 μm might take hours to days to fully convert to hydrate while the droplets with a diameter smaller than 15 μm, the conversion occurs very fast [31]. On the contrary, some experiments reported that the size of water droplets has negligible effect on the hydrate formation and morphology [29].

Hydrate dissociation also occurs during any step of the hydrate formation. Since the dissociation or melting process is endothermic, heat transfer plays a dominant role in comparison with intrinsic kinetics (prevailing at very early stage), solubility and mass transfer. Gas hydrate exploits memory effect phenomenon that promotes hydrate formation from a melted hydrate phase. However, this effect does not systematically decrease the formation time [15].

1.2.2.2. Interfacial Energy

Interfacial tension plays a key role in nucleation process of gas hydrates, which dictates the morphology, location, and growth rate [3, 30]. In this thesis, we first try to understand the basic theory of gas hydrate nucleation as the most challenging step in order to find ways to inhibit or promote it depending on the applications [32-35]. The kinetic and thermodynamic behaviors of the additives will be described later in chapter 5.

In the classical theory of nucleation, formation of a new cluster phase consisting of n crystal unit cells needs work to compensate the energy consumed for a combination of interfacial energy and creation of a new phase that occupies space (see Figure 1.10). This formation work is given by:

$$W(J) = -n\Delta\mu + c(nv_h)^{\frac{2}{3}}\gamma \tag{1.1}$$

where $\Delta\mu$ (J) measures the supersaturation (i.e., difference in the chemical potentials) as a function of pressure and temperature, c is a shape factor, v_h is the volume of a hydrate building unit, and γ (J/m^2) accounts for the effective specific surface energy. Owing to great importance and dictating effects, the surface energy contributed in aqueous hydrate mixtures is the main focus of this thesis.

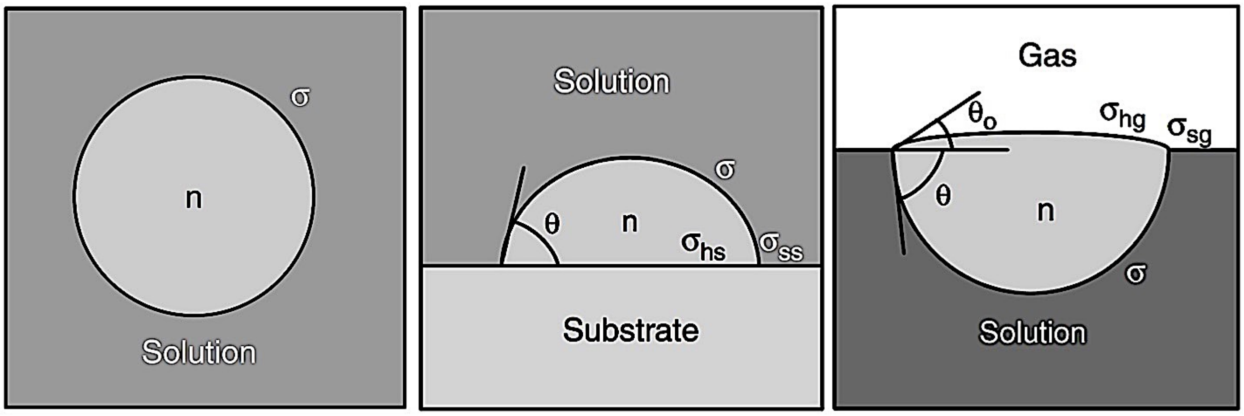

Figure 1.10. Schematic nucleation theory of gas hydrates in the solution (left), the substrate-solution interface (middle), the solution-gas interface (right) [33].

Generally, the surface energy cannot be obtained precisely from only experiments [39, 40]. Therefore, we may assume the specific surface energy is the same as the surface tension for polycrystalline solids in large scale formation as they are statistically isotropic [41]. Then, we can readily obtain these crucial parameters from the application of molecular dynamics to stress tensor calculations for gas hydrates [39]:

$$P = \begin{pmatrix} P_{xx} & P_{xy} & P_{xz} \\ P_{yx} & P_{yy} & P_{yz} \\ P_{zx} & P_{zy} & P_{zz} \end{pmatrix} \tag{1.2}$$

Each component of this stress tensor (sometimes called the pressure tensor) is obtained from:

$$P_{ab} = \frac{1}{V}\sum_i \left(\frac{p_{ia}p_{ib}}{m_i} + r_{ia}f_{ib}\right) \tag{1.3}$$

where ab, i, p, m, r, and f represent the tensor component, the particle index, the momentum, the mass, the position, and the force, respectively. Subsequently, the interfacial tension (γ) is given by:

$$\gamma = \sigma + \sigma_{sg} + \sigma_{hg} = \int_{-\infty}^{+\infty} dz \left[P_{zz} - \frac{1}{2}\left(P_{xx} + P_{yy}\right)\right] \tag{1.4}$$

The chemical and physical interactions between hydrophobic methane gas and polar liquid water molecules cause abrupt change in the local density profile, which disrupt the isotropy of interface. Hence, the anisotropic interfaces demand unique computational techniques to cope with their asymmetry.

1.2.2.3. Inhibition of Gas Hydrate Formation

The presence of chemical additives affects the nucleation and growth processes of gas hydrates. In addition, additives in the system invalidates many theories and equations of states for gas hydrates [42]. The effect of additives can be either promoting [43-45] or inhibiting [46-49] gas hydrate formation. Promoting hydrate formation is of interest with some applications such as gas storage, seawater desalination, gas transportation, and CO_2 sequestration, however in this document, we investigate only additives with inhibiting effects, known as inhibitor, to prevent the hydrate blockage and blowout in pipelines, both onshore and offshore [4, 6, 8, 13].

Nowadays, there are two main types of inhibitors used in the oil and gas industry: thermodynamic and low dosage hydrate inhibitors. Moreover, natural oils and salts present in the environment can assist the inhibition process to a certain degree [4, 31].

Formation and stability of gas hydrates require specific thermodynamic temperature and pressure conditions (i.e., higher pressure and lower temperature than their equilibrium condition). In the thermodynamic inhibition method, a hydrogen-bonding additive shifts the required thermodynamics conditions at which gas hydrates are no longer stable or forming. In other words, the thermodynamic inhibitor competes with gas hydrates to make hydrogen bonds between its oxygens (negative side) and water molecule hydrogen (positive side) to hinder hydration; therefore, the gas-water system needs higher pressure and lower temperature to provide the sufficient driving force of hydrate formation [6]. Figure 1.11 presents temperature and pressure profile subjected to an oil and gas pipeline from a deep water well to the onshore facility. Any fluid inside the shaded hydrate stability/formation region can form gas clathrates, which may result in pipe blockage. Methanol and monoethylene glycol (MEG) are two ubiquitous examples of thermodynamic inhibitors [42]. However, methanol can also show promoting effects under some conditions [50].

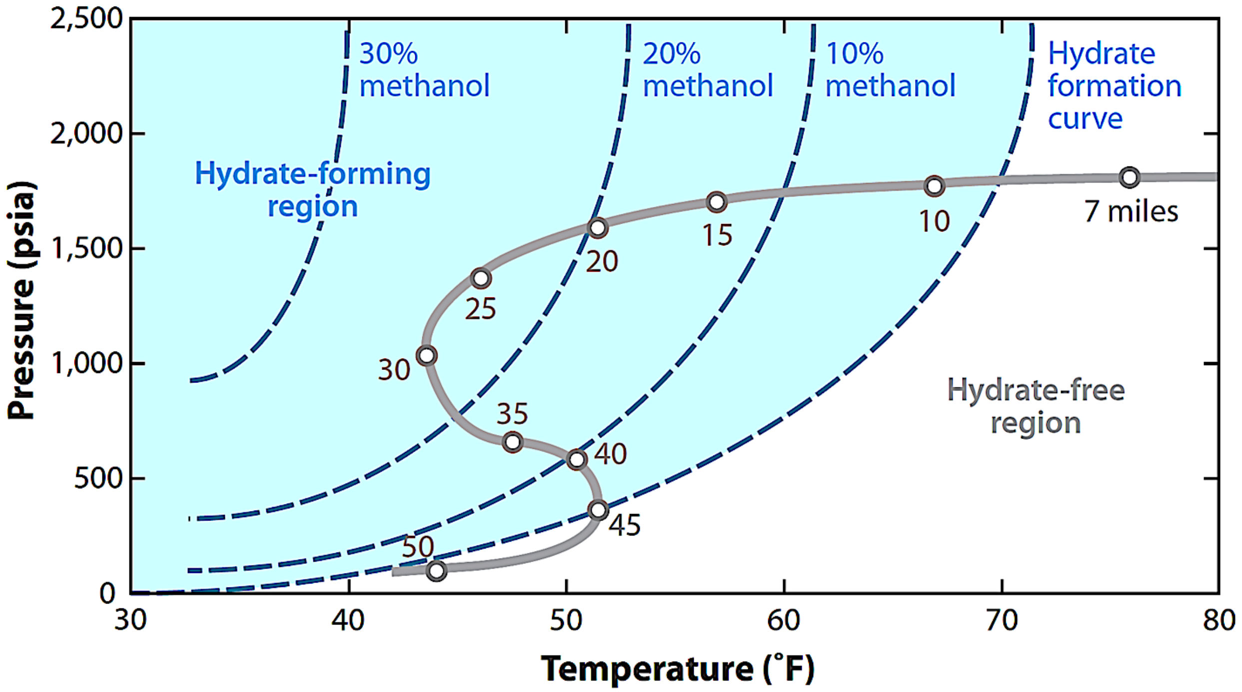

Figure 1.11. Gas hydrate stability region with and without the presence of the thermodynamic inhibitor in a submerged oil and gas pipeline [4].

Thermodynamic inhibitors must be added to a flow-line with a minimum concentration (40-60 vol%) to technically affect the hydrate formation [4]. This large amount of an undesired substance causes problems such as pipe corrosion and eventual separation and recovery. For instance, oil and gas companies globally spend around US$ 220 million/year on using methanol [6]. Hence, a new series of inhibitors was introduced to the industry defined as low dosage hydrate inhibitors (LDHI) [49, 51].

Unlike thermodynamic inhibitors, LDHIs do not shift the equilibrium curve of gas hydrates. Their effects are time dependent and their use requires small amounts (around 1 wt%) to prevent pipeline blockage caused by gas clathrates. According to different inhibition process, LDHIs are categorized into two types: kinetic hydrate inhibitors and anti-agglomerant inhibitors [51-54].

Kinetic hydrate inhibitors (KHI) slow the hydrate crystallization process. Polymers with low molecular weight such as polyvinylpyrrolidone (PVP) and polyvinylcaprolactam (PVCap) are injected into the aqueous phase to wrap around the hydrate surface inhibiting significant crystal growth [47, 52, 55-57]. This inhibition process by anchoring polymers does not cease the gas hydration. It only prolongs the clathrate formation process until the fluid reaches the onshore facilities without plugging the pipeline, unless the driving force is very high (e.g., more than 10 K subcooling) [4].

The other type of low dosage hydrate inhibitors are anti-agglomerants (AA). They are long polymer molecules that create non-polar coatings encompassing hydrate crystals to prevent their further agglomerations with other hydrate crystals due to capillary attraction. This non-sticky slurry of small clathrate particles can be suspended and transported in the flowline with no blockages. Anti-agglomerant inhibitors require a flow of liquid hydrocarbon phase in the gas line, as opposed to kinetic hydrate inhibitors [1].

Most of the current low dosage hydrate inhibitors, which are used in oil and gas industry, are expensive and with environmentally harmful effects. Therefore, the challenge to find cheaper, biodegradable, and environmentally friendly inhibitors yet exists.

1.2.3. Modeling and Simulation

Clathrate hydrate formation is a nanoscale, rapid, and stochastic process, but experiments do not capture and resolve these main characteristics [15]. In addition, experiments could be relatively hard and expensive to provide the necessary thermodynamic conditions (high pressure and low temperature), specifically in the case of sII gas hydrates as the predominant structure of natural gas hydrates in the pipelines. Instead, the powerful analytical and computational simulations may elucidate the kinetic behavior of hydrates formation. Therefore, we model the clathrate hydrates to seek fundamental and critical insights of the nucleation and growth processes.

Many researchers have applied a very successful and well known model called van der Waals-Platteeuw (vdWP) to investigate gas hydrates' thermodynamics based on an analogy to the gas adsorption Langmuir model as a measure of the interaction strength between gas and water molecules [4]. This model measures the supersaturation using grand canonical ensemble with four assumptions: one-component guest molecule hydrate, fixed spherical hydrate cage volume, negligible guest-guest molecules interactions, and no quantum effects [4, 26, 58]. The following equation gives the variation of chemical potential of water in the hydrate as a result of the gas enclathration [59, 60]:

$$\mu^0 - \mu^H = \Delta\mu_w^H(T,P) = -RT\sum_m \upsilon_m ln\left(1 - \sum_j \theta_{mj}\right) \tag{1.5}$$

where R, T, υ_m, θ_{mj}, μ^H and, μ^0 are gas constant, temperature, number of cages of type m per water molecule in the hydrate, fraction of cavities of type m occupied by the guest j, and water chemical potential in the occupied and empty hydrates, respectively. The θ_{mj} fraction is obtained from the Langmuir function for the gas fugacity, assuming there is only one guest per cage [59, 60]:

$$\theta_{mj}(T,P,y) = \frac{C_{mj}(T)f_j(T,P,y)}{1+\sum_{i=1}^{ncomp} C_{mj}(T)f_j(T,P,y)} \tag{1.6}$$

where f_j and C_{mj} are the fugacity of guest j in the liquid hydrocarbon phase and Langmuir constant, respectively. One might calculate the θ_{mj} fraction for a hydrate lattice occupied with more than one guest from the expressions below [59, 60]:

$$\theta_{mj}^{(k)} = \frac{F_{mj}^{(k)}}{1+\sum_{i=1}^{k} F_{mj}^{(i)}} \tag{1.7}$$

where $F_{mj}^{(1)} = C_{mj}^{(1)} f_j$ for 1 guest, $F_{mj}^{(2)} = C_{mj}^{(1)} C_{mj}^{(2)} f_j{}^2$for 2 guests, $F_{mj}^{(3)} = C_{mj}^{(1)} C_{mj}^{(2)} C_{mj}^{(3)} f_j{}^3$ for 3 guests, and so forth.

Generally, the Langmuir constant is the most challenging part of vdWP model, which requires a very accurate method to account for the interactions between guest and water molecules of hydrates. Provided to form a spherically symmetric cage, the only existing interactions are between one guest with its surrounding water molecules, the Langmuir constant C_{mj} is given by [59, 60]:

$$C_{mj} = \frac{4\pi}{k_B T}\int_0^{Rcell} exp\left(\frac{-W(r)}{k_B T}\right) r^2 dr \tag{1.8}$$

where $W(r)$ is a simple cell potential function relating the guest-water molecules that is traditionally calculated from Lennard-Jones or a Kihara spherical core potential, firstly introduced by Parrish et al. [2].

The main issue with the proposed potential functions is that they need a set of parameters found numerically. Many researches attempted to analytically estimate these parameters. For instance, viscosity and second virial coefficient data might be used to determine the parameters of the Kihara cell potential [23, 60]. However, experiments provided more accurate results for these parameters [4, 60, 61]. As mentioned before, the experiments cannot capture all the key characteristics of gas hydrate systems. To model a real system, a set of molecular simulations can more precisely estimate the supersaturation compared to the challenging and inaccurate experimental work regarding the cell potential parameters.

Despite the fact that vdWP model predicts well the equilibrium conditions of methane hydrates, the assumptions made in vdWP model can drastically affect the results. For instance, the equilibrium pressure of propane hydrates cannot be well determined by this model owing to hydrate cage size change with the guest size and incomplete information of the neighboring guest-guest interactions [12, 24]. Only the interactions of the water molecules engaged in the cage and the neighboring cages can change the Langmuir constant by 280 % [22].

Given these challenges one might seek to use ab initio molecular dynamics or density functional theory (DFT) in order to study the clathrate hydrate systems. These subatomic methods need to create a force field by applying quantum mechanics methods to the interactions of the individual electrons to study the motions and interactions of the atoms, resulting in unacceptable prolonged simulation time. Therefore, the model can only contain very few atoms at T = 0 K, thus neglecting the thermal motions of the molecules and also the interactions of the neighboring guest and water molecules to save simulation time [5]. However, even if such techniques yielded very important results at the single crystal lattice length scale, the simulated model does not represent an accurate gas hydrate system at large scales. Hence, molecular dynamics (MD) [62-67] and Monte Carlo (MC) [59, 68-72] simulation methods could be employed with no need of vdWP assumptions, to analyze the detailed atomistic mechanisms underlying the kinetic behavior of gas hydrates formation and compare them with the results obtained from experiments, simulations and theory.

Herein, we use the molecular dynamics technique to numerically explore equilibrium configurations and transport properties as a function of time. In this thesis, we solve Newton's equations of motion for the constituent atoms with the distributed potential and kinetic energies to explore configurational space. Relatively heavy nuclei allow us to assume that the particles behave as a classical many-body system with no quantum effect for a wide range of materials [73, 74].

First, we need to set the initial coordinates and velocities of the atoms along with a predefinition of the favorable interaction potential as the energy function in a system with periodic boundary condition. We can readily observe the effect of temperature and motion for given intermolecular and the intramolecular potentials. We can choose a finite temperature, which is an equivalent set to the initial velocities so that the average kinetic energy is $3k_BT/2$. Then, we calculate the pair forces with a cut-off distance acting on the atoms to analyze their motions at every time step. The force calculation is probably the most expensive operation in MD. Then, we follow Newton's prescription by applying Verlet algorithm to determine the new atoms coordinates and velocities after each time step in the order of femtosecond [73-77].

In an analogous manner to the experiments, the simulations should be performed over thousands of time steps. We more accurately average the desired properties in a long-time run to capture the most reliable outcome when the system equilibrium is guaranteed.

1.3. Thesis Objectives

Nucleation and growth play the most important role of clathrate hydrates study in various technical and environmental applications. Despite that thermodynamics of hydrate formation has been extensively studied, an accurate description and characterization of its kinetic behavior is still largely lacking. As mentioned above, experimental findings are unable to elucidate molecular details of the formation process such as stochastic nucleation. The majority of existing experimental studies have been performed on sI gas hydrates as the necessary formation conditions of sII hydrates are very difficult and expensive, despite that such hydrates are the most ubiquitous structure of gas hydrates forming in oil and gas pipelines. Current purely theoretical work has also not succeeded in explaining and characterizing hydrate formation owing to their inaccurate assumptions that have been explained earlier in this document. These facts leave us with the opportunity to exploit new theories and powerful computer simulations to better clarify the fundamental material physics behind the formation process. Therefore, the main objectives of this work are:

1) Compute the interfacial tension between the following interfaces at different pressure and temperature regimes:
    - Water-methane gas (Chapter 2)
    - Water-natural gas (Chapter 3)
    - Water-methane hydrate (Chapter 4)
    - Methane hydrate-methane gas (Chapter 5)
2) Relate the interfacial tension versus temperature and pressure to the classical scaling laws (Chapter 2, 3).
3) Establish all possible mixtures among the liquid water and methane hydrate and gas in order to investigate the structural, mechanical, and thermodynamic properties (Chapter 2-5).
4) Characterize the effect of pressure and temperature on the interfacial tensions in the aqueous methane hydrate solution (Chapter 2-5).

5) Find the structure of natural gas hydrate in a wide range of pressure and temperature (Chapter 3).
6) Evaluate the effect of methane hydrate crystal elasticity at the interface with water and methane gas on the interfacial tension (Chapter 4).
7) Calculate the interfacial energy and supersaturation contributions as a function of temperature and pressure in order to determine the formation process, location, and morphology of the methane hydrate (Chapter 5).
8) Approximate the methane hydrate nucleation work and growth rate in the presence of hydrate inhibitors (Chapter 5).
9) Compare the methane hydrate formation when using the interfacial properties of ice and methane hydrate (Chapter 5).

We meet these objectives with the use of accurate and efficient computational work. In this work, we employ molecular dynamics to simulate the grain-size formation process of gas hydrates (e.g., methane hydrates). We extend this work by adding other gas molecules to create a system consisting of a mixture of sI and sII hydrate structures to approach the more realistic system of oil and gas in a flow-line. To accomplish this goal, we use a well-established modeling software called Large Scale Atomic/Molecular Massively Parallel Simulator (LAMMPS). This software is a robust and accurate open source simulator for molecular dynamics. It is worth mentioning that the MD codes are run on the Calcul Quebec and Compute Canada supercomputers. When we collect the data obtained from the simulations, we compute and analyze the desired properties such as supersaturation, interfacial energy, cage occupancy, and thermodynamic conditions. Moreover, we use Visual Molecular Dynamics (VMD) and MATLAB software to generate plots and 3D graphics for visualizing and analyzing our large-scale systems.

1.4. Thesis Organization

The organization of this thesis is shown in Figure 1.12 and described in the following pages.

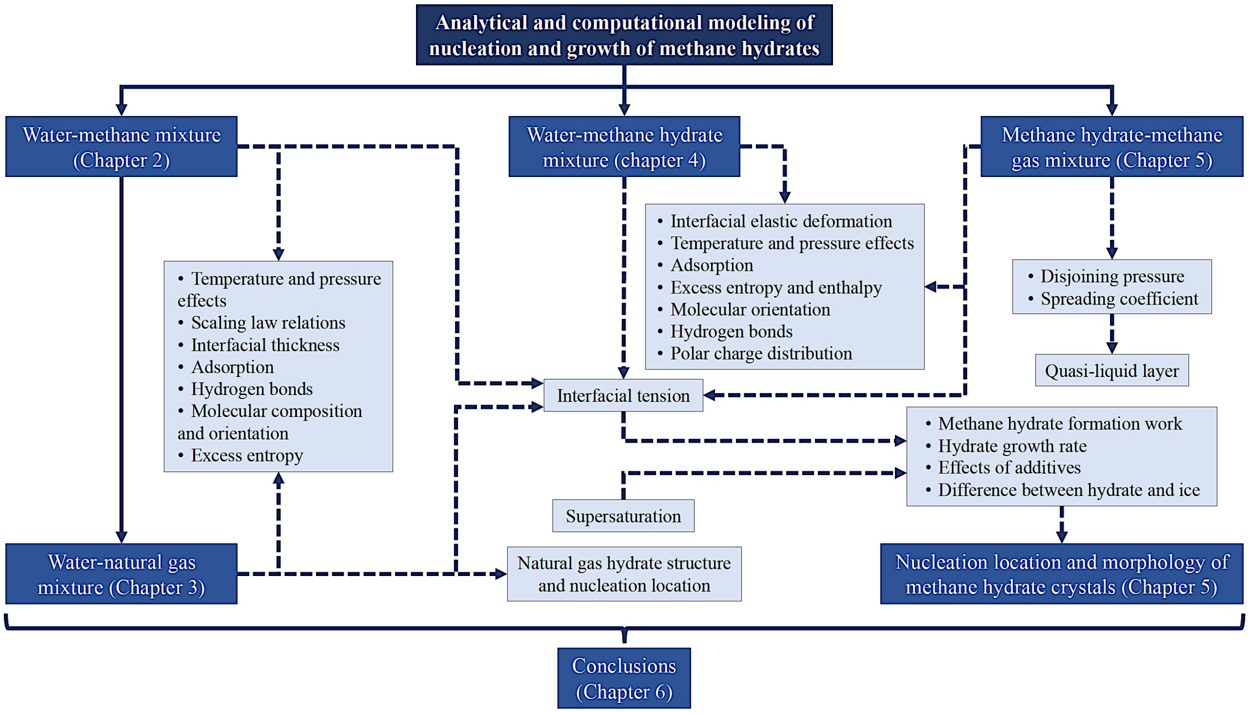

Figure 1.12. Thesis organization chart connecting the objectives and chapters 2-5.

Chapter 2: Mirzaeifard, S., P. Servio, and A.D. Rey, Molecular dynamics characterization of temperature and pressure effects on the water-methane interface. In this chapter, the interfacial tension between the liquid water and methane gas phases is investigated over a wide range of pressure and temperature using a sophisticated ensemble in molecular dynamics. Some crucial interfacial phenomena such as adsorption and hydrogen bonding that adjust the surface tension are investigated.

Chapter 3: Mirzaeifard, S., P. Servio, and A.D. Rey, Molecular dynamics characterization of the water-methane, ethane, and propane gas mixture interfaces. In this chapter, we include ethane and propane molecules in the gas phase to mimic a realistic natural gas-water mixture. The interfacial tension as a function of temperature and pressure is computed at the water-gas interface using a novel and accurate molecular dynamics technique. We seek insights into the location of the gas hydrate formation by investigations on the hydrogen bonding, composition, surface excess, and radial distribution function.

Chapter 4: Mirzaeifard, S., P. Servio, and A.D. Rey, Modeling and simulation of water and methane hydrate crystal interface. In this chapter, we use the mechanical approach to interfacial tension combined with the effect of interfacial elastic deformation to study the non-planar interface of the methane hydrate crystals. The interfacial tension between the methane hydrate and liquid water is computed in a wide range of pressures and temperatures.

Chapter 5: Mirzaeifard, S., P. Servio, and A.D. Rey, Characterization of nucleation of methane hydrate crystals: interfacial theory and molecular simulation. In this chapter, the main focus is on the methane hydrate formation over a range of temperature and pressure to understand the effect of interfacial energy and supersaturation contributions in the nucleation process. Different types of interfaces formed between gas-hydrate, gas-liquid, and hydrate-liquid are considered to better model the formation.

Chapter 6: Conclusions and contributions to original knowledge. In this chapter, we discuss the key findings of this work and their significances along with a list of contributions to original knowledge and possible future directions.

1.5. References

1. Sloan, E.D. and C.A. Koh, *Clathrate hydrates of natural gases*. 2008, Boca Raton, FL: CRC Press.
2. Parrish, W.R. and J.M. Prausnitz, *Dissociation pressures of gas hydrates formed by gas mixtures.* Industrial & Engineering Chemistry Process Design and Development, 1972. **11**(1): p. 26-35.
3. Aman, Z.M. and C.A. Koh, *Interfacial phenomena in gas hydrate systems.* Chemical Society Reviews, 2016. **45**(6): p. 1678-1690.
4. Koh, C.A., et al., *Fundamentals and applications of gas hydrates.* Annual Review of Chemical and Biomolecular Engineering, 2011. **2**(1): p. 237-257.
5. Alavi, S. and R. Ohmura, *Understanding decomposition and encapsulation energies of structure I and II clathrate hydrates.* The Journal of Chemical Physics, 2016. **145**(15): p. 154708.
6. Sloan, E.D., *Fundamental principles and applications of natural gas hydrates.* Nature, 2003. **426**(6964): p. 353-363.
7. B. Klauda, J. and S. I. Sandler, *Phase behavior of clathrate hydrates: a model for single and multiple gas component hydrates.* Chemical Engineering Science, 2003. **58**(1): p. 27-41.
8. Ginley, D.S. and D. Kahen, *Fundamentals of materials for energy and environmental sustainability*. 2012, Cambridge; New York: Cambridge University Press.

9. Riedel, M., E.C. Willoughby, and S. Chopra, *Geophysical characterization of gas hydrates*. 2010, Tulsa, OK: Society of Exploration Geophysicists.

10. Lin, W., A. Delahaye, and L. Fournaison, *Phase equilibrium and dissociation enthalpy for semi-clathrate hydrate of CO2 + TBAB.* Fluid Phase Equilibria, 2008. **264**(1–2): p. 220-227.

11. Giavarini, C. and K. Hester, *Gas hydrates : immense energy potential and environmental challenges.* 2011.

12. Chialvo, A.A., M. Houssa, and P.T. Cummings, *Molecular dynamics study of the structure and thermophysical properties of model sI clathrate hydrates.* The Journal of Physical Chemistry B, 2002. **106**(2): p. 442-451.

13. Englezos, P. and J.D. Lee, *Gas hydrates: a cleaner source of energy and opportunity for innovative technologies.* Korean Journal of Chemical Engineering, 2005. **22**(5): p. 671-681.

14. Klauda, J.B. and S.I. Sandler, *Global distribution of methane hydrate in ocean sediment.* Energy & Fuels, 2005. **19**(2): p. 459-470.

15. Fandiño, O. and L. Ruffine, *Methane hydrate nucleation and growth from the bulk phase: Further insights into their mechanisms.* Fuel, 2014. **117, Part A**: p. 442-449.

16. Carroll, J.J., *Natural gas hydrates: a guide for engineers.* 2003.

17. Hawtin, R.W., D. Quigley, and P.M. Rodger, *Gas hydrate nucleation and cage formation at a water/methane interface.* Physical Chemistry Chemical Physics, 2008. **10**(32): p. 4853-4864.

18. Ballard, A. and E. Sloan, *Hydrate phase diagrams for methane+ ethane+ propane mixtures.* Chemical Engineering Science, 2001. **56**(24): p. 6883-6895.

19. Makogon, I.F., *Hydrates of hydrocarbons*. 1997, Tulsa, Okla.: PennWell Books.

20. Tanaka, R., R. Sakemoto, and R. Ohmura, *Crystal growth of clathrate hydrates formed at the interface of liquid water and gaseous methane, ethane, or propane: variations in crystal morphology.* Crystal Growth & Design, 2009. **9**(5): p. 2529-2536.

21. Ballard, A. and E. Sloan, *The next generation of hydrate prediction: Part III. Gibbs energy minimization formalism.* Fluid phase equilibria, 2004. **218**(1): p. 15-31.

22. Klauda, J.B. and S.I. Sandler, *Ab initio intermolecular potentials for gas hydrates and their predictions.* The Journal of Physical Chemistry B, 2002. **106**(22): p. 5722-5732.

23. Klauda, J.B. and S.I. Sandler, *A fugacity model for gas hydrate phase equilibria.* Industrial & Engineering Chemistry Research, 2000. **39**(9): p. 3377-3386.

24. Klauda, J.B. and S.I. Sandler, *Modeling gas hydrate phase equilibria in laboratory and natural porous media.* Industrial & Engineering Chemistry Research, 2001. **40**(20): p. 4197-4208.

25. Klauda, J.B. and S.I. Sandler, *Predictions of gas hydrate phase equilibria and amounts in natural sediment porous media.* Marine and Petroleum Geology, 2003. **20**(5): p. 459-470.

26. Ballard, A.L. and E.D. Sloan Jr, *The next generation of hydrate prediction: I. hydrate standard states and incorporation of spectroscopy.* Fluid Phase Equilibria, 2002. **194–197**: p. 371-383.

27. Zhao, J., et al., *Microstructural characteristics of natural gas hydrates hosted in various sand sediments.* Physical Chemistry Chemical Physics, 2015. **17**(35): p. 22632-22641.

28. Sun, C.Y., et al., *Studies on hydrate film growth.* Annual Reports Section "C" (Physical Chemistry), 2010. **106**(0): p. 77-100.

29. Servio, P. and P. Englezos, *Morphology of methane and carbon dioxide hydrates formed from water droplets.* AIChE Journal, 2003. **49**(1): p. 269-276.

30. Asserson, R.B., et al., *Interfacial tension measurement of freon hydrates by droplet deposition and contact angle measurements.* Journal of Petroleum Science and Engineering, 2009. **68**(3–4): p. 209-217.

31. Sloan, E.D., *Natural gas hydrates in flow assurance.* 2011.

32. Kashchiev, D., *Nucleation: basic theory with applications.* 2000.

33. Kashchiev, D. and A. Firoozabadi, *Nucleation of gas hydrates.* Journal of Crystal Growth, 2002. **243**(3–4): p. 476-489.

34. Kashchiev, D. and A. Firoozabadi, *Driving force for crystallization of gas hydrates.* Journal of Crystal Growth, 2002. **241**(1–2): p. 220-230.

35. Kashchiev, D. and A. Firoozabadi, *Induction time in crystallization of gas hydrates.* Journal of Crystal Growth, 2003. **250**(3–4): p. 499-515.

36. Bai, D., et al., *How properties of solid surfaces modulate the nucleation of gas hydrate.* Scientific Reports, 2015. **5**: p. 12747.

37. Koga, T., et al., *Hydrate formation at the methane/water interface on the molecular scale.* Langmuir, 2010. **26**(7): p. 4627-4630.

38. Firoozabadi, A., *Thermodynamics of hydrocarbon reservoirs*. 1999, New York: McGraw-Hill.

39. Vázquez, U.O.M., et al., *Calculating the surface tension between a flat solid and a liquid: a theoretical and computer simulation study of three topologically different methods.* Journal of Mathematical Chemistry, 2009. **45**(1): p. 161-174.

40. Binks, B.P. and J.H. Clint, *Solid wettability from surface energy components: relevance to pickering emulsions.* Langmuir, 2002. **18**(4): p. 1270-1273.

41. Grimvall, G., *Chapter 6 - The phonon spectrum*, in *Thermophysical Properties of Materials*. 1999, Elsevier Science B.V.: Amsterdam. p. 79-111.

42. Jager, M., A. Ballard, and E. Sloan, *The next generation of hydrate prediction: II. dedicated aqueous phase fugacity model for hydrate prediction.* Fluid phase equilibria, 2003. **211**(1): p. 85-107.

43. Arora, A., et al., *Biosurfactant as a Promoter of Methane Hydrate Formation: Thermodynamic and Kinetic Studies.* Scientific Reports, 2016. **6**: p. 20893.

44. PAL, S. and T.K. KUNDU, *DFT-based inhibitor and promoter selection criteria for pentagonal dodecahedron methane hydrate cage.* Journal of Chemical Sciences, 2013. **125**(5): p. 1259-1266.

45. Heeschen, K.U., J.M. Schicks, and G. Oeltzschner, *The promoting effect of natural sand on methane hydrate formation: grain sizes and mineral composition.* Fuel, 2016. **181**: p. 139-147.

46. Moon, C., P.C. Taylor, and P.M. Rodger, *Clathrate nucleation and inhibition from a molecular perspective.* Canadian Journal of Physics, 2003. **81**(1-2): p. 451-457.

47. Carver, T.J., M.G.B. Drew, and P.M. Rodger, *Inhibition of crystal growth in methane hydrate.* Journal of the Chemical Society, Faraday Transactions, 1995. **91**(19): p. 3449-3460.

48. Perfeldt, C.M., et al., *Inhibition of gas hydrate nucleation and growth: efficacy of an antifreeze protein from the longhorn beetle rhagium mordax.* Energy & Fuels, 2014. **28**(6): p. 3666-3672.

49. Jensen, L., K. Thomsen, and N. von Solms, *Inhibition of structure I and II gas hydrates using synthetic and biological kinetic inhibitors.* Energy & Fuels, 2011. **25**(1): p. 17-23.

50. Amtawong, J., et al., *Propane clathrate hydrate formation accelerated by methanol.* The Journal of Physical Chemistry Letters, 2016. **7**(13): p. 2346-2349.

51. Tang, C., et al., *Kinetic studies of gas hydrate formation with low-dosage hydrate inhibitors.* Science China Chemistry, 2010. **53**(12): p. 2622-2627.

52. Englezos, P., *Nucleation and growth of gas hydrate crystals in relation to "kinetic inhibition".* Revue De L Institut Francais Du Petrole, 1996. **51**(6): p. 789-795.

53. Lederhos, J.P., et al., *Effective kinetic inhibitors for natural gas hydrates.* Chemical Engineering Science, 1996. **51**(8): p. 1221-1229.

54. Zerpa, L.E., et al., *Surface chemistry and gas hydrates in flow assurance.* Industrial & Engineering Chemistry Research, 2011. **50**(1): p. 188-197.

55. Dirdal, E.G., et al., *Can cyclopentane hydrate formation be used to rank the performance of kinetic hydrate inhibitors?* Chemical Engineering Science, 2012. **82**: p. 177-184.

56. Wu, R., et al., *Effect of kinetic hydrate inhibitor polyvinylcaprolactam on cyclopentane hydrate cohesion forces and growth.* Energy & Fuels, 2014. **28**(6): p. 3632-3637.

57. Zhang, J.S., et al., *Adsorption of kinetic inhibitors on clathrate hydrates.* The Journal of Physical Chemistry C, 2009. **113**(40): p. 17418-17420.

58. Waals, J.H.v.d. and J.C. Platteeuw, *Clathrate solutions*, in *Advances in Chemical Physics*. 2007, John Wiley & Sons, Inc. p. 1-57.

59. Martín, Á., *A simplified van der Waals-Platteeuw model of clathrate hydrates with multiple ocupancy of cavities.* The Journal of Physical Chemistry B, 2010. **114**(29): p. 9602-9607.

60. Martín, A. and C.J. Peters, *New thermodynamic model of equilibrium states of gas hydrates considering lattice distortion.* The Journal of Physical Chemistry C, 2009. **113**(1): p. 422-430.

61. Brown, E., et al., *Cyclopentane hydrate cohesion measurements and phase equilibrium predictions.* Journal of Natural Gas Science and Engineering, 2016. **35, Part B**: p. 1435-1440.

62. Ji, H., et al., *Microsecond molecular dynamics simulation of methane hydrate formation in humic-acid-amended sodium montmorillonite.* Energy & Fuels, 2016. **30**(9): p. 7206-7213.

63. Kuznetsova, T., B.r. Kvamme, and A. Parmar, *Molecular dynamics simulations of methane hydrate pre-nucleation phenomena and the effect of PVCap kinetic inhibitor.* AIP Conference Proceedings, 2012. **1504**(1): p. 776-779.

64. Kvamme, B., T. Kuznetsova, and K. Aasoldsen, *Molecular dynamics simulations for selection of kinetic hydrate inhibitors.* Journal of Molecular Graphics and Modelling, 2005. **23**(6): p. 524-536.

65. Kvamme, B.B., G. Huseby, and O.K. Forrisdahl, *Molecular dynamics simulations of PVP kinetic inhibitor in liquid water and hydrate/liquid water systems.* Molecular Physics, 1997. **90**(6): p. 979-992.

66. Walsh, M.R., et al., *Microsecond simulations of spontaneous methane hydrate nucleation and growth.* Science, 2009. **326**(5956): p. 1095-1098.

67. Yan, K.-F., et al., *Molecular dynamics simulation of the crystal nucleation and growth behavior of methane hydrate in the presence of the surface and nanopores of porous sediment.* Langmuir, 2016. **32**(31): p. 7975-7984.

68. Katsumasa, K., K. Koga, and H. Tanaka, *On the thermodynamic stability of hydrogen clathrate hydrates.* The Journal of Chemical Physics, 2007. **127**(4): p. 044509.

69. Luis, D.P., A. Garcia-Gonzalez, and H. Saint-Martin, *A theoretical study of the hydration of methane, from the aqueous solution to the sI hydrate-liquid water-gas coexistence.* International Journal of Molecular Sciences, 2016. **17**(6).

70. Papadimitriou, N.I., et al., *Evaluation of the hydrogen-storage capacity of pure H2 and binary H2-THF hydrates with Monte Carlo simulations.* The Journal of Physical Chemistry C, 2008. **112**(27): p. 10294-10302.

71. Papadimitriou, N.I., et al., *Storage of methane in clathrate hydrates: Monte Carlo simulations of sI hydrates and comparison with experimental measurements.* Journal of Chemical & Engineering Data, 2016. **61**(8): p. 2886-2896.

72. Papadimitriou, N.I., I.N. Tsimpanogiannis, and A.K. Stubos. *Monte Carlo simulations of methane hydrates*. in *Proceedings of the 7th International Conference on Gas Hydrate, Edinburgh, Scotland*. 2011.

73. Frenkel, D. and B. Smit, *Understanding molecular simulation: from algorithms to applications.* 2002.

74. Jensen, F., *Introduction to computational chemistry*. 2007, Chichester, England; Hoboken, NJ: John Wiley & Sons.

75. Br·zdov·, V. and D.R. Bowler, *Atomistic computer simulations: a practical guide.* 2013.

76. Hinchliffe, A., *Chemical modeling: from atoms to liquids*. 1999, Chichester; New York: Wiley.

77. Rapaport, D.C., *The art of molecular dynamics simulation.* 2004.

Chapter 2. Molecular Dynamics Characterization of Temperature and Pressure Effects on the Water-Methane Interface

2.1. Preface

In this chapter, the interfacial tension between the methane gas and liquid water phases is investigated over a wide range of temperature and pressure using a novel ensemble in molecular dynamics. The key mechanisms such as adsorption and hydrogen bonding, which control the surface tension are identified, and a classical thermodynamic law scaling the tension change with temperature is presented. This chapter is reproduced with permission from "Mirzaeifard, S., P. Servio, and A.D. Rey, Molecular dynamics characterization of temperature and pressure effects on the water-methane interface. Colloid and Interface Science Communications, 2018. 24: p. 75-81".

2.2. Abstract

The water-methane interface plays an important role in mass transfer between the phases. In this work, we employ molecular dynamics to investigate and characterize the mechanics, thermodynamics, and composition of water-methane interfaces applying a unique methodology known as the NP_NAT ensemble. We systematically increase the pressure (1-50 MPa) and temperature (25-105^{o}C) to calculate the interfacial tension from its mechanical definition. We predict the surface tension via pressure and temperature relations in agreement with the classical scaling laws such as the Eötvös rule. It is found that the surface adsorbs methane molecules as per high interfacial excess and local density of methane. The methane practically remains insoluble in water due to favorable interactions with a dense hydrogen bonded region near the surface. The obtained macroscopic interfacial tension properties and sensitivity to pressure and temperature and the corresponding molecular mechanisms contribute to the evolving understanding and practical applications of this important interface.

2.3. Keywords

water-methane mixture; surface tension; molecular dynamics simulation; NPNAT ensemble

2.4. Introduction

Interfacial thermodynamics and transport phenomena are central to many engineering and chemical processes. In particular, the interfacial tension drives the mass transport across the interface and significantly influences the capillary pressure governing the fluid transport in petroleum reservoirs, which is considered vital for the exploration, production, and high pressure processes [1, 2]. The interfacial tension mainly depends on structural and thermodynamic properties such as pressure, temperature, and chemical compositions, which are currently poorly understood but cannot be ignored in the study of aqueous mixtures which contains water and gaseous alkanes [3]. As fossil energy resources are diminishing, we need to optimize extraction and use processes based on molecular-level understanding of the physical properties of hydrocarbon-water systems.

Water-methane interfaces are ubiquitous as the latter is the most common and lightest component of the natural gas. The interaction of co-exiting methane and water bulk phases in natural and industrial environments might cause the formation of clathrate hydrates promoting the motives of our work [4]. Clathrate hydrates, gas hydrates, or simply hydrates are ice-like crystalline solids that consist of water molecules stable cages (cavities), called hosts. The gas molecule, which is effectively compressed inside of the water cage is the guest or hydrate former. Gas hydrates have a wide range of applications in different industries including: flow assurance, transportation, new energy resources, gas storage, environmental crisis like global warming arisen by release of methane gas [4-6]. Hydrate formation process typically initiates at the surface, whose materials physics are not well understood [7]. Classical nucleation theory postulates the formation of a new cluster phase consisting of n crystal unit cells which needs work to compensate for the energy consumed for a combination of interfacial energy and the creation of a new phase that occupies space. The formation work is given by [7]:

$$W(J) = -n\Delta\mu + c(nv_h)^{\frac{2}{3}}\sigma \tag{2.1}$$

where $\Delta\mu(J)$, c, v_h, and σ_{ef}(J/m^2) are supersaturation, shape factor, hydrate volume, and surface energy, respectively. For an anisotropic system, the surface energy is clearly not a scalar quantity. To obtain the interfacial energy between different phases, most significantly liquid-gas, we need a clear knowledge of the pressure tensor governing the surfaces. This knowledge is required to explain phase transitions, thermodynamic stability, morphology, nucleation, and the growth rate of gas hydrates. This is imperative in order to understand the basic theory of hydrate formation and find ways of inhibiting or promoting their formation, depending on the application. Furthermore, water-methane studies give better insight into water-heavier alkanes mixtures due to the similar nature of interfacial interactions such as surface tension which is predominantly influenced by molecular structure than weight.

In distinction to the bulk region, interfacial atoms and molecules are not strongly bound, allowing for molecular re-organizations at the interface [3] demanding new experimental, computational, and theoretical characterization techniques. Experimentally, it is difficult to measure surface tension in perfect samples with controlled purity. Moreover, experiments typically require high pressure for hydrate formation, which are extremely difficult and involve expensive instrumentation. Generally, surface energy cannot be precisely obtained from only experiments [8, 9]. In addition, we need microscopic understanding of the system, which experimental work lacks, leaving molecular simulations as a very effective option to provide all the necessary information concerning the interfacial regions. Likewise, computer simulations encounter their own challenges when the system contains liquid-gas interfaces. First, the interface separating liquid and gas phases is extremely thin leading to essential discontinuities in macroscopic fields. Second, local densities largely change across the interface. Liquids have high density with constant volume in addition to spontaneous interfacial contraction, while gases develop an apparent elastic skin with large molecular mobility in much lower density regimes. Third, the interface imposes a localized surface tension force on the liquid phase. Fourth, we experience a phase transition and topology changes at the interface, which import disturbance and poor statistics into the system properties relative to the number of molecules. Lastly, time and length scales should be sufficiently long to tailor realistic models. The most important challenge is to narrow the gap between experiments, theory and simulation predictions on interfacial tension and its dependence on temperature and pressure.

This challenge is even more highlighted for the water-methane systems. Even in the most stable conditions, the water-hydrophobic gas surface is not flat showing nanoscopic waves scattering light with low intensity. The ionization properties, dipole moment, and dielectric permittivity of water phase vary from its bulk to surface over infinitesimal distances. The organization of water molecules at the surface simply adapts with thermodynamic parameters and ions binding. Furthermore, robust hydrogen bonding and charges holding between molecules complicate water mixtures. In general, liquid water in contact with gas or solid phase exhibits two distinct thermodynamic behaviors at the interface and bulk [10, 11].

In recent years, with the use of very powerful computing resources and improved computational models, molecular simulation techniques can leverage theoretical tools combined with statistical mechanics to accurately capture the dynamics of interfacial systems at length and time scales difficult to access experimentally. In this paper, we use molecular dynamic (MD) techniques in conjunction with interfacial thermodynamics of gas-liquid interfaces and surface physics to provide an accurate characterization of the complex water-methane-interface as a function of temperature and applied pressure. In particular, classical scaling laws of utility to applications are derived and the molecular underpinnings are revealed.

Use of powerful computing resources allows utilization of sufficiently long time and length scales to mimic realistic models. The key aspect of the MD approach is to completely control a pure water-methane mixture with no external disturbances, as opposed to experiments, to investigate the thermodynamics and mechanics of the system. We can observe macromolecular structures to better understand the physics and theory behind the phase transitions from microscopic to macroscopic level. With molecular dynamics, we can also readily obtain the crucial interfacial tension parameters from stress tensor analysis and characterize the temperature and pressure effects.

In an aniso-diametric system, the physical and thermodynamic parameters such as the local density are not uniform along the normal direction to the planar surface. One of the challenges in the calculation of the interfacial tension is to address an appropriate statistical ensemble as we intend to predict sensible values. In the *NVT* ensemble the system volume should be adjusted manually, consequently, great knowledge over the system volume at equilibrium is always required. On the other hand, the standard *NPT* ensemble cannot properly predict the interfacial tension as the tangential pressure is negative and not constant along the interface. The pressure cannot be chosen to be isotropic for systems with multiple phases, whose interfaces have thermodynamic differences between the lateral and normal directions. Therefore, conventional *NVT* and *NPT* ensembles are not precise enough for interfacial tension calculations. We need specific ensembles that controls the pressure across the system to avoid the disturbances in the interfacial area. To obtain sensible values, we use the NP_NAT ensemble, since we cope with a constant normal pressure P_N imposed to the planar surface with a specific cross sectional area (A). This novel ensemble provides the most reliable predictions of liquid-gas systems [12, 13] and lipid membranes in cell biology [14]. In recent computational studies, the thermodynamic definition is used to calculate the surface tension of mixtures [15, 16]. According to this definition, the interfacial tension is the derivative of the free energy with respect to the interfacial area. This method effectively estimates more global than local properties [17], even though we intend to study the system from both perspectives. Besides, the NP_NAT ensemble holds the interfacial area static throughout the simulations. Hence, the thermodynamic definition is unable to predict the interfacial tension. Herein, we use the local components of the stress tensor to follow the Kirkwood and Buff method for calculating the interfacial tension (γ_{KB}) from the mechanical definition at the water-methane interface [18].

The organization of this paper is as follows. In the next section, we describe the model and briefly state the computational MD simulations details. In addition, we elaborate on the novel approach for interfacial tension calculation. In the results section, we discuss the pressure and temperature effects on the interfacial density, tension, thickness, and molecular composition. Lastly, the main conclusions and their significance are presented.

2.5. Model and Simulation Methods

In this work, we use molecular dynamics simulations to study the classical thermodynamic behavior of the water-methane mixture at various pressures and temperatures. To calculate the interfacial tension, we follow the common computational method that confines the liquid water phase between two methane gas phases [18, 19]. We model the simulation box with an initial size of 36×36×120 Å in three dimensions. Knowledge of the initial value for the box length in the z direction (L_z) is not required as L_z can freely fluctuate, adjusting the system volume to reach the prescribed bulk density for each phase. Fixing box lengths in the x and y dimensions with independent dilation or contraction in only the z dimension provides a constant cross section (i.e., $A = L_x L_y$), essential for the NP_NAT ensemble [20]. To reach the desired target pressure, the system volume, and consequently, the coexisting densities of the components should be able to change towards equilibration. Periodic boundary conditions are applied throughout. We randomly place 3710 water molecules in a slab in the middle of the simulation box and surround this slab with 200 methane molecules on both sides. Figure 2.1 shows a snapshot of a typical initial configuration of the system. To model the force field for water and methane molecules, we use the transferable intermolecular potential with the four points (TIP4P) model [21] and united atom optimized potentials for liquid simulations (OPLS-UA) model [22], within the LAMMPS simulation package

[23]. We use the Lennard-Jones (LJ) potential with Lorentz-Berthelot mixing rules to represent the intermolecular interactions:

$$U_{LJ}(r) = 4\varepsilon\left[\left(\frac{\sigma}{r}\right)^{12} - \left(\frac{\sigma}{r}\right)^{6}\right] \tag{2.2}$$

In the Lorentz-Berthelot approach, an arithmetic mixing rule calculates the essential LJ parameters for the unlike particles, as given below:

$$\varepsilon_{ij} = \sqrt{\varepsilon_{ii}\varepsilon_{jj}} \tag{2.3}$$

$$\sigma_{ij} = \frac{\sigma_{ii}+\sigma_{jj}}{2} \tag{2.4}$$

where ε, σ, and r are the depth of the potential well, the finite distance with zero potential, and the distance between the particles, respectively.

We apply the particle-particle particle-mesh (PPPM) technique introduced by Hockney and Eastwood [24, 25] with an accuracy of 10^{-5} for the errors in force calculations to obtain the Coulombic electrostatic interactions. The cut-off distance for LJ and short range electrostatic interactions are 12Å and partial electron charges, the distance and the angles between atoms or charge sites, and LJ potential parameters used for the simulation can be found in Table 2.1 [21, 22]. Furthermore, we use the Shake algorithm to apply an additional constraining force to the specified bonds and angles associated with the water molecules. This force guarantees the OH bond length and the HOH angle remain constant throughout the simulations.

Table 2.1. Simulation parameters including: partial electron charges, distance and angles between atoms or charge sites, and Lennard-Johns potential well depth (ε) and finite distance (σ).

	Mass(g/mol)	σ(Å)	ε(Kcal/mol)	charge(e)
O	15.9994	3.16435	0.16275	-1.0484
H	1.008	0	0	0.5242
CH_4	16.0425	3.73	0.29391	0
OH bond length		0.9572		
HOH angle		104.52		
OM distance		0.125		

We then integrate the non-Hamiltonian equations of motion by using the Verlet algorithm and velocity rescaling for temperature control to sample the particles positions and velocities from the

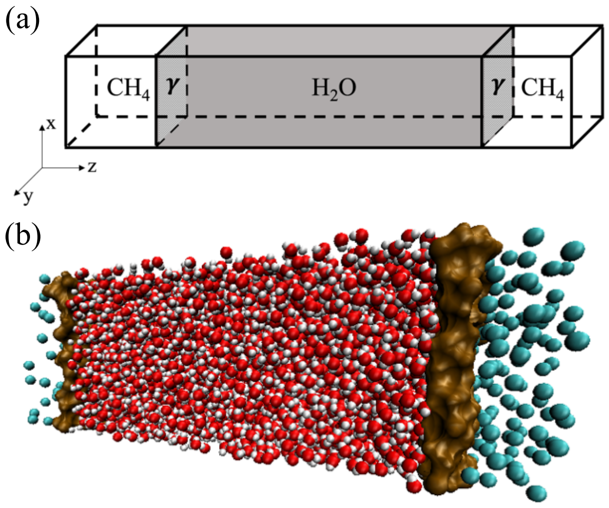

Figure 2.1. (a) Schematic showing one grey zone containing the water molecules and two white zones containing the methane molecules to form the liquid and gas phases, respectively. (b) Initial configuration of the system. The green, red, and white particles represent the methane molecules, the oxygen atoms, and the hydrogen atoms, respectively. Two brown regions represent the interfaces between the liquid and gas phases.

desired ensemble. The pressure and temperature are then regulated and include the inherent fluctuations using Nosé-Hoover thermostat and Parrinello-Rahman barostat, which couple some dynamic variables to the equations of motion. The time step is fixed at 2 fs and all simulations are performed for 4 ns in order to reach equilibrium. This simulation time is set sufficiently long to provide accurate results for the surface tension as opposed to previous MD studies. The damping constant for temperature and pressure regulation is chosen to be 4 ps. We estimate that the system reaches equilibration during the first 3 ns since there is no significant change in the behavior of the thermodynamic and mechanical properties such as temperature and pressure. The correlation factor calculated for the system energy rapidly approaches zero to support the equilibrium state. In the last 1 ns of the simulations, once the equilibration is assured, we begin to collect the simulation outcome for further analysis.

According to the Kirkwood and Buff method, the surface tension for a system with a density gradient in the z direction is obtained from:

$$\gamma_{KB} = \int_{-\infty}^{+\infty} \left(P_N - P_T(z)\right) dz, \tag{2.5}$$

where P_N and P_T are the normal pressure and tangential pressure, respectively, and the integral is calculated over the interfacial thickness. The values for P_N and P_T can be calculated from the stress tensor [26]:

$$P_N = P_{zz} = P \tag{2.6}$$

$$P_T = \frac{1}{2}\left(P_{xx} + P_{yy}\right) \tag{2.7}$$

Subsequently, the surface tension is given by:

$$\gamma_{KB} = \int_{-\infty}^{+\infty} \left[P_{zz} - \frac{1}{2}\left(P_{xx} + P_{yy}\right)\right] dz \tag{2.8}$$

Ignoring the slight computational fluctuations, the normal and tangential pressures are constantly equal to the total pressure along the simulation box, except for the interface. The tangential pressure drastically decreases at the interface resulting in a nonzero positive value for the surface tension. Nevertheless, the surface tension obtained from the mechanical definition (Eqn. 2.8) underestimates its value owing to truncations in the interatomic interactions, particularly in inhomogeneous systems [27-29]. The cut-off distance in the LJ potential calculations diminishes the value for the surface tension in an analogous manner that attenuates the bulk pressure with a constant density. Therefore, multicomponent systems where all their components are present in all the phases require a long-range or tail correction in the interfacial energy calculation. Chapela et al. [29] introduced a well-known formula, later improved by Blokhuis et al. [28], for the tail correction to compensate for this inaccuracy:

$$\gamma_{tail} = \int_0^1 \int_{r_c}^{\infty} 12\pi\varepsilon\sigma^6 \left(\rho_l - \rho_g\right)^2 \left(\frac{3s^3 - s}{r^3}\right) cot\left(\frac{rs}{d}\right) dsdr, \tag{2.9}$$

where r_c, s, d, and ρ_g and ρ_l are the cut-off distance, position, interfacial thickness, and molecular densities of the gas and liquid phases, respectively. Hence, the interfacial tension (γ) adopted in this work is:

$$\gamma = \gamma_{KB} + \gamma_{tail} \tag{2.10}$$

2.6. Results and Discussion

To calculate the interfacial tension based on the mechanical definition, we need to divide the simulation box into small slabs (i.e., cuboids with equal lengths in x and y dimensions) and subtract the normal and the tangential pressure values obtained from the components of the stress tensor in each slab. As mentioned above, the system stability requires the normal and tangential pressures to remain constant and negative at the interface, respectively, allowing the interfacial tension to achieve a positive value. However, the normal and tangential pressure difference reveals two negative peaks near the water phase, appearing on both interfaces (left and right), which implies an edge compression regime [30-32]. This compression regime is relatively small compared to the tension regime. Previous researches reported different potential sources triggering the compression: the nature of the interfaces [31, 32], interfacial polarization [33], the choice of the force field with LJ and electrostatic truncation scheme [13, 34], or unphysical values originated from inevitable simulations errors [17, 35]. Nevertheless, the existence of such a compression zone is not yet fully understood and its full resolution and complete understanding is beyond the scope of this work.

The nonuniform behavior in the z dimension, particularly close to the interface, demands an increase in the slab size and average the macroscopic parameters to maintain the system stabilization. As we systematically increase the slab size from 0.1Å to 12Å or the temperature from 25^{o}C to 105^{o}C, the negative peaks associated with the presumed compression regimes weaken. Figure 2.2 depicts how the slab size changes the normal and tangential pressure difference leading us to use average stress tensor components for the surface tension calculation as given below. It is noted that we divide the integral (Eqn. 2.5) by two as two interfaces appear between water and methane molecules along the simulation box:

$$\gamma = \frac{L_Z}{2}\left[\langle P_z\rangle - \frac{1}{2}\left(\langle P_{xx}\rangle + \langle P_{yy}\rangle\right)\right] + \gamma_{tail} \tag{2.11}$$

On the other hand, the presence of two maximum peaks indicates that the system configuration is well defined to include two independent liquid-gas surfaces, while the tonsorial components of the pressure in the bulk phases are not involved in the interfacial energy calculation.

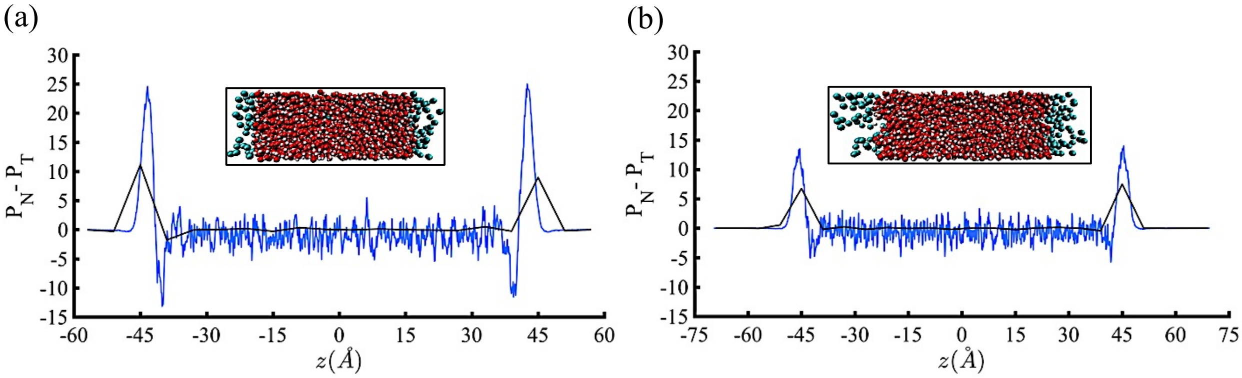

Figure 2.2. Choosing different size for the slabs changes the difference of the normal and tangential pressures (reported in units of mN/m^2). This change might even lead to unreliable surface tension values. Blue and black lines represent the simulations with the slab lengths of 0.1Å and 6Å (as example) in the z dimension, respectively. The pressure of the system is 10 MPa and the temperatures are 25°C (a) and 105°C (b). In addition, the blue line in plot (b) clearly shows how increasing temperature damps the two negative edge peaks associated with compression [30,32].

The mass density is now characterized to better understand the temperature and pressure effects on the interfacial molecular-level behavior, noting that an accurate density profile from experiments may not be trivial. We also require the density profile for both water and methane phases to include tail corrections. The temperature is then systematically incremented from 25°C to 105°C (Figure 2.3). In summary, a sudden expansion initially occurs in the z dimension, which causes the local mass density of both components to dramatically decrease at the interface until the system is sufficiently expanded to allow the local densities to fluctuate around an approximate plateau. In contrast with the effect of temperature, increasing the system pressure compresses both phases leading to larger local densities. This enlarging shift is almost negligible on the water side suggesting pressure independency. The compressive forces predominantly impact the gas components as expected, which implies preferred adsorption of methane molecules on the water phase. Additionally, we fit the density profiles with hyperbolic tangent functions to obtain the surface excess (Γ) at 25°C from [36]:

$$\Gamma\ (\mathrm{mol}/m^2) = \frac{1}{A}\int_{-\infty}^{\infty}\{\rho_m(z) - \rho_{m,l}\Theta(-z) - \rho_{m,v}\Theta(z)\}\,dz, \tag{2.12}$$

where ρ_m, $\rho_{m,l}$, $\rho_{m,v}$, and $\Theta(z)$ are the methane density profile, bulk density in water and methane phases, and Heaviside step function, respectively. The calculated surface excesses of 2.8×10^{-6} and 3.5×10^{-6} mol/m^2 at 10 and 15 MPa, respectively, in combination with increase of methane local density, suggest ideal methane enrichment in the surface. This dense methane film can explain lower interfacial energy by the Gibbs equation compared to the pure water liquid-vapor system. A similar trend can be obtained for the methane density profile in systems in a lower temperature regime. For instance, the surface excess of methane at 0°C and 10 MPa is 3.9×10^{-6} mol/m^2, which reveals more noticeable methane adsorption onto the surface. This anomalous adsorption suggests heterogeneous nucleation for methane hydrate, which occurs at the surface.

With robust knowledge of the interfacial density profile, we can now calculate the interfacial tension between the liquid and gas phases from Eqn. 2.11. Figure 2.4 shows that the interfacial tensions of the water-methane mixture from MD simulations are in very good agreement with experiments and previous computational work. The average absolute deviations (AAD) are in a range of 1.38% to 5.59% computed from the given formula:

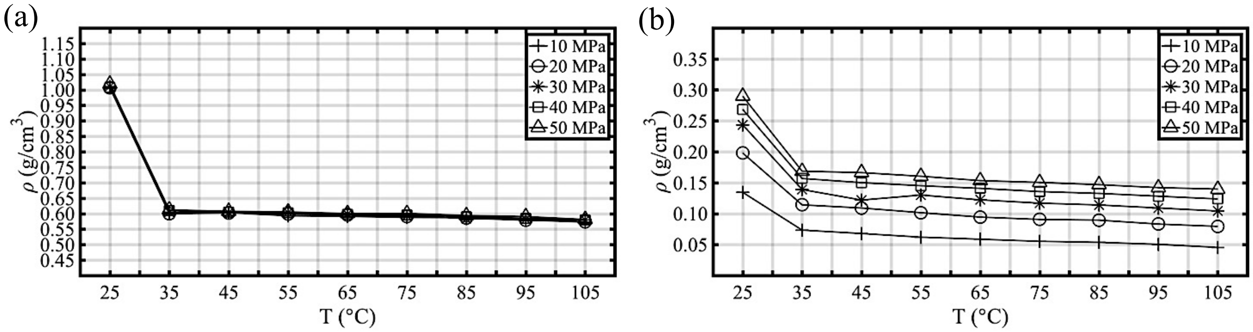

Figure 2.3. The plots depict the values for the local density (g/cm^3) of the water (a) and methane (b) molecules at the interface versus the temperature (°C) of the system. When the system is exposed to a temperature upturn, a sudden decrease is observed for the local density of both components, especially in the systems with higher pressure regime (>30 MPa).

$$AAD = \frac{1}{N}\sum_{i=1}^{N}\left|\gamma_i - \langle\gamma_{ref}\rangle\right|\times 100, \tag{2.13}$$

where $\langle\gamma_{ref}\rangle$ and N denote the mean value and the number of references, respectively. Since molecular dynamics is a very sensitive technique to pressure, the systems in low pressure regime (<5 MPa) show further pressure fluctuations leading to instabilities, whereas the high-pressure regime (>10 MPa) have been commonly accepted to provide more reliable results, particularly in liquid and solid phases.

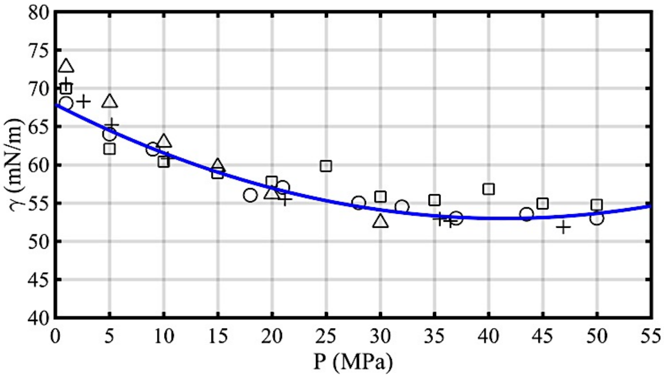

Figure 2.4. Surface tension (mN/m) at the temperature of 25^{o}C with increasing the system pressure (MPa). The plus sign, triangle, circle, and square markers denote the data obtained from the experiments by Sachs et al. and Sun et al., simulation, and present work (with blue fitting curve), respectively [36-38].

When the systems are compressed, two separated liquid and gas phases are forced to merge with each other with more condensed interfaces. Therefore, we expect the surface to lose its tension with increasing system pressure. Figure 2.4 demonstrates an approximately quadratic decrease in surface tension with pressure, in agreement with both experiments and simulations [36-38]. This decreasing trend of the interfacial tension disappears at pressure greater than 50 MPa, and subsequently the interface displays a slight tension increase with pressure upturn. The region of decreasing tension is fitted with the following quadratic polynomial (units reported in the figure):

$$\gamma(mN/m) = 0.0087\,P^2 - 0.72\,P + 68 \qquad (2.14)$$

The 10-90 Å interfacial thickness (t) is representative of the surface thickness found in ellipsometric and x-ray reflectivity experiments [39, 40], which is 2.1972 times larger than the physical thickness (d) [41]. We obtain the physical thickness d(Å) from the hyperbolic tangent fitting curve of density profile:

$$\rho(z) = \frac{1}{2}\rho_b\left(1 - \tanh\frac{|z-z_c|-z_G}{d}\right) \qquad (2.15)$$

where ρ_b, z_c, and z_G represent the bulk density, the center of interface, and the Gibbs dividing surface position. The physical thickness can also be calculated from fundamental thermodynamic relations:

$$d(\text{Å}) = \left|\frac{\partial G}{\partial P}\right|_{A,T} = \left|\frac{\partial\gamma(mN/m)}{\partial P(MPa)}\right|_{A,T}\left(\frac{10^{-9}MPa}{1mN/m^2}\right)\left(\frac{10^{10}\text{Å}}{1m}\right) = |0.174\,P(MPa) - 7.2| \qquad (2.16)$$

Please note that in deriving this equation using Eqn. 2.14 we include conversion factors for pressure and distance. The interfacial thickness obtained from these two methods at 25°C and 10 MPa has only 5.4% deviation indicating a theoretical validation for our simulations. To evaluate the temperature and pressure effects on the interface, we report the associated thickness and box length. Figure 2.5 shows that interfacial thickness *t* and box length L_z substantially depend on the thermodynamic conditions of the system. L_z can largely expand and adapt as we increase the temperature. Moreover, the system can reveal larger compression in both *t* and L_z along with increasing pressure. This effect of the pressure might persist so long as the system retains the conditions pertaining to its compressibility.

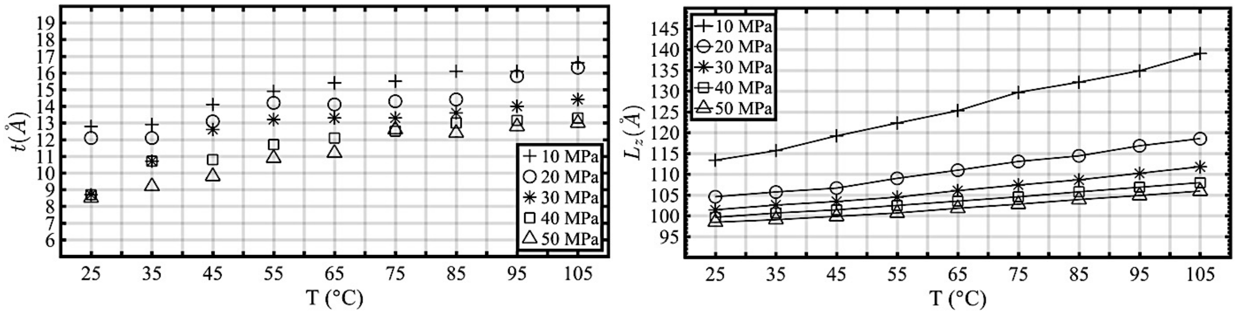
(a)

(b)

Figure 2.5. Increasing the temperature reveals an increase in interfacial thickness *t* (a) and, more effectively, L_z (b) at 10, 20, 30, 40, and 50 MPa. The systems at higher temperatures better manifest the box length elongation.

In addition to pressure, the interfacial tension significantly depends on the temperature of the system. When the temperature increases, the cohesive forces acting between the water molecules decrease, subsequently the interfacial tension decreases so that it approaches zero at the critical point. Figure 2.6 clearly shows this trend for the surface tension with rising temperature at constant pressure. In a system with constant pressure and cross-sectional area, a quadratic function of the temperature (K) can approximately estimate the interfacial tension:

$$\gamma(mN/m) = 0.000069\,T^2 - 0.22\,T + 120 \tag{2.17}$$

Since the second order term is almost negligible, we assume that the fitted curve is a linear function to compare the results with the classical scaling laws. Therefore, a master curve is constructed to correlate the interfacial tension and temperature with a classical equation in an improved form of the Eötvös rule given by Ramsay and Shields [42]:

$$\gamma V^{2/3} = k(T_c - T - 6), \tag{2.18}$$

where V, T_c, and k are the molar volume, critical temperature of the mixture, and Eötvös constant which is equal to 2.1×10^{-7} J/K.mol$^{2/3}$, respectively. The following linear fit reports the surface tension in units of mN/m at 10 MPa when the temperature is given in degrees K:

$$\gamma = -0.23\,T + 129.4 \tag{2.19}$$

The binary mixture requires the molar volume of 28.37 cm^3 and the critical temperature of 573.26 K to complement the fitting line. If we assume the mixture is ideal, these computed values also match the molar volume and the critical temperature of the mixture obtained from the mixing

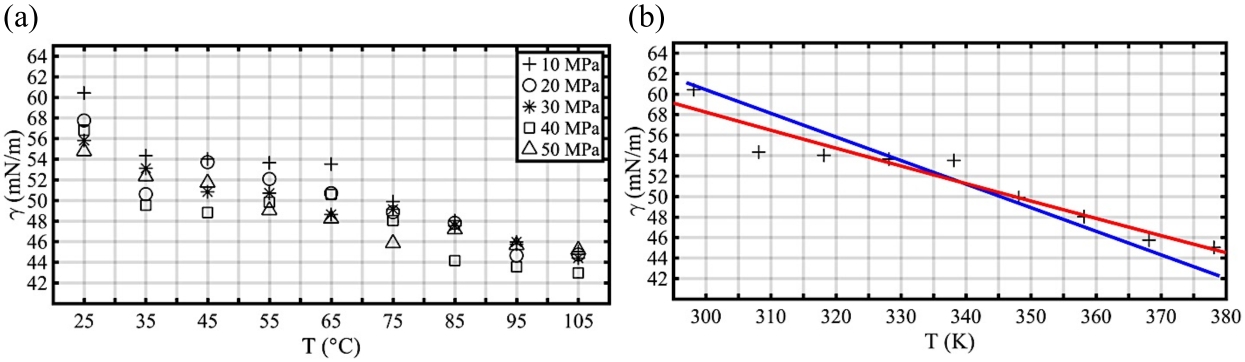

Figure 2.6. The plot (a) depicts the inverse behavior of the interfacial tension (mN/m) versus temperature (^{o}C). Blue and red lines in the plot (b) display the linear and quadratic master curves, respectively, which fit the interfacial tension at 10 MPa and different temperatures (K) and whose slopes estimate the surface entropy.

rules [43]. We note that this fitted linear function might only predict the surface tension in the specific range of pressures and temperatures as we do not examine the other factors including molecular structure, orientation, and polarity under different thermodynamic conditions.

The surface entropy (S) can be calculated from the summation of two terms associated with the enthalpy and isobaric heat capacity of the system [44]. Utilizing a more efficient approach, we assume the surface entropy only depends on the temperature at relatively constant pressure and compute it from the fundamental thermodynamic equations:

$$-S = \left(\frac{\partial G}{\partial T}\right)_{A,P} = \left(\frac{\partial \gamma}{\partial T}\right)_{A,P} \tag{2.20}$$

After unit conversion and multiplication by the area, we attain an entropy value of 117.98 kcal/mol at 275 K and 10 MPa, which shows very good agreement with a deviation of 6.07% from the previous studies [45].

Next, we characterize the chemical composition across the interface. Since we place the water bulk in the central region encompassed by methane, the water mass fraction prevails over the methane mass fraction along with a decrease in the potential energy in the central region. Figure 2.7 depicts that a pressure variation (10-50 MPa) negligibly influences the components compositions and leaves the profiles untouched, whereas it influences the local density, specifically for the methane phase. Nevertheless, increasing the temperature (25-105^{o}C) affects the methane mass fraction, particularly under the low-pressure regime. The water molecules are subject to less resistance to mobility between the phases, while lower competition from neighboring water molecules forms stronger hydrogen bonds between the polar water molecules at the surface than the bulk to interact with the nonpolar methane molecules restricting their penetration to the water phase. The hydrogen bond density near the surface in the water phase increases as per temperature drop or pressure upturn in an analogous manner to the temperature and pressure effects on the methane density profile at the interface. Therefore, the water mass fraction in the gas phase increases and methane solubility in liquid water at P>10 MPa and 25<T<105^{o}C remains poor.

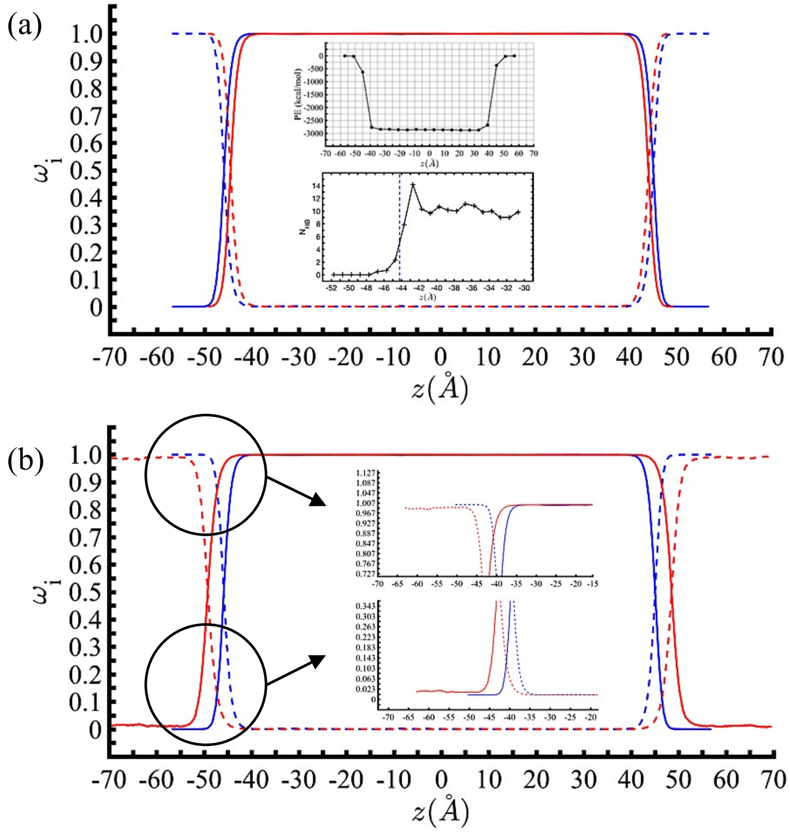

Figure 2.7. Water (solid line) and methane (dashed line) mass fractions. The pressure and temperature are subject to change in the plots (a) and (b), respectively. The system temperature for the plot (a) is 25°C. Blue and red lines denote the pressure of 10 and 50 MPa, respectively. Increasing the water mass fraction, consequently, decreasing the methane mass fraction in the liquid phase exhibits a dramatic decrease in the potential energy and increase in the hydrogen bond quantity at the interface as shown in the insets. Dashed line in the inset (a) represents the interface center obtained from the inflection point of fitted density profiles. Blue and red lines in the plot (b) denote the temperature of 25°C and 105°C at 10 MPa, respectively. The insets demonstrate how the mass fractions remain constant in the liquid phase but slightly change in the gas phase when the system experiences a temperature difference so that the water molecules might enter the gas phase more frequently at high-temperature regime.

2.7. Conclusions

In this work, we used molecular dynamics to characterize the interfacial mechanics, thermodynamics, and chemical composition of liquid water and methane gas interface. Given the chemical asymmetry and mechanical anisotropy of the methane-water interface we used a novel NP_NAT ensemble, that can keep constant normal pressure and constant cross-sectional area, both crucial to obtain reliable properties in interfacial studies. As result of this computational method, this work improved the accuracy of the predicted interfacial property data, showing less deviation from the experiments as well as generating a molecular-level characterization. Classical scaling laws were employed, such as the Eötvös rule in conjunction with fundamental thermodynamics to fully characterize the pressure and temperature dependence of the interfacial tension, interfacial thickness, and surface entropy, achieving good agreement with available experimental data. Results also concluded that the surface tension decreases as the pressure increases up to 50 MPa and more susceptibly, the temperature. Using the adaptive ensemble, we demonstrated that the interfacial thickness and longitudinal computational box length can elongate with either temperature increase or pressure decrease. Increasing both methane surface excess and local density near the surface suggests anomalous methane adsorption onto the water-methane surface. On the other hand, the strong hydrogen bonds adjacent to the surface in the water side favorably interact with the methane molecules and withhold them in the gas phase limiting the methane solubility, particularly at high pressure (P>10 MPa). Overall, the comprehensive results provide a quantitative characterization and molecular-level description of the water-methane interface which is of importance to fundamental surface physics and energy and environmental applications.

2.8. Acknowledgements

This work is made possible by the financial support of the McGill Engineering Doctoral Awards (MEDA) Grad Excellence Award program and the Natural Sciences and Engineering Research Council (NSERC) through the Discovery Grants Program. The authors are also thankful to Calcul Québec and Compute Canada for technical support and access to HPC facilities.

2.9. References

1. Busch, A. and A. Amann-Hildenbrand, *Predicting capillarity of mudrocks.* Marine and Petroleum Geology, 2013. **45**: p. 208-223.

2. Nourbakhsh, A., *Determination of capillary pressure, relative permeability and pores size distribution characteristics of coal from Sydney basin-Canada.* 2012.

3. Poling, B.E., J.M. Prausnitz, and J.P. O'connell, *The properties of gases and liquids*. Vol. 5. 2001: Mcgraw-Hill New York.

4. Sloan Jr, E.D. and C. Koh, *Clathrate hydrates of natural gases*. 2007: CRC press.

5. Sloan, E.D., *Fundamental principles and applications of natural gas hydrates.* Nature, 2003. **426**(6964): p. 353-363.

6. Harriss, R.C., et al., *Sources of atmospheric methane in the south Florida environment.* Global Biogeochemical Cycles, 1988. **2**(3): p. 231-243.

7. Kashchiev, D. and A. Firoozabadi, *Nucleation of gas hydrates.* Journal of Crystal Growth, 2002. **243**(3–4): p. 476-489.

8. Binks, B.P. and J.H. Clint, *Solid wettability from surface energy components: relevance to pickering emulsions.* Langmuir, 2002. **18**(4): p. 1270-1273.

9. Vázquez, U.O.M., et al., *Calculating the surface tension between a flat solid and a liquid: a theoretical and computer simulation study of three topologically different methods.* Journal of Mathematical Chemistry, 2009. **45**(1): p. 161-174.

10. Chaplin, M., *Theory vs experiment: what is the surface charge of water?* Water Journal Multidisciplinary Research Journal 1, 2009: p. 1-28.

11. Eisenberg, D., D.S. Eisenberg, and W. Kauzmann, *The structure and properties of water*. 2005: Oxford University Press on Demand.

12. Biscay, F., et al., *Monte Carlo simulations of the pressure dependence of the water−acid gas interfacial tensions.* The Journal of Physical Chemistry B, 2009. **113**(43): p. 14277-14290.

13. Biscay, F., et al., *Monte Carlo calculation of the methane-water interfacial tension at high pressures.* The Journal of Chemical Physics, 2009. **131**(12): p. 124707.

14. Ikeguchi, M., *Partial rigid-body dynamics in NPT, NPAT and NPγT ensembles for proteins and membranes.* Journal of Computational Chemistry, 2004. **25**(4): p. 529-541.

15. Kvamme, B., T. Kuznetsova, and K. Schmidt. *Experimental measurements and numerical modelling of interfacial tension in water-methane systems*. in *Presentation at the International Conference of Computational Methods in Sciences and Engineering, Chania, Greece*. 2006.
16. Schmidt, K.A., G.K. Folas, and B. Kvamme, *Calculation of the interfacial tension of the methane–water system with the linear gradient theory.* Fluid Phase Equilibria, 2007. **261**(1): p. 230-237.
17. Ghoufi, A. and P. Malfreyt, *Calculation of the surface tension and pressure components from a non-exponential perturbation method of the thermodynamic route.* The Journal of Chemical Physics, 2012. **136**(2): p. 024104.
18. Kirkwood, J.G. and F.P. Buff, *The statistical mechanical theory of surface tension.* The Journal of Chemical Physics, 1949. **17**(3): p. 338-343.
19. Tolman, R.C., *Consideration of the Gibbs theory of surface tension.* The Journal of Chemical Physics, 1948. **16**(8): p. 758-774.
20. Ghadar, Y. and A.E. Clark, *Intermolecular network analysis of the liquid and vapor interfaces of pentane and water: microsolvation does not trend with interfacial properties.* Physical Chemistry Chemical Physics, 2014. **16**(24): p. 12475-12487.
21. Horn, H.W., et al., *Development of an improved four-site water model for biomolecular simulations: TIP4P-Ew.* The Journal of Chemical Physics, 2004. **120**(20): p. 9665-9678.
22. Jorgensen, W.L., J.D. Madura, and C.J. Swenson, *Optimized intermolecular potential functions for liquid hydrocarbons.* Journal of the American Chemical Society, 1984. **106**(22): p. 6638-6646.
23. Plimpton, S., *Fast parallel algorithms for short-range molecular dynamics.* Journal of Computational Physics, 1995. **117**(1): p. 1-19.
24. Hockney, R.W. and J.W. Eastwood, *Computer simulation using particles*. 1988: crc Press.
25. Isele-Holder, R.E., W. Mitchell, and A.E. Ismail, *Development and application of a particle-particle particle-mesh Ewald method for dispersion interactions.* The Journal of Chemical Physics, 2012. **137**(17): p. 174107.
26. Rowlinson, J.S. and B. Widom, *Molecular theory of capillarity*. 2013: Courier Corporation.
27. Grest, G.S., et al., *Substructured multibody molecular dynamics*. 2006, Sandia National Laboratories.

28. Blokhuis, E., et al., *Tail corrections to the surface tension of a Lennard-Jones liquid-vapour interface.* Molecular Physics, 1995. **85**(3): p. 665-669.

29. Chapela, G.A., et al., *Computer simulation of a gas–liquid surface. Part 1.* Journal of the Chemical Society, Faraday Transactions 2: Molecular and Chemical Physics, 1977. **73**(7): p. 1133-1144.

30. Ibergay, C., et al., *Molecular simulations of the n-alkane liquid-vapor interface: Interfacial properties and their long range corrections.* Physical Review E, 2007. **75**(5): p. 051602.

31. Davis, H. and L. Scriven, *Stress and structure in fluid interfaces.* Advances in Chemical Physics, 1982. **49**: p. 357-454.

32. Winkelmann, J., *H. Ted Davis: Statistical mechanics of phases, interfaces, and thin films, VCH publishers, New York 1996, ISBN 1-56081-513-2, 712 Seiten, 267 Abb., Preis: DM 135, 00.* Berichte der Bunsengesellschaft für physikalische Chemie, 1997. **101**(3): p. 641-642.

33. Nicolas, J. and N. De Souza, *Molecular dynamics study of the n-hexane–water interface: towards a better understanding of the liquid–liquid interfacial broadening.* The Journal of Chemical Physics, 2004. **120**(5): p. 2464-2469.

34. Calvo, F., *Molecular dynamics determination of the surface tension of silver-gold liquid alloys and the Tolman length of nanoalloys.* The Journal of Chemical Physics, 2012. **136**(15): p. 154701.

35. Mendoza, F.N., et al., *Surface tension of hydrocarbon chains at the liquid–vapour interface.* Molecular Physics, 2008. **106**(8): p. 1055-1059.

36. Sakamaki, R., et al., *Thermodynamic properties of methane/water interface predicted by molecular dynamics simulations.* The Journal of Chemical Physics, 2011. **134**(14): p. 144702.

37. Sachs, W. and V. Meyn, *Pressure and temperature dependence of the surface tension in the system natural gas/water principles of investigation and the first precise experimental data for pure methane/water at 25°C up to 46.8 MPa.* Colloids and Surfaces A: Physicochemical and Engineering Aspects, 1995. **94**(2): p. 291-301.

38. Sun, C.-Y., G.-J. Chen, and L.-Y. Yang, *Interfacial tension of methane+water with surfactant near the hydrate formation conditions.* Journal of Chemical & Engineering Data, 2004. **49**(4): p. 1023-1025.

39. Alejandre, J., D.J. Tildesley, and G.A. Chapela, *Molecular dynamics simulation of the orthobaric densities and surface tension of water.* The Journal of Chemical Physics, 1995. **102**(11): p. 4574-4583.

40. Reed, S.K. and R.E. Westacott, *The interface between water and a hydrophobic gas.* Physical Chemistry Chemical Physics, 2008. **10**(31): p. 4614-4622.

41. Blas, F.J., et al., *Vapor-liquid interfacial properties of fully flexible Lennard-Jones chains.* The Journal of Chemical Physics, 2008. **129**(14): p. 144703.

42. Udeagbara, S.G., *Effect of Temperature and Impurities on Surface Tension of Crude Oil*. 2010: Universal-Publishers.

43. McCain, W.D., *The properties of petroleum fluids*. 1990: PennWell Books.

44. Jacobson, L.C., W. Hujo, and V. Molinero, *Thermodynamic stability and growth of guest-free clathrate hydrates: a low-density crystal phase of water.* The Journal of Physical Chemistry B, 2009. **113**(30): p. 10298-10307.

45. Naeiji, P., F. Varaminian, and M. Rahmati, *Comparison of the thermodynamic, structural and dynamical properties of methane/water and methane/water/hydrate systems using molecular dynamic simulations.* Journal of Natural Gas Science and Engineering, 2017. **44**: p. 122-130.

Chapter 3. Molecular Dynamics Characterization of the Water-Methane, Ethane, and Propane Gas Mixture Interfaces

Chapter 3: Molecular Dynamics Characterization of the Water-Methane, Ethane, and Propane Gas Mixture Interfaces

3.1. Preface

In this chapter**,** ethane and propane molecules are added to the gas phase in order to tailor more realistic natural gas-water mixture, present in the nature and energy-related industries. The interfacial tension as a function of pressure and temperature is calculated at the gas-water interface with the use of a sophisticated ensemble embedded in molecular dynamics technique. Moreover, a wide range study on the hydrogen bonding, composition, surface excess, and radial distribution function reveals some insights into the location of the gas hydrate formation. This chapter is reproduced with permission from “Mirzaeifard, S., P. Servio, and A.D. Rey, Molecular dynamics characterization of the water-methane, ethane, and propane gas mixture interfaces. Chemical Engineering Science, 2019. 208: 114769”.

3.2. Abstract

The co-existing natural gas and water bulk phases arise in a wide range of technological and environmental processes. The liquid-gas mixture is separated by an interface which plays a crucial role in mass transport across the phases. In this work, we use the molecular dynamics (MD) technique to investigate the molecular organization, solubility, density, and composition of natural gas-water interfaces. We apply the $NP_{N}AT$ ensemble which is an appropriate statistical methodology to dodge the defects of the conventional ensembles in surface physics, and ultimately, to characterize the interfacial thermodynamics and mechanics. High interfacial density, excess, and radial pair distribution function of the gas components in order of propane, ethane, and methane, respectively, suggest the interfacial adsorption as per favorable interactions with a dense hydrogen bonding network near the surface in the liquid water phase. It is also found that the gas components solubility is negligible. Nevertheless, methane molecules present in natural gas can further dissolve in water, comparing to pure methane. We lastly conclude a heterogeneous formation of structure II hydrate from the adsorption and composition results. Moreover, we systematically increase the pressure from 1 MPa to 50 MPa and the temperature from 273.15 K to 303.15 K to calculate the interfacial tension using the mechanical approach. We observe a decrease in the interfacial tension along with an increase in both pressure and temperature. Given the remarkable hydrocarbon adsorption acting as a surfactant, this interfacial tension attenuation is more highlighted in a natural gas-water system compared to the pure liquid-vapor water or water-pure methane systems at the same temperature and pressure. We employ MD combined with fundamental thermodynamics to predict the interfacial tension via its independent relations with pressure and temperature which agrees with the classical scaling laws, namely, the Eötvös rule. The corresponding molecular mechanisms captured by the microscopic and macroscopic properties at the interfacial region prospectively demonstrate a sensitivity to both temperature and pressure, which contributes to the developing understanding and applications of the imperative water-natural gas interface.

3.3. Keywords

water-natural gas mixture interface; gas hydrates; surface physics; interfacial tension; molecular dynamics simulation; NP_NAT ensemble.

3.4. Introduction

The coexistence of natural gas and water is found in the oil and gas industries [1, 2] and in biological systems [3]. It also plays a significant role in terms of environmental impact [4], and has a strong relevance to climate science [5]. In all these processes and phenomena, the methane, ethane, and propane mixture, as the main constituents of the natural gas, is directly in contact with liquid water [6] and hence interfacial thermodynamics and interfacial transport phenomena at the water-natural gas (W/NG) interfaces play an important role [7]. In particular the interfacial tension governs the capillary pressure involved in the fluid dynamics in petroleum pipelines and reservoirs, which is vital for many processes such as exploration and production [8, 9]. Despite its technological and fundamental physics importance, the molecular-level understanding and characterization of W/NG interfacial properties, interfacial composition and mechanics remains incomplete.

Under frequently found natural and industrial temperature and pressure conditions, the interactions of natural gas and water molecules may trigger the nucleation of clathrate hydrates. Clathrate or gas hydrates are ice-like crystalline solids which consist of the gas, guest molecules, encapsulated inside of the metastable host water cavities [10]. Depending on the guest gas molecules, the hydrates can form different crystalline structures known as structure I [11], structure II [12, 13], and structure H [14]. Clathrate hydrates are central to many industrial applications such as flow assurance, gas storage, climate change, alternative energy resources, and transportation [15]. For instance, clathrate hydrates reserves are estimated to be able to provide up to three orders of magnitude more energy than the diminishing fossil energy reserves [1, 10], which promotes our incentives. The main motivation of this work is to characterize the interfacial energy contribution in the nucleation process of gas hydrates by performing a molecular-level study of the natural gas-liquid water interface.

3.4.1. Motivation

We briefly elaborate on the motivation of this work. According to the classical nucleation theory (CNT), the hydrate formation can be categorized as either homogeneous or heterogeneous but the process remains incompletely understood [16, 17]. Elucidating the basic theory behind the clathrate formation is important in order to discover efficient methods of promoting or inhibiting their formation, depending on the above-mentioned applications. Among all the theories in crystallography, the classical nucleation theory is still the basis of the most modern nucleation studies, which can successfully describe the work of clathrate formation, namely, ice and gas hydrate [10, 18-20]. After necessary assumptions, this work is divided into two contributions including spontaneous formation of a new phase and the interfacial energy cost [21]:

$$W(J) = -n\Delta\mu + c(nv_h)^{\frac{2}{3}}\sigma \tag{3.1}$$

where n, $\Delta\mu(J)$, c, v_h (m^3), and σ ($\mathrm{J/m}^2$) denote the number of crystal unit cells, supersaturation, shape factor, hydrate volume, and surface energy, respectively. Hence, to make progress with the understanding of this formation work, we need to calculate the interfacial energy between all the involved phases including liquid-gas, hydrate-gas, and liquid-hydrate. Figure 3.1a shows schematic examples of hydrate formation. Many factors such as different hydrate phase morphologies [22] and fluid flow in natural or industrial environments might affect the formation [23-25]. The interfacial boundaries between different existing phases dictate the ideal location and process for the hydrate nucleation [26]. Thus, an extensive characterization of the interfacial energy between the natural gas and liquid water phases is vitally important to hydrate science.

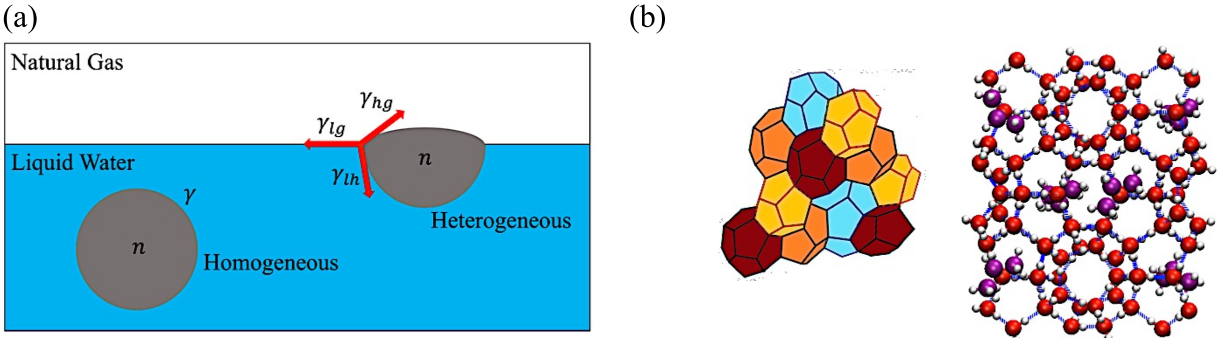

Figure 3.1. (a) Introducing different clathrate formation processes. γ is the interfacial tension of the homogeneous formation of gas hydrates. γ_{lg}, γ_{hg}, and γ_{lh} denote the interfacial tension between the liquid-gas phases, the hydrate-gas phases, and the liquid-hydrate phases, respectively. In this work, we study γ_{lg} where the liquid is water. (b) Geometric configuration of structure II hydrates alongside a snapshot of propane hydrate. The purple, red, and white particles denote the propane molecules, the oxygen atoms, and the hydrogen atoms, respectively. The blue dashed lines represent the hydrogen bonding network.

In this study, we assume the surface energy is the same as the surface tension in large scale formation [27]. Therefore, to capture the interfacial energy between different phases including natural gas-liquid water, one needs a sound knowledge of the tensorial stress governing the interface mechanics. The interfacial tension between the liquid and hydrate phases to reach the total interfacial energy contribution can also be obtained using the Young equation [28], which is not within the scope of this work.

The understanding of the nature of interfacial interactions is of great importance to elucidate the thermodynamic stability, phase transitions, morphology, nucleation, and the growth rate of clathrate hydrates, which requires novel experimental techniques, theoretical modeling, or computational characterization. The molecular structure and organization at the surface predominantly influence the bulk and interfacial properties of the water-natural gas systems. Hayama *et al.* propound to investigate the effects of different alkanes on the molecular mechanism at the interface, which cannot be explained in their experiments [29]. Furthermore, Speight *et al.* state that surface tension increases with molecular weight [30] while this relation is unclear in the mixtures. Moreover, Wang *et al.* observes that mixing the gas components changes their solubility in liquid water/alcohols, which tremendously affects the mechanism of the hydrate inhibitors, but the reason is poorly understood [31]. To the best of our knowledge, this is the first work that attempts to simulate the water-natural gas mixture in order to answer all these crucial questions. Furthermore, based on the W/NG interface characterization, we deduce features of the heterogeneous nucleation of structure II hydrates, whereas the ubiquitous methane molecules in ocean sediments insinuate that structure I hydrates would probabilistically form [15, 32, 33]. Figure 3.1b shows a configuration sample of structure II hydrates.

Experimental characterization of the W/NG interface at conditions relevant to gas hydrate nucleation is challenging due to the high pressure for hydrate formation, need of molecular-level measurements, and sample impurities leading to inaccurate results [34, 35]. Hence, we seek insights into the microscopic interfacial regions using computer simulations, which can effectively provide all the essential information. Nonetheless, molecular simulations encounter challenges of its own at water-hydrophobic gas interfaces, explicitly, sudden local density variation, robust hydrogen bonding, ion binding, topological disturbance, discontinuity of macroscopic fields, spontaneous interfacial contraction, and sufficient time and length scales for reliable results. These issues can be appropriately overcome by applying the methods to mimic realistic models and leverage the study of the distinct thermodynamic and mechanical behaviors at the bulk and interfaces [36, 37]. In this work, we employ very powerful molecular dynamic (MD) techniques in conjunction with sophisticated interfacial thermodynamics to investigate molecular organization, weights, structure, and solubility of large alkanes. In addition, we readily calculate the crucial interfacial tension from pressure tensor analysis, and subsequently, derive classical scaling laws to characterize the complex natural gas-water interface as a function of pressure and temperature. The key aspect of our approach is to observe the molecular structures of a pure mixture with no external disturbances to further uncover the theoretical physics behind the phase co-existence at both microscopic and macroscopic levels.

3.4.2. Computational Challenges

We briefly comment the computational challenges in capturing the physics and thermodynamics of the W/NG interface. Some thermodynamic and physical parameters including the local density and potential energy express non-uniform behavior along the normal direction to the liquid-gas interface. We tackle this problem in surface science with the selection of a proper statistical ensemble to provide sensible results. In general, the appearance of multiple phases consisting of anisotropic interfaces constrains the choice of ensemble. The thermodynamics and mechanics of the system differ in the normal and lateral directions at the interface. Consequently, the standard *NPT* ensemble cannot guarantee reliable interfacial properties. This ensemble requires adjusting a uniform pressure, whereas, the stress tensor loses its constancy along the simulation box so that the tangential pressure suddenly drops at the interfaces. On the other hand, the conventional *NVT* ensemble could be an alternative to automatically calibrate the pressure resolving the above-mentioned concerns. Nevertheless, this ensemble might fail because of the lack of information over the system volume. Therefore, we need to use a unique ensemble in surface studies, which is independent of complete knowledge over the system volume or the tangential pressure at the interface, and simultaneously, controlling the temperature and pressure across the mixture to avoid the disturbances in the interfacial regions. Herein, we propose to employ the NP_NAT ensemble, which only sets the constant cross-sectional area (A) and normal pressure (P_N) imposed onto the planar surface. This sophisticated ensemble has been previously used to predict the most sensible values of liquid-gas systems [38, 39], anisotropic liquid-solid interfaces [40] and polar lipid bilayers in cell membrane [41].

In modern computational physics, there are two thermodynamic and mechanical approaches to calculate the interfacial tension of mixtures [42-44]. In the thermodynamic approach, one might derive the surface tension from the change in interfacial free energy over the associated area. This definition mainly targets the global properties [45], while we intend to pursue both global and local perspectives of the system. In addition, the interfacial area must remain static in the NP_NAT ensemble throughout the simulations leaving the mechanical approach as a pragmatic option for us to effectively estimate the interfacial tension of a system with a density gradient in only one dimension. Therefore, we need to obtain the local components of the pressure tensor at the natural gas-water interface obeying the Kirkwood and Buff technique [44].

The organization of this paper is as follows. In the next section, we concisely describe the models and MD simulation including the novel method for the calculation of the liquid-gas interfacial tension. In the results and discussion section, we analyze the density, adsorption, solubility, and molecular organization at the interface. In addition, the temperature and pressure effects on the interfacial tension, structure, thickness, and entropy are discussed. Finally, we present the main conclusions of this work, and the novelty and significance of the results for current and future studies.

3.5. Model and Simulation Methods

We employ the molecular dynamics technique to investigate the classical thermodynamic behavior of the water-natural gas mixture at its interface as a function of pressure and temperature. We follow the common computational method in surface science and confine the liquid water phase between two gas phases as shown in Figure 3.2a [44, 46]. Then we apply periodic boundary conditions for the simulation box with the initial size of 36×36×200 Å in three dimensions. The NP_NAT ensemble requires the fixed box lengths in the x and y dimensions to provide a constant cross-sectional area (i.e., $A = L_x L_y$). The initial value of the box length in the z dimension (L_z) is arbitrary as we allow the box to independently dilate or contract in that direction [47]. This procedure regulates the system volume so we can attain the desired target pressure, and consequently, the prescribed bulk density for coexisting liquid and gas phases towards equilibration. We design the simulation box with two distinct molecular configurations. In the first scenario, we randomly place 600 molecules for each individual gas component in a slab in the middle of the simulation box and surround this slab with 3825 water molecules on both sides. Hereby, we seek to better understand the effect of molecular weight and structure of the different hydrocarbons in an identical situation. Next, we form another configuration with a realistic gas composition to tailor the natural gas for the second scenario. We confine 3825 water molecules between two regions of the gas molecules, which altogether consist of 600 methane molecules, 45 ethane molecules, and 17 propane molecules following the natural gas composition from experiments [16]. Figure 3.2b depicts one snapshot of a typical initial configuration of this case. Fortunately, we can study the water-natural gas interfacial properties and the timely access to experimental data [29] allows us to validate the methods and predictions.

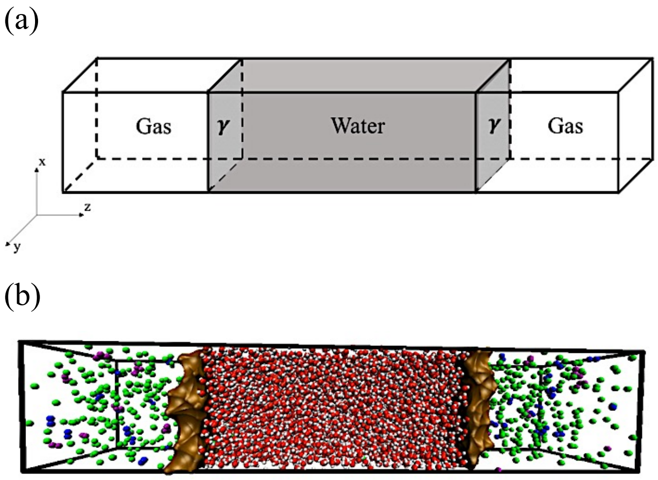

Figure 3.2. (a) Schematic showing the water and gas molecules in grey and white zones to represent the liquid and gas phases, respectively. (b) Snapshot of the initial configuration of the system. The green, blue, purple, red, and white particles denote the methane molecules, the ethane molecules, the propane molecules, the oxygen atoms, and the hydrogen atoms, respectively. The brown regions define the interfaces separating the gas and liquid phases.

In the present work, we employ the transferable intermolecular potential with the four points (TIP4P) model [48] and united atom optimized potentials for liquid simulations (OPLS-UA) model [49] to simulate the force fields for water and gas molecules, respectively, within the LAMMPS simulation package [50]. To calculate the Coulombic electrostatic interactions, we apply the particle-particle particle-mesh (PPPM) technique, optimized for the TIP4P model, introduced by Hockney and Eastwood [51, 52] with an accuracy of 10^{-5} for the errors in force computation. Moreover, we utilize the Lennard-Jones (LJ) potential with Lorentz-Berthelot approach as an arithmetic mixing rule for the unlike particles to represent the intermolecular interactions:

$$U_{LJ}(r) = 4\varepsilon\left[\left(\frac{\sigma}{r}\right)^{12} - \left(\frac{\sigma}{r}\right)^{6}\right] \tag{3.2}$$

$$\varepsilon_{ij} = \sqrt{\varepsilon_{ii}\varepsilon_{jj}} \tag{3.3}$$

$$\sigma_{ij} = \frac{\sigma_{ii}+\sigma_{jj}}{2} \tag{3.4}$$

where ε, σ, and r denote the potential well depth, the finite distance at zero potential, and the distance between the particles, respectively. We choose the cut-off distance of 12 Å for LJ and short range electrostatic interactions. Table 3.1 expresses the required simulation data, including the partial electron charges, the distance and the angles between atoms or charge sites, and LJ potential parameters [48, 49]. An additional force is applied through the Shake algorithm to constrain the bonds and the angles associated with the bonded molecules including the water, the ethane, and the propane. Using such force can guarantee all bond lengths and angles remain constant throughout the simulations.

Table 3.1. Molecular weights, distance and angles between atoms or charge sites, partial electron charges, and Lennard-Johns potential well depth (ε) and finite distance (σ) determine the simulation parameters.

	mass (g/mol)	σ (Å)	ε (kcal/mol)	charge (e)
O	15.999	3.164	0.163	-1.0484
H	1.0080	0	0	0.5242
CH_4	16.042	3.733	0.294	0
CH_3 (ethane)	15.035	3.775	0.207	0
CH_3 (propane)	15.035	3.905	0.175	0
CH_2 (propane)	14.027	3.905	0.118	0
O-H bond length		0.9572 Å		
H-O-H angle		104.52°		
O⋯M distance		0.125 Å		
C-C bond length		1.526 Å		
C-C-C angle		112.4°		

The Verlet algorithm is used to integrate the non-Hamiltonian equations of motion within each time step of 2 fs. In addition, we retain the scaling of the particles velocity to control the temperature, and subsequently, to sample the system configuration using the desired ensemble. Nosé-Hoover thermostat and Parrinello-Rahman barostat couple the dynamic variables to the motion equations to regulate the temperature and the pressure with the damping constant of 4 ps for the inherent fluctuations. The simulations are carried out for 10 ns, which is sufficiently long to ascertain the thermodynamic equilibrium state. To support the practical equilibration time of 3-4 ns, we observe no major variation in the mechanical and thermodynamic properties of the system such as the pressure and the temperature, and simultaneously, the correlation factor for the potential energy rapidly vanishes. Nonetheless, we analyze the simulation outcome collected from the last 1 ns to guarantee acceptable accuracy.

The following equation is used to calculate the interfacial tension from the Kirkwood and Buff method (γ_{KB}):

$$\gamma_{KB} = \int_{-\infty}^{+\infty} \left(P_N - P_T(z)\right) dz \tag{3.5}$$

where P_N and P_T indicate the normal and tangential pressures, respectively. This integral is calculated over the entire simulation box in the z direction. We then compute P_N and P_T from the stress tensor [53]:

$$P_N = P_{zz} = P \tag{3.6}$$

$$P_T = \frac{1}{2}\left(P_{xx} + P_{yy}\right) \tag{3.7}$$

Ignoring the slight computational fluctuations, these normal and tangential pressures are constantly identical to the total pressure along the simulation box excluding the interfacial regions. While, the tangential pressure considerably drops at the interface producing a positive value for the difference between the normal and tangential pressures. Additionally, we use the mean values for the stress tensor components to calculate the surface tension, in an analogous manner to our previous work [54]. Please note that the integral (Eqn. 3.5) is divided by two, given the existence of two evolved interfaces between water and gas molecules along the simulation box. Hence, the surface tension can be obtained from:

$$\gamma_{KB} = \frac{Lz}{2}\left[\langle P_z \rangle - \frac{1}{2}\left(\langle P_{xx} \rangle + \langle P_{yy} \rangle\right)\right] \tag{3.8}$$

However, the truncations in the computation process of the interatomic interactions causes the interfacial energy obtained from the mechanical definition (Eqn. 3.8) to be underestimated [55, 56]. The cut-off distance in the interatomic interactions weakens the interfacial tension along with the bulk pressure at a constant density. In the inhomogeneous systems such as the mixture in this study where all the phases are engaged with all the components, the drop in the interfacial tension calculation is much highlighted [57]. To compensate for the surface tension inaccuracy in multicomponent systems, we require a tail (long-range) correction given by Blokhuis *et al.* [55]:

$$\gamma_{tail} = \int_0^1 \int_{r_c}^{\infty} 12\pi\varepsilon\sigma^6 \left(\rho_l - \rho_g\right)^2 \left(\frac{3s^3 - s}{r^3}\right) cot\left(\frac{rs}{d}\right) dsdr \qquad (3.9)$$

where r_c, d, s, and ρ_l and ρ_g represent the cut-off distance, interfacial thickness, position, and molecular densities of the liquid and gas phases, respectively. Accordingly, we obtain the interfacial tension (γ) from the following equation throughout the simulations:

$$\gamma = \frac{L_Z}{2}\left[\langle P_Z\rangle - \frac{1}{2}\left(\langle P_{xx}\rangle + \langle P_{yy}\rangle\right)\right] + \int_0^1 \int_{r_c}^{\infty} 12\pi\varepsilon\sigma^6 \left(\rho_l - \rho_g\right)^2 \left(\frac{3s^3 - s}{r^3}\right) cot\left(\frac{rs}{d}\right) dsdr \qquad (3.10)$$

3.6. Results and Discussion

The mass density and component concentration are the initial quantities of interest. We need to obtain a firm knowledge of the interfacial mass density profile which can later contribute in the tail correction of the interfacial tension calculation. In addition to the bulk density, we obtain the local mass densities of all the components (i.e., water, methane, ethane, and propane molecules) to discern the molecular distribution along the simulation box.

To elucidate the effects of the different hydrocarbons, we follow the scenario one in the method section and build a system with an equal mole fraction for each of the components in the natural gas at 298.15 K and 10 MPa. Figure 3.3 exhibits a peak in the density profile in the gas side near the interface owing to the compressive forces between the gas components. An accumulation of gas molecules onto the water surface might explain the existence of this peak. This anomalous adsorption points to the heterogeneous mode of hydrate nucleation, which occurs at the interface of natural gas and liquid water. Such phenomenon for solitary methane molecules in contact with water has been previously reported [54, 58]. Herein, Figure 3.3a depicts that the presence of the ethane molecules might change the composition of the natural gas at the interface so that the ethane molecules have priority to the methane molecules in terms of the interfacial adsorption. Likewise, Figure 3.3b shows that the insertion of the propane molecules with identical quantity into the gas mixture leads to the enrichment of the propane molecules followed by the ethane molecules with a negligible methane enrichment.

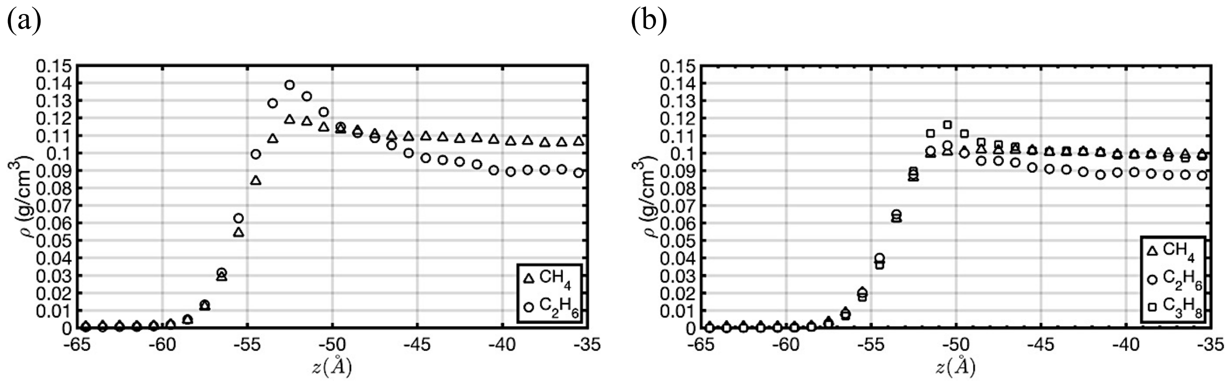

Figure 3.3. Local density profiles (g/cm3) of the water-gas mixture with (a) and without (b) the propane molecules near the interface at 298.15 K and 10 MPa. The triangle, circle, and square markers denote the methane, ethane, and the propane concentrations, respectively. When the system contains large hydrocarbons, the gas adsorption onto the water surface sequentially occurs from large to small molecules. Please note that the interface center is -50 Å, which is obtained from the inflection point of fitted density profiles.

To quantify this segregation effect, we calculate the component adsorption Γ_i from the surface excess of each of the gas components:

$$\Gamma_i(\text{mol}/m^2) = \frac{1}{A}\int_{-\infty}^{\infty}\left\{\rho_i(z) - \rho_{i,l}\Theta(-z) - \rho_{i,g}\Theta(z)\right\}dz \tag{3.11}$$

where ρ_i, $\rho_{i,l}$, $\rho_{i,g}$, and $\Theta(z)$ denote the component i density profile (g/cm^3), bulk density (g/cm^3) in liquid and gas phases, and Heaviside step function, respectively. Table 3.2 reports the surface excess of the gas components in the systems with and without the propane molecules. We expectedly observe that the maximum surface excess is associated with the largest saturated hydrocarbons.

Table 3.2. Interfacial excess of the water-gas mixture with and without the propane molecules at 298.15 K and 10 MPa.

	$\Gamma_{CH_4}(10^{-6}\ \text{mol}/m^2)$	$\Gamma_{C_2H_6}(10^{-6}\ \text{mol}/m^2)$	$\Gamma_{C_3H_8}(10^{-6}\ \text{mol}/m^2)$
CH_4+C_2H_6	2.50	3.93	-
CH_4+C_2H_{6+}+C_3H_8	2.39	2.74	2.80

To evaluate the molecular distribution in the system, we now characterize the chemical composition across the left interface. Since we encompass the gas in the central region between the water molecules, the mass fraction of the gas components prevails over the liquid water as we move from the box sides towards the center. Figure 3.4 depicts the concentration profiles for the water and gas molecules along the box length in the z direction. Negligible mass fraction for the gas components in the water phase is observed. We hypothesize that the presence of a firm hydrogen bonding (HB) network among the polar water molecules near the interface restricts the mobility of nonpolar gas molecules between the phases. Nevertheless, the gas components in order of their size may escape through this hydrogen bonding network, and slightly, penetrate the water phase. This penetration is more vivid for the methane molecules as the smallest hydrocarbon in the natural gas composition. The adsorption of the ethane and propane molecules also obliges few more methane molecules to be released into the water phase. The same results for the gas components solubility have been previously observed in the experiments [31, 59]. To confirm this hypothesis, we will consider a more realistic model later in this document to analyze the interaction between the hydrogen bonding and gas molecules. In general, these obtained gas concentration results in combination with the graded adsorption from high to low hydrocarbons are the first computational predictions, which elucidates why the natural gas at the favorable thermodynamic conditions heterogeneously forms the structure type II hydrates under the classical nucleation theory classification.

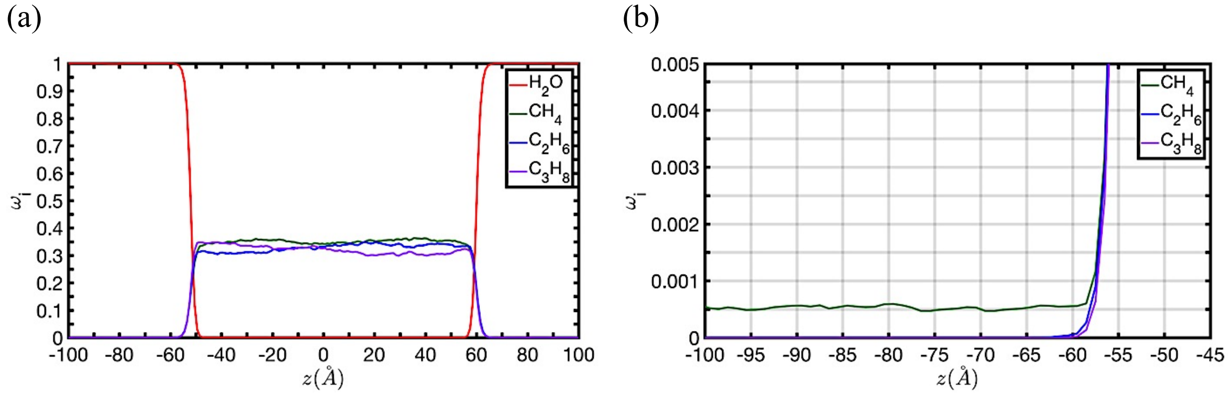

Figure 3.4. The plot (a) shows the mass fractions of water (red), methane (green), ethane (blue), and propane (purple) molecules at 298.15 K and 10 MPa. The plot (b) enlarges the mass fractions of the gas molecules in the liquid phase to illustrate the minor solubility of the methane molecules and the infinitesimal penetrations of the ethane and propane molecules inside the liquid water phase. Please note that the centers of the left and right interfaces are -50 Å and 62 Å, respectively, which are obtained from the inflection points of fitted density profiles.

We now use the other example with the mass fractions close to natural gas composition to examine the graded adsorption scenario in more realistic model. In this model, the water molecules are encapsulated between the gas molecules. Figure 3.5 exhibits a considerable loss in the potential energy at the interface as we move from the side gas phases to the central liquid phase in the z direction. This loss coincides with a major upturn in the water local density.

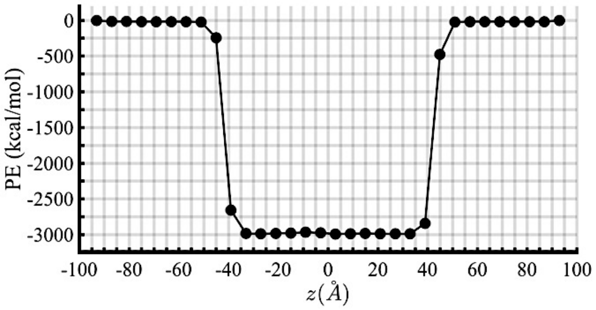

Figure 3.5. Potential energy (kcal/mol) of a system at 298.15 K and 10 MPa. As the mass fraction of the gas molecules decreases, consequently, the water mass fraction increases so that the system reveals a dramatic decrease in its local potential energy.

We calculate the radial pair distribution function of the gas components and water molecules at the interface to assess the effects of large hydrocarbon on the interfacial adsorption. Figure 3.6 clearly validates the previous conclusion that the water surface is covered with ordinal layers of propane, ethane, and methane molecules. The distribution functions show an initial spike at the same distance for the different components expressing the first layer of adsorption populated with more propane molecules. However, this spike is more pronounced for the methane and ethane molecules followed by a smooth increase in their distribution functions. The propane molecules show more fluctuations owing to their longer molecular length. It is worth mentioning that the propane molecules tend to lay in parallel, as opposed to perpendicular, on the water surface as the radial pair distribution functions for the CH_2 and CH_3 groups in the propane molecules are nearly the same, analogous to the purple lines shown in Figure 3.6. The results for the CH_2 and CH_3 groups are not individually shown in the figure since the differences with the propane distribution function is extremely infinitesimal. Although the methane, ethane, and propane have different molecular lengths, the adsorption trend is equivalent, which emphasizes on a parallel molecular orientation for the ethane and propane molecules.

This interfacial adsorption trend concluded from the density profile, the surface excess, and the radial pair distribution function calculations suggests the hydrate formation of structure sII, which involves the large saturated hydrocarbons. Moreover, the system at a lower temperature, which is thermodynamically more favorable for hydrate nucleation, shows an additional adsorption of the gas molecules facilitating the heterogeneous hydrate nucleation (see Figure 3.6 (b)).

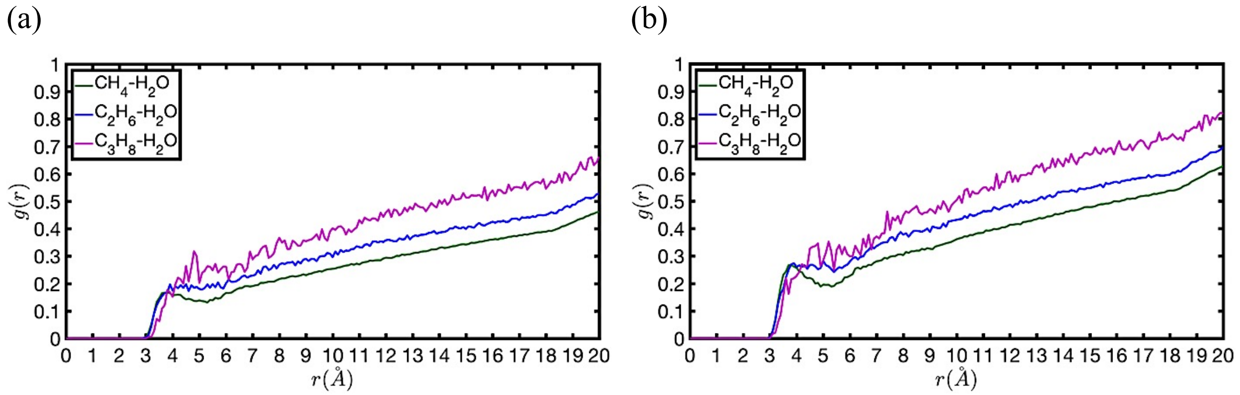

Figure 3.6. Radial pair distribution functions of the system at (a) 298.15 K and (b) 275.15 K, and 10 MPa. The plots present the multilayer adsorption of gas molecules onto the water surface. The adsorption enhances once the system experiences lower temperature as shown in the plot (b).

Herein, we compute the number of hydrogen bonds between the water molecules near the interface in a system at 298.15 K. We define the hydrogen bonding criterion by $O - O$ distance and $O \cdots O - H$ angle less than 3.5 Å and 30°, respectively, and average the computed number across 1000 configurations at equilibrium. Subsequently, we remove the ethane and the propane molecules from the systems to investigate the effect of the gas components coexistence. Furthermore, we reduce the temperature to 275.15 K, which thermodynamically provides the more favorable condition for the hydrate formation, to explore how the number of hydrogen bonds is pertinent to the system temperature. Figure 3.7a implies that the water molecules tend to form a denser hydrogen bonding network near the interface separating the surface water from the bulk water with distinct molecular-level organizations. Therefore, we speculate that the interfacial gas adsorption is attributed to more favorable interfacial interaction between the hydrogen bonds and the gas components in the water and the gas phases, respectively. Since the number of hydrogen bonds in a simple mixture of water and methane molecules appears to be lower than the natural gas-water system, we postulate that the number of hydrogen bonds increases with the natural gas molecular weight. On the other hand, the linear structure of ethane and propane molecules can better influence the hydrogen bonding network compared to the spherical methane molecules.

Moreover, Figure 3.7b evidently demonstrates that the hydrogen bond density near the surface increases as the temperature decreases, which leads to more adsorption of the larger hydrocarbons on the interface allowing the heterogeneous nucleation of the structure II hydrates. Additionally, this hydrogen bond-gas interaction predominantly triggers the compressive forces on the gas components yielding poor solubility of natural gas in liquid water at T<303K and 10 MPa, which agrees with the earlier results obtained from the concentration profiles.

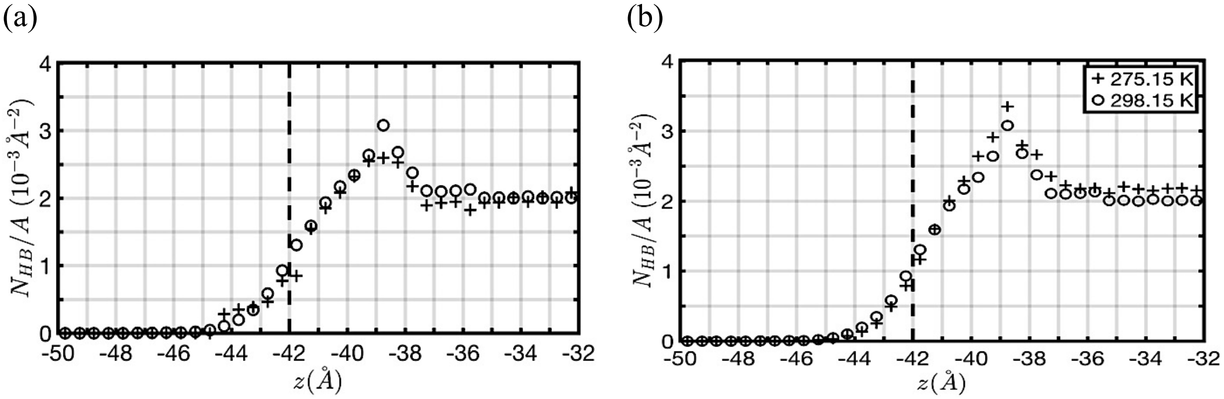

Figure 3.7. The plot (a) depicts the hydrogen bond quantity at the interface. The plus sign and circle markers represent the water-methane mixture and the water-natural gas mixture, respectively. Dashed line defines the interface center obtained from the inflection point of fitted density profiles. The plot shows that the presence of large hydrocarbons consolidates the interfacial hydrogen bonding. The temperature of the system is subject to change in the plot (b) to show the hydrogen bonding network near the interface is intensified in lower temperature regimes. The plus sign and circle markers denote the temperature of 275.15 K and 298.15 K, respectively.

We can now calculate the interfacial tension between the liquid water and the natural gas phases using Eqn. 3.10 to compare the results with the experiments and authenticate our method. In addition, we anticipate this calculation will support the findings of hydrate formation in different thermodynamic pressure and temperature regimes.

To calculate the interfacial tension, we increase the system pressure from 1 MPa to 10 MPa at the same temperature and gas composition following the experiments [29]. The deficient interactions between the interfacial molecules in the normal direction as compared to the bulk penalize the interfacial energy so that the pressure decrease causes the increase of this deficiency owing to less neighbors surrounding the molecules at the surface. The molecular interactions between the dense film of natural gas and water can compensate for the cohesive forces lowering the internal pressure, which leads to lower interfacial energy by the Gibbs equation compared to the pure water liquid-vapor system. Interfacial tension diminution is more highlighted for the natural gas-water system so that it exhibits 17.17-27.26% reduction at P>10 MPa compared to the water-pure methane mixture [54]. Figure 3.8 lucidly shows that the computational results are in excellent agreement with the experiments at the different thermodynamic conditions with average absolute deviations (AAD) of 0.19% to 3.35% obtained from [29]:

$$AAD = \frac{1}{N}\sum_{i=1}^{N}\left|\gamma_i - \langle\gamma_{ref}\rangle\right| \times 100 \tag{3.12}$$

where $\langle\gamma_{ref}\rangle$ and N represent the mean value and the number of references, respectively. The obtained AAD clearly shows the accuracy of using NP_NAT ensemble in MD for a system which involves the interfacial asymmetry. The largest deviation from the experiment is attributed to the system at 1 MPa since MD is slightly instable in low pressure regime (<5 MPa) owing to more pressure fluctuations, particularly in liquid and solid phases. The ADD vanishes as we increase the applied pressure in MD simulations providing more sensible results.

Herein, we systematically increase the system pressure from 1 MPa to 50 MPa at 298.15 K and calculate the interfacial tension to fit the obtained results with a master curve, and subsequently, find a relationship between the interfacial tension and the pressure as given below (units reported in the figure):

$$\gamma = 0.7862\,P - 10.88\sqrt{P} + 79.05 \tag{3.13}$$

(a)

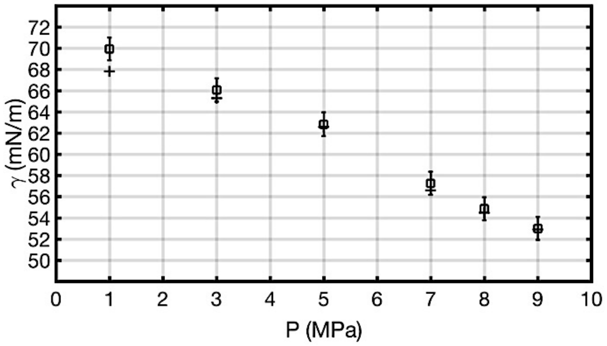

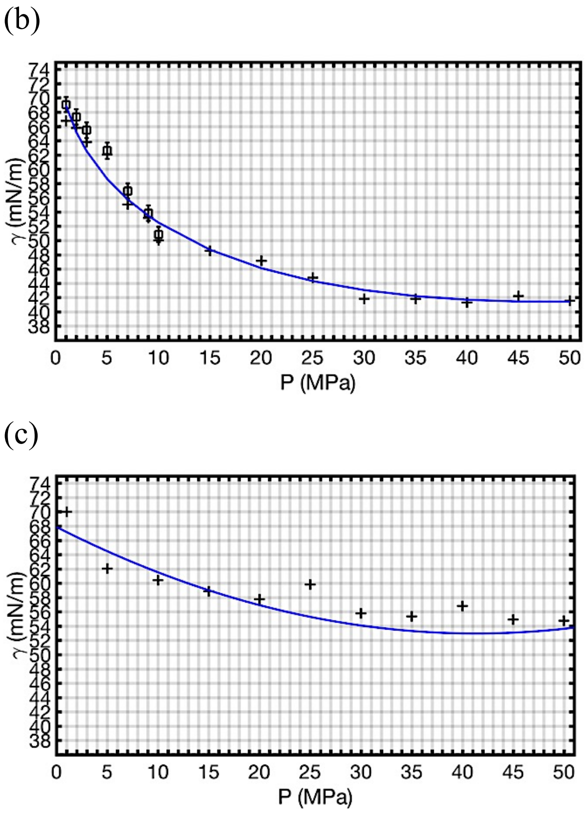

Figure 3.8. Interfacial tension (mN/m) of the water-natural gas mixture with increasing the system pressure (MPa) at the temperature of 293.15 K (a) and 298.15 K (b). The plot (c) shows the interfacial tension of the water-pure methane mixture at 298.15 K [54]. The square and plus sign markers represent the data obtained from the experiments by Hayama *et al.* and present work (with blue fitting curve), respectively [29]. The plots explicitly demonstrate that the interfacial tension decreases when the system is exposed to a pressure upturn, especially in the systems in the lower pressure regime (< 10 MPa).

In comparison with the water-pure methane system, the water-natural gas interfacial tension more rapidly decreases with pressure increase while both systems theoretically have the same interfacial tension of 66.9 mN/m at 298.15 K and 1.66 MPa [54]. Please note that the decrease of the interfacial tension disappears at P>30 MPa, consequently, the interface exhibits a constant tension with pressure upturn up to 50 MPa. This plateau section can be explained by the classic repulsive interactions between the water and nonpolar hydrophobic gas molecules. After the interface is saturated with the natural gas molecules, increasing pressure can no longer change the interfacial thickness, subsequently, the volume and the difference between bulk and interfacial density, which leads to revoking the effect of pressure on the interfacial tension and thickness. Figure 3.9a depicts the physical interfacial thickness $d(\text{Å})$ from the density profiles fitted by the hyperbolic tangent functions:

$$\rho(z) = \frac{1}{2}\rho_b\left(1 - \tanh\frac{|z-z_c|-z_G}{d}\right) \tag{3.14}$$

where ρ_b, z_c, and z_G denote the bulk density (g/cm^3), the center of interface (Å), and the Gibbs dividing surface position (Å), respectively.

In addition to the interfacial thickness, we report the box length in the z dimension (L_z) to evaluate the temperature and the pressure effects on the system. Figure 3.9 shows that d (a) and L_z (b) significantly contract or expand to adapt to the new thermodynamic conditions. In summary, the system can reveal large expansion in both d and, more susceptibly, L_z along with temperature rise or pressure drop. Please note that the pressure effect can persist so long as the system continues to hold its conditions which are pertinent to the material compressibility.

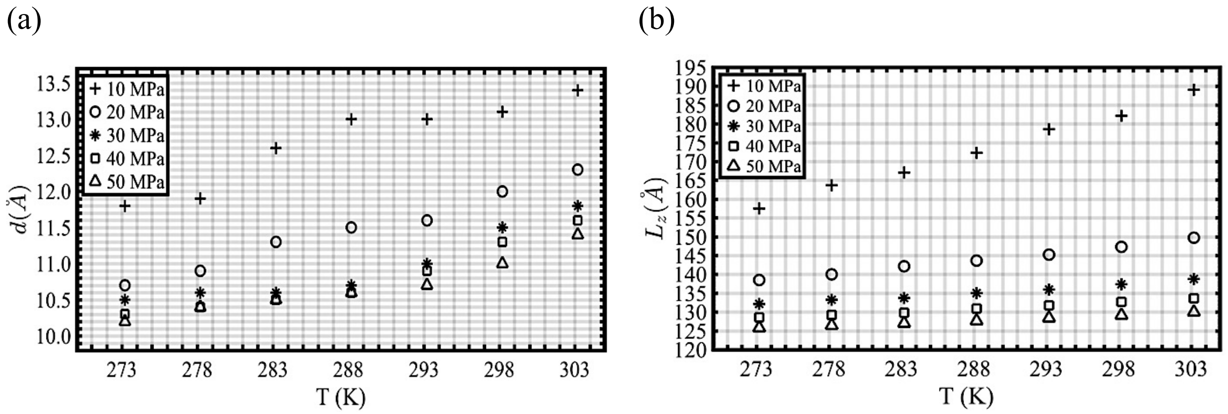

Figure 3.9. The temperature upturn triggers an increase in the physical interfacial thickness *d* (a) and L_z (b) at 10, 20, 30, 40, and 50 MPa represented by plus sign, circle, star, square, and triangle markers, respectively. High temperature regime further manifests the elongation of the box length.

Subsequently, we systematically increase the system temperature in a range of thermodynamically favorable conditions for the hydrate formation and calculate the interfacial tension between the water and gas phases. Figure 3.10 shows that the interfacial tension substantially depends on the temperature so that the interfacial tension decreases with increasing temperature, ultimately, the tension vanishes at the critical point. The tension diminution is attributed to the declining cohesive forces acting between the water molecules. In the system with a constant cross-sectional area at 10 MPa, one might fit the interfacial tension values with a quadratic curve in an analogous manner to the interfacial tension-pressure relation (units reported in the figure):

$$\gamma = -0.0001\, T^2 - 0.18\, T + 110 \tag{3.15}$$

Since the second order term is almost negligible, a good linear estimate to the surface tension as shown in Figure 3.10b is:

$$\gamma = -0.24\, T + 122.36 \tag{3.16}$$

Given the considerable adsorbed hydrocarbons acting as surfactants, the interfacial tension is expectedly lower than the surface tension between the pure liquid water in contact with its vapor. Likewise, the natural gas that contains larger hydrocarbons than methane further reduces the tension forasmuch as the fitting line exhibits 4.3% steeper slope in comparison with the mixture of water and pure methane [54].

Moreover, this master curve can correlate the interfacial tension and the temperature with the use of classical scaling laws. The Eötvös rule improved by Ramsay and Shields can perfectly conform by the following formula [60]:

$$\gamma V^{2/3} = k(T_c - T - 6) \tag{3.17}$$

where V, T_c, and k denote the molar volume, critical temperature of the mixture, and Eötvös constant of 2.1×10^{-7} J/K.mol$^{2/3}$, respectively. Hence, we find that the water-gas mixture with the molar volume of 28.86 cm^3 and the critical temperature of 536.31 K corresponds to the linear fitting line. Interestingly, we can attain very similar molar volume and critical temperature with only 1.9% deviation from the mixing rules providing the system is considered ideal, which again shows the agreement of the simulations with theory [61]. Nevertheless, this linear function may only predict the interfacial tension in the specific range of temperature and pressure since we do not examine the other factors such as molecular orientation, polarity, and structure under different thermodynamic conditions.

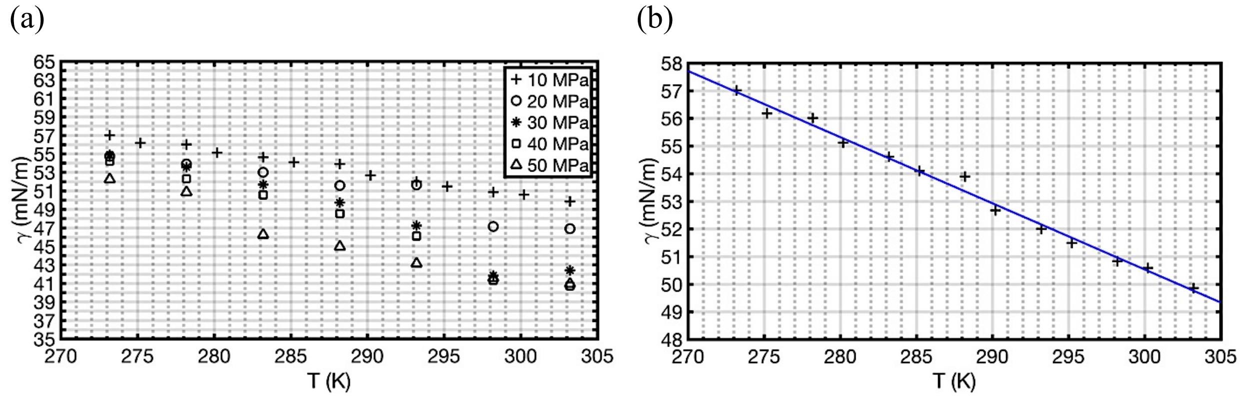

Figure 3.10. The plot (a) displays the inverse behavior of the interfacial tension (mN/m) with the temperature (K) upturn at 10 (plus signs), 20 (circles), 30 (stars), 40 (squares), and 50 (triangles) MPa. Blue line in the plot (b) depicts the linear master curves fitting the interfacial tension at 10 MPa. The slope of this line is the surface entropy.

Lastly, we derive the surface entropy (*S*) from the fundamental thermodynamic equations to find more insights into the effect of temperature on the interfacial tension. We postulate that the surface entropy merely depends on the temperature in a system with relatively constant pressure. One approach is to calculate the surface entropy from the summation of the system enthalpy and the isobaric heat capacity [62]. Here, we propose a more efficient method to derive this surface entropy from the fundamental thermodynamic equations:

$$-S = \left(\frac{\partial G}{\partial T}\right)_{A,P} = \left(\frac{\partial \gamma}{\partial T}\right)_{A,P} \tag{3.18}$$

For instance, we obtain an entropy value of -133.48 kcal/mol at 298.15 K and 10 MPa, after multiplication by the area and unit conversion. A persistent negative surface entropy in the W/NG mixtures implies that increasing the system temperature must weaken the interfacial tension as a result of more molecular fluctuation and disorder at the interface, which follows the regular classical behavior with no anomaly, unlike several compounds such as para-azoxyanisole (PAA), p-anisaldazine, and some liquid crystals [63, 64].

3.7. Conclusions

In the current study, we employed molecular dynamics simulations to investigate the interfacial thermodynamics, mechanics, and chemical composition at the interface between natural gas and liquid water. We applied a specific NP_NAT ensemble which holds the cross-sectional area and the perpendicular pressure to the planar interface constant owing to the mechanical anisotropy and chemical asymmetry of the water-natural gas interfaces. Both conditions of this ensemble are critical to achieve reliable results in surface studies. The use of such ensemble improved the accuracy of the interfacial properties such as the surface tension, and diminished the deviation between the experiments and computational methods.

The interfacial density profile, surface excess, radial pair distribution function, and chemical compositions in both phases were computed to generate molecular-level characterization. Increasing the interfacial density and excess, and the distribution of the propane, ethane, and methane molecules near the water-gas interface suggests that the surface adsorbs the gas components in order of their size while heavy alkanes reveal lower solubility into the water phase. Priority in the anomalous adsorption of large saturated hydrocarbons such as propane onto the natural gas-water surface implies that the nucleation of structure II clathrates initiated at the interface is recognized as heterogeneous formation in the classical nucleation theory. After a complete enumeration of all hydrogen bonds adjacent to the interface, we speculated that the favorable interactions between the hydrogen bonds in water phase and hydrophobic hydrocarbons in gas phase can elucidate both high adsorption and low solubility of gas molecules, particularly in high pressure regime (P>10 MPa).

The interfacial tension values were calculated and evaluated on the basis of the available experimental data. In conjunction with the computational results, we used the classical scaling laws, for example, the Eötvös rule originated from fundamental thermodynamics to fully characterize the effects of the temperature and pressure on the interfacial properties including the surface tension, thickness, and entropy. We concluded that interfacial tension decreases with an increase in the system temperature and pressure up to 50 MPa. Given the substantial hydrocarbons adsorption at the interface acting as surfactant, the interfacial tension in a natural gas-water system is more attenuated than the liquid-vapor water or water-pure methane systems at the same temperature and pressure. We employed the adaptive ensemble to capture the elongation of the longitudinal box length and interfacial thickness with either pressure drop or temperature increase. In summary, these results comprehensively deliver a quantitative and qualitative characterization of the natural gas-water interface which is of great significance to basic surface science and emerging environmental applications.

3.8. Acknowledgements

SM appreciates the financial support of the McGill Engineering Doctoral Awards (MEDA) Grad Excellence Award. This research is supported by the Natural Sciences and Engineering Research Council (NSERC) through the Discovery Grants Program. We are grateful to Compute Canada and Calcul Québec for the access to HPC facilities and the technical supports. ADR is grateful to McGill University for financial support through the James McGill Professorship appointment.

3.9. References

1. Sloan, E.D., *Fundamental principles and applications of natural gas hydrates.* Nature, 2003. **426**(6964): p. 353-363.

2. Khadem, S.A. and R.B. Boozarjomehry, *Development of systematic framework for an intelligent decision support system in gas transmission network.* Industrial & Engineering Chemistry Research, 2015. **54**(43): p. 10768-10786.

3. Haynes, C.A. and R. Gonzalez, *Rethinking biological activation of methane and conversion to liquid fuels.* Nature chemical biology, 2014. **10**(5): p. 331-339.

4. Osborn, S.G., et al., *Methane contamination of drinking water accompanying gas-well drilling and hydraulic fracturing.* proceedings of the National Academy of Sciences, 2011. **108**(20): p. 8172-8176.

5. Harriss, R.C., et al., *Sources of atmospheric methane in the south Florida environment.* Global Biogeochemical Cycles, 1988. **2**(3): p. 231-243.

6. Faramawy, S., T. Zaki, and A.-E. Sakr, *Natural gas origin, composition, and processing: A review.* Journal of Natural Gas Science and Engineering, 2016. **34**: p. 34-54.

7. Khadem, S.A., et al., *Pressure and temperature functionality of paraffin-carbon dioxide interfacial tension using genetic programming and dimension analysis (GPDA) method.* Journal of Natural Gas Science and Engineering, 2014. **20**: p. 407-413.

8. Busch, A. and A. Amann-Hildenbrand, *Predicting capillarity of mudrocks.* Marine and petroleum geology, 2013. **45**: p. 208-223.

9. Nourbakhsh, A., *Determination of capillary pressure, relative permeability and pores size distribution characteristics of coal from Sydney basin-Canada.* 2012.

10. Sloan Jr, E.D. and C. Koh, *Clathrate hydrates of natural gases*. 2007: CRC press.

11. Jendi, Z.M., P. Servio, and A.D. Rey, *Ideal Strength of Methane Hydrate and Ice Ih from First-Principles.* Crystal Growth & Design, 2015. **15**(11): p. 5301-5309.

12. Vlasic, T.M., P. Servio, and A.D. Rey, *Atomistic modeling of structure II gas hydrate mechanics: Compressibility and equations of state.* AIP Advances, 2016. **6**(8): p. 085317.

13. Vlasic, T.M., P.D. Servio, and A.D. Rey, *Effect of Guest Size on the Mechanical Properties and Molecular Structure of Gas Hydrates from First-Principles.* Crystal Growth & Design, 2017. **17**(12): p. 6407-6416.

14. Carroll, J., *Natural gas hydrates: a guide for engineers*. 2014: Gulf Professional Publishing.

15. Koh, C.A., et al., *Fundamentals and applications of gas hydrates.* Annual Review of Chemical and Biomolecular Engineering, 2011. **2**(1): p. 237-257.

16. Knott, B.C., et al., *Homogeneous nucleation of methane hydrates: Unrealistic under realistic conditions.* Journal of the American Chemical Society, 2012. **134**(48): p. 19544-19547.

17. Sarupria, S. and P.G. Debenedetti, *Homogeneous nucleation of methane hydrate in microsecond molecular dynamics simulations.* The journal of physical chemistry letters, 2012. **3**(20): p. 2942-2947.

18. Bai, X.-M. and M. Li, *Test of classical nucleation theory via molecular-dynamics simulation.* The Journal of chemical physics, 2005. **122**(22): p. 224510.

19. Lupi, L., B. Peters, and V. Molinero, *Pre-ordering of interfacial water in the pathway of heterogeneous ice nucleation does not lead to a two-step crystallization mechanism.* The Journal of Chemical Physics, 2016. **145**(21): p. 211910.

20. Warrier, P., et al., *Overview: Nucleation of clathrate hydrates.* The Journal of Chemical Physics, 2016. **145**(21): p. 211705.

21. Kashchiev, D. and A. Firoozabadi, *Nucleation of gas hydrates.* Journal of Crystal Growth, 2002. **243**(3–4): p. 476-489.

22. Kashchiev, D., *Nucleation : basic theory with applications*. 2000, Butterworth Heinemann: Oxford.

23. Bagherzadeh, S.A., et al., *Influence of hydrated silica surfaces on interfacial water in the presence of clathrate hydrate forming gases.* The Journal of Physical Chemistry C, 2012. **116**(47): p. 24907-24915.

24. Bai, D., et al., *How properties of solid surfaces modulate the nucleation of gas hydrate.* Scientific reports, 2015. **5**: p. 12747.

25. Liang, S. and P.G. Kusalik, *The nucleation of gas hydrates near silica surfaces.* Canadian Journal of Chemistry, 2014. **93**(8): p. 791-798.

26. Aman, Z.M. and C.A. Koh, *Interfacial phenomena in gas hydrate systems.* Chemical Society Reviews, 2016. **45**(6): p. 1678-1690.

27. Grimvall, G., *Chapter 6 - The phonon spectrum*, in *Thermophysical Properties of Materials*. 1999, Elsevier Science B.V.: Amsterdam. p. 79-111.

28. Kashchiev, D. and A. Firoozabadi, *Induction time in crystallization of gas hydrates.* Journal of crystal growth, 2003. **250**(3-4): p. 499-515.

29. Hayama, H., et al., *Interfacial tension between (methane+ ethane+ propane) gas mixture and water from 283.2 K to 298.2 K under up to 10 MPa.* The Journal of Chemical Thermodynamics, 2017. **108**: p. 71-75.

30. Speight, J.G., *Chapter 5 - Properties of Organic Compounds*, in *Environmental Organic Chemistry for Engineers*, J.G. Speight, Editor. 2017, Butterworth-Heinemann. p. 203-261.

31. Wang, L.-K., et al., *Experimental study on the solubility of natural gas components in water with or without hydrate inhibitor.* Fluid Phase Equilibria, 2003. **207**(1-2): p. 143-154.

32. Demirbas, A., *Methane gas hydrate*. 2010: Springer Science & Business Media.

33. Klauda, J.B. and S.I. Sandler, *Global distribution of methane hydrate in ocean sediment.* Energy & Fuels, 2005. **19**(2): p. 459-470.

34. Binks, B.P. and J.H. Clint, *Solid wettability from surface energy components: relevance to pickering emulsions.* Langmuir, 2002. **18**(4): p. 1270-1273.

35. Vázquez, U.O.M., et al., *Calculating the surface tension between a flat solid and a liquid: a theoretical and computer simulation study of three topologically different methods.* Journal of Mathematical Chemistry, 2009. **45**(1): p. 161-174.

36. Chaplin, M., *Theory vs experiment: what is the surface charge of water?* Water Journal Multidisciplinary Research Journal 1, 2009: p. 1-28.

37. Eisenberg, D., D.S. Eisenberg, and W. Kauzmann, *The structure and properties of water*. 2005: Oxford University Press on Demand.

38. Biscay, F., et al., *Monte Carlo simulations of the pressure dependence of the water− acid gas interfacial tensions.* The Journal of Physical Chemistry B, 2009. **113**(43): p. 14277-14290.

39. Biscay, F., et al., *Monte Carlo calculation of the methane-water interfacial tension at high pressures.* The Journal of chemical physics, 2009. **131**(12): p. 124707.

40. Noya, E.G., C. Vega, and E. de Miguel, *Determination of the melting point of hard spheres from direct coexistence simulation methods.* The Journal of chemical physics, 2008. **128**(15): p. 154507.

41. Ikeguchi, M., *Partial rigid-body dynamics in NPT, NPAT and NPγT ensembles for proteins and membranes.* Journal of computational chemistry, 2004. **25**(4): p. 529-541.

42. Kvamme, B., T. Kuznetsova, and K. Schmidt. *Experimental measurements and numerical modelling of interfacial tension in water-methane systems*. in *Presentation at the International Conference of Computational Methods in Sciences and Engineering, Chania, Greece*. 2006.

43. Schmidt, K.A., G.K. Folas, and B. Kvamme, *Calculation of the interfacial tension of the methane–water system with the linear gradient theory.* Fluid Phase Equilibria, 2007. **261**(1): p. 230-237.

44. Kirkwood, J.G. and F.P. Buff, *The statistical mechanical theory of surface tension.* The Journal of Chemical Physics, 1949. **17**(3): p. 338-343.

45. Ghoufi, A. and P. Malfreyt, *Calculation of the surface tension and pressure components from a non-exponential perturbation method of the thermodynamic route.* The Journal of chemical physics, 2012. **136**(2): p. 024104.

46. Tolman, R.C., *Consideration of the Gibbs theory of surface tension.* The journal of chemical physics, 1948. **16**(8): p. 758-774.

47. Ghadar, Y. and A.E. Clark, *Intermolecular network analysis of the liquid and vapor interfaces of pentane and water: microsolvation does not trend with interfacial properties.* Physical Chemistry Chemical Physics, 2014. **16**(24): p. 12475-12487.

48. Horn, H.W., et al., *Development of an improved four-site water model for biomolecular simulations: TIP4P-Ew.* The Journal of chemical physics, 2004. **120**(20): p. 9665-9678.

49. Jorgensen, W.L., J.D. Madura, and C.J. Swenson, *Optimized intermolecular potential functions for liquid hydrocarbons.* Journal of the American Chemical Society, 1984. **106**(22): p. 6638-6646.

50. Plimpton, S., *Fast parallel algorithms for short-range molecular dynamics.* Journal of computational physics, 1995. **117**(1): p. 1-19.

51. Hockney, R.W. and J.W. Eastwood, *Computer simulation using particles*. 1988: crc Press.

52. Isele-Holder, R.E., W. Mitchell, and A.E. Ismail, *Development and application of a particle-particle particle-mesh Ewald method for dispersion interactions.* The Journal of chemical physics, 2012. **137**(17): p. 174107.

53. Rowlinson, J.S. and B. Widom, *Molecular theory of capillarity*. 2013: Courier Corporation.

54. Mirzaeifard, S., P. Servio, and A.D. Rey, *Molecular dynamics characterization of temperature and pressure effects on the water-methane interface.* Colloid and Interface Science Communications, 2018. **24**: p. 75-81.

55. Blokhuis, E., et al., *Tail corrections to the surface tension of a Lennard-Jones liquid-vapour interface.* Molecular Physics, 1995. **85**(3): p. 665-669.

56. Chapela, G.A., et al., *Computer simulation of a gas–liquid surface. Part 1.* Journal of the Chemical Society, Faraday Transactions 2: Molecular and Chemical Physics, 1977. **73**(7): p. 1133-1144.

57. Grest, G.S., et al., *Substructured multibody molecular dynamics*. 2006, Sandia National Laboratories.

58. Sakamaki, R., et al., *Thermodynamic properties of methane/water interface predicted by molecular dynamics simulations.* The Journal of chemical physics, 2011. **134**(14): p. 144702.
59. Scharlin, P., et al., *Solubility of gases in water: Correlation between solubility and the number of water molecules in the first solvation shell.* Pure and applied chemistry, 1998. **70**(10): p. 1895-1904.
60. Udeagbara, S.G., *Effect of Temperature and Impurities on Surface Tension of Crude Oil*. 2010: Universal-Publishers.
61. McCain, W.D., *The properties of petroleum fluids*. 1990: PennWell Books.
62. Jacobson, L.C., W. Hujo, and V. Molinero, *Thermodynamic stability and growth of guest-free clathrate hydrates: a low-density crystal phase of water.* The Journal of Physical Chemistry B, 2009. **113**(30): p. 10298-10307.
63. Chandrasekhar, S., *Liquid Crystals*. 2nd ed. 1992: Cambridge University Press. p. 80-84.
64. Rey, A.D., *Modeling the Wilhelmy surface tension method for nematic liquid crystals.* Langmuir, 2000. **16**(2): p. 845-849.

Chapter 4. Modeling and Simulation of Water and Methane Hydrate Crystal Interface

4.1. Preface

The mechanical definition of the interfacial tension is employed on the non-planar interface of the methane hydrate crystals. Moreover, the elastic deformation of such crystalline solid is considered. The interfacial tension between the liquid water and methane hydrate is calculated to understand the how the surface reacts faced with pressure and temperature change. This chapter is reproduced with permission from "Mirzaeifard, S., P. Servio, and A.D. Rey, Modeling and simulation of water and methane hydrate crystal interface. Crystal Growth & Design, 2019. 19: p. 5142-5151. Copyright 2019 American Chemical Society".

4.2. Abstract

Water-methane hydrate interfaces are ubiquitous in oil and gas technologies and in nature. The structure and properties of this liquid/crystal interface plays a significant role in transport phenomena between the bulk phases. In this paper, we use molecular dynamics techniques to characterize the liquid water-crystalline methane hydrate in the bulk and, particularly, the interface. We show that the interfacial mechanical approach based on the novel constant normal pressure-cross-sectional area (NP_NAT) ensemble with a computational slab length equal to the lattice parameter of the methane clathrates can accurately predict the interfacial free energy of a curved interface. Notably, the computational platform for the interfacial tension characterization includes contributions from elastic strains. In the studied temperature and pressure ranges, we find that the interfacial tension slightly increases with temperature upturn or pressure drop due to less disordered orientation and dispersed distribution of the molecules at the interface. We generate a full molecular-level characterization by computing the excess enthalpy and stress, local density profile, radial distribution function, hydrogen bonding density, and charge distribution to confirm the observed interfacial tension trend, which significantly contributes to the evolving understanding of gas hydrate formation.

4.3. Keywords

water-methane hydrate interface; surface physics; interfacial tension; molecular dynamics simulation; NP_NAT ensemble.

4.4. Introduction

Under favorable thermodynamic conditions of low temperature and high pressure, water and gas molecules form a crystalline guest-host solid material known as a clathrate or gas hydrate, where the water forms an ordered hydrogen-bonded network that encapsulates the guest gas [1]. These clathrates can form several crystalline structures depending on the size and properties of the encapsulated gas molecules, including sI [2] sII [3, 4], and sH [5]. In this work, we focus on methane gas as the trapped guest molecule in water cavities forming the sI hydrate phase, since the methane hydrate is the most common and important gas hydrate [6, 7].

A fundamental understanding of hydrate nucleation forms the basis to control their formation by inhibition or promotion processes. On the basis of the application of classical nucleation theory (CNT) to elucidate clathrate formation [1, 8-10], a complete knowledge of the interfacial energy contributions between all the involved phases, including the hydrate-liquid, is critically needed but currently poorly understood [11, 12]. According to CNT, the formation work is the sum of a spontaneously driven supersaturation and a surface energy contribution [13]:

$$W(J) = -n\Delta\mu + c(nv_h)^{\frac{2}{3}}\sigma \tag{4.1}$$

where n, $\Delta\mu(J)$, c, v_h (m^3), and σ (J/m^2) represent the crystal unit cell number, chemical potential difference (supersaturation), shape factor, hydrate volume, and surface energy, respectively. Figure 4.1 shows representative examples of the water-hydrate interactions in different morphologies [14], depending on many factors such as the involved phases [15] and fluid flow [16-18]. Undeniably, there exists a need for extensive characterization of the interfacial tension at the liquid water-clathrate interface, which is shared among all the formation processes. The distribution of hydrate in nature emphasizes the prominence of surface energy, which dictates the optimal morphology and location in the hydrate formation process and its growth rate underlying the Gibbs-Duhem equation [15]. The interfacial tension extensively contributes to the total free energy owing to the normally large surface area engaged in the hydrate systems. The aggregation of hydrate particles is a function of this hydrate-water interfacial tension.

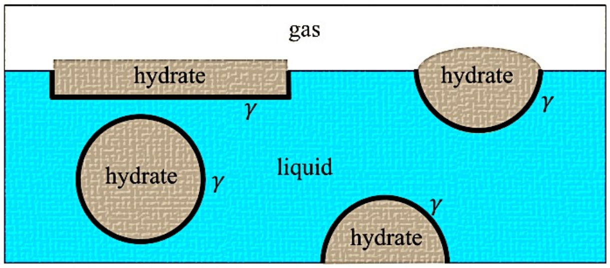

Figure 4.1. Schematic of water/hydrate interfaces under different nucleation conditions. γ denotes the interfacial tension of this interface.

A better understanding of interfacial phenomena facilitates the control of the macroscopic behavior of hydrate solutions in nature and technologies in the energy industries based on hydrates. For instance, we may inhibit the hydrate formation in both unconventional and traditional fuel production systems by adsorbing surfactant obtained from synthetic and natural sources [15]. In addition to the formation process, the phase transitions and thermodynamic stability are regulated by the interfacial properties influenced by molecular interactions and structure, which highlights the great importance of surface investigations [1, 15, 19, 20].

The mixture of sI methane hydrate in direct contact with liquid water can have significant implications in flow assurance (i.e., management of fluid transportation in multiphase flow), clean energy resources, gas storage and transportation, climate change, environmental processes, and reservoirs associated with the petroleum industries [19-24]. In all of these applications, interfacial transport phenomena and thermodynamics are essential for process control and simulation [25-27]. Nevertheless, the characterization and molecular-level understanding are precluded without inputs from simulation [28, 29]. Hence, a combination of the analytical theory with numerical computation on the interface between the water and methane hydrate forms the main scope of this work. However, molecular simulations have their own computational challenges in capturing the thermodynamics and physics of the liquid-crystal interfaces due to factors such as sudden density change, unrealistic fluctuations, hydrogen and ion bonding, and adequate time and length scales to obtain sensible results [30, 31]. In this work we use specifically tailored molecular dynamic (MD) techniques combined with sophisticated analytical theory to investigate the thermodynamic and mechanic parameters at the bulk and interface as a function of temperature and pressure on both microscopic and macroscopic scales.

Since the water-methane hydrate mixture displays chemical and structural asymmetry and mechanical anisotropy across the interface, we must tackle this system with an appropriate statistical ensemble to predict accurate results. Therefore, we employ the unique NP_NAT ensemble to constrain and control the cross-sectional area (A) and the perpendicular pressure (normal stress component) imposed on the interface (P_N) inspired by its application in other systems with anisotropic interfaces [32-34] including liquid-solid mixtures [35].

In this computational study, we use the well-known mechanical definition of the interfacial tension over the thermodynamic approach [36-39], although we acknowledge that both local and global perspectives can yield high accuracy [39, 40]. The only issue for the mechanical approach is that it is generally applicable to infinite, nonplanar (curved) interfaces [39, 41]. Here, we demonstrate that we may remarkably overcome these issues, allowing us to generate accurate results using a proper MD ensemble and slab length along with an interfacial energy term correction discussed below. To capture the interfacial tension at the desired interface, we require a complete knowledge of the stress tensor which governs the mechanics of the interface. Hence, we follow the Kirkwood and Buff method to obtain all the local components of the tensorial pressure at the water-methane hydrate interface [38]. Additionally, since the mixture interface interpolates a liquid on one side and a crystal on the other, the elastic deformation of the solid surface might influence the interfacial tension via the addition of a reversible work per interfacial area to elastically stretch the surface. This work represents the surface energy change with strain, and it must be included in all the stress-sensitive interfaces, particularly the crystal or solid surfaces, so that the interfacial tension and free energy of the liquid-crystal mixtures are different [42-47]. We generalize the formula of the interfacial tension to incorporate the elastic deformation energy using the Shuttleworth equation [48-51]. In particular, we demonstrate the need and importance of this elastic correction to the interfacial tension in the field of gas hydrates.

In addition, we seek to understand how this interfacial tension behaves while being subjected to pressure and temperature changes. To the best of our knowledge, this is the first work that reports the interfacial tension at a wide range of practical temperatures and pressures considering the elastic deformation of the crystalline methane hydrate at the interface. Furthermore, this study explains how the molecular orientation, hydrogen bonding network, charge distribution, and local mass density at the interface relate to the interfacial tension.

The organization of this work is as follows. In the following section, we present the modeling and MD simulation details in conjunction with the computational approach for the interfacial tension. In the next section, we report the pressure and temperature effects on the local density and potential energy, the lattice parameter effect, interfacial tension, excess enthalpy and entropy, adsorption, radial distribution function, hydrogen bonding density, and charge distribution. Finally, we conclude the paper with the substantial potential effect of the novel results of this study on present and future work of gas hydrate physics and technologies.

4.5. Methodology

4.5.1. Model and Computational Methods

We confine the methane hydrate phase between two liquid water phases as previously done [38, 52]. The crystalline hydrate phase with 100% cage occupancy contains 1328 methane and 7636 water molecules surrounded by 5468 liquid water molecules in a 3D simulation box with an initial size of 48 × 48 × 200 Å and periodic boundary conditions. Figure 4.2 displays a schematic diagram and snapshot sample of a typical initial configuration of this system [38, 52].

In this study, we use the LAMMPS software [53] to simulate the force fields for the methane and water molecules using the united atom optimized potentials for liquid simulations (OPLS-UA) [54] and transferable intermolecular potential with the four points (TIP4P) models [55], respectively. In addition, we implement the TIP4P-optimized particle-particle particle-mesh (PPPM) method with the force computation accuracy of 10^{-5} devised by Hockney and Eastwood [56, 57] to compute the Coulombic electrostatic interactions. We also apply the Lennard-Jones (LJ) potential with Lorentz-Berthelot mixing rule to account for the intermolecular interactions:

$$U_{LJ}(r) = 4\varepsilon\left[\left(\frac{\sigma}{r}\right)^{12} - \left(\frac{\sigma}{r}\right)^{6}\right] \tag{4.2}$$

$$\varepsilon_{ij} = \sqrt{\varepsilon_{ii}\varepsilon_{jj}}\ ,\ \sigma_{ij} = \frac{\sigma_{ii}+\sigma_{jj}}{2} \tag{4.3}$$

where ε, σ, and r represent the LJ potential well depth, the finite distance at zero potential, and the particle distance, respectively, as shown in Figure 4.2 [54, 55]. The cutoff distance of both the LJ and Coulombic electrostatic interactions is chosen to be 12 Å. Moreover, we utilize the Shake algorithm to constrain the water molecules so that the existing bond lengths and angles refrain from any considerable change throughout the simulations.

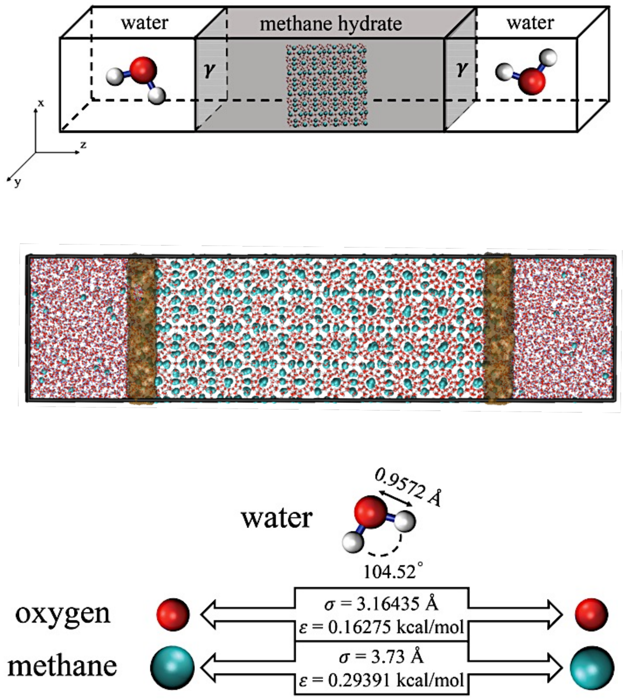

Figure 4.2. Simulation template showing the red, white, and green particles as oxygen atoms, hydrogen atoms, and methane molecules, respectively. The brown regions on both sides denote the interfacial zones, which separate the liquid and crystal phases.

We choose a time step of 2 fs through the Verlet algorithm to integrate the non-Hamiltonian equations of motion. The applied thermostat and barostat are Nose-Hoover and Parrinello-Rahman, respectively, to adjust the temperature and pressure of the system using a damping constant of 4 ps for the characteristic fluctuations. Please note that the damping constant must not be undervalued, as we may accommodate large pressure fluctuations in such solid-liquid systems, which adds to the high complexity of the tensorial pressure calculations. To sample the system configurations, we initially run the simulations for 300 ns using the isothermal-isobaric (*NPT*) ensemble to reach the equilibrium and appropriate lattice parameters at each temperature and pressure. We ensure thermodynamic equilibrium by a series of calculations on the correlation factors of mechanical and thermodynamic properties. We further carry out the simulations for 20 ns employing the isothermal-isobaric-isointerface area (NP_NAT) ensemble, which demands a constant normal pressure (P_N) imposed onto an interface with a persistent cross-sectional area (A) to accurately capture the interfacial phenomena. Constraining the normal pressure and contact surface will help to overcome the aforementioned issue of pressure control in solid mixtures. We analyze and report the data collected from the last 10 ns of the simulation run to guarantee accurate results.

4.5.2. Interfacial Tension

We calculate the interfacial tension the following equation based on Bakker's method (γ_B) [58]:

$$\gamma_B = \frac{1}{2}\int_{-\infty}^{+\infty}\left(P_N - P_T(z)\right) dz \tag{4.4}$$

where P_N and P_T denote the normal and tangential pressures, respectively. P_N and P_T can be obtained from the stress tensor given the relations below [59]:

$$P_N = P_{zz} = P \ , \ P_T = \frac{1}{2}\left(P_{xx} + P_{yy}\right) \tag{4.5}$$

If we neglect the tensorial pressure fluctuations, P_N and P_T are essentially identical along the simulation box apart from the interfaces owing to a substantial drop in the tangential pressure. Please note that Eqn. 4.4 is an average of the two standing interfaces on both sides of the methane clathrate phase, which enhances accuracy. Furthermore, the interfacial tension for inhomogeneous multicomponent systems requires a long-range or tail correction to compensate the under-estimated interatomic interactions caused by the truncation error of setting a cutoff distance [60-62]. Blokhuis *et al.* developed the following formula to calculate the correction term [60]:

$$\gamma_{tail} = \int_0^1 \int_{r_c}^{\infty} 12\pi\varepsilon\sigma^6 {\Delta\rho_{HL}}^2 \left(\frac{3s^3 - s}{r^3}\right) cot\left(\frac{rs}{t}\right) dsdr \tag{4.6}$$

where r_c, t, s, and $\Delta\rho_{HL}$ represent the cutoff distance, interfacial thickness, position, and molecular density difference between the hydrate and liquid phases, respectively.

According to the Shuttleworth equation, the interfacial tension is the sum of the interfacial free energy (θ) and the derivative of the interfacial energy with respect to the deformation or strain (τ) [45, 47]:

$$\gamma = \theta + A\frac{\partial\theta}{\partial A} = (\gamma_B + \gamma_{tail}) + A\frac{\partial(\gamma_B + \gamma_{tail})}{\partial A} \tag{4.7}$$

We use a combination of adaptive *NPT* and *NP_NAT* ensembles throughout the simulations to achieve both cross-sectional area variation and precise interfacial energy calculation. Whenever possible the fidelity of the methods and predictions is established with experimental data.

4.6. Results and Discussion

The first step is to find the local density profile of the mixture to perform the tail correction (Eqn. 4.6). The local density is influenced more by the system temperature than the pressure. Figure 4.3 clearly shows that these density values abruptly decrease as we move from the liquid water phase to the crystalline methane clathrate phase. Such a decrease coincides with an increase in the local potential energy across the interface, as demonstrated in Figure 4.4. We fit the density profiles by the standard hyperbolic tangent function to obtain the water and methane hydrate density.

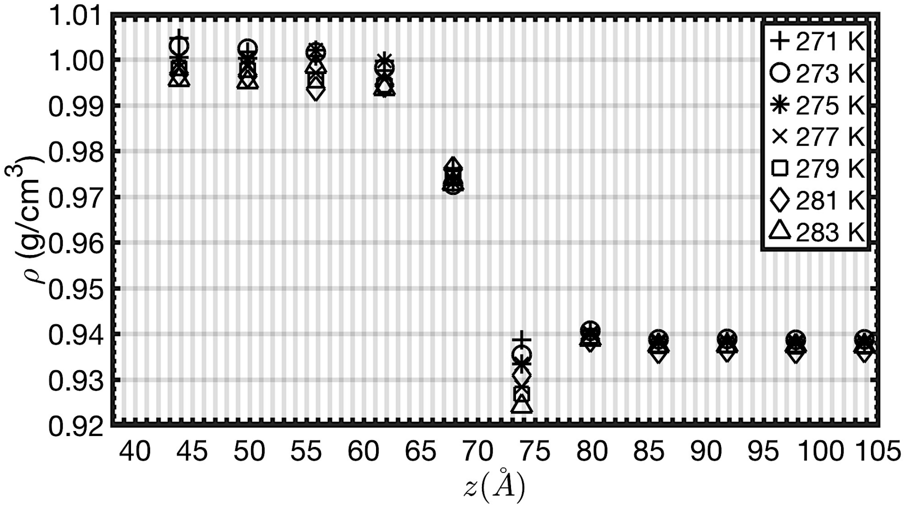

Figure 4.3. Local density profiles (g/cm^3) of the water-methane hydrate mixture along the simulation box at 10 MPa and different temperatures. The plus sign, circle, star, cross, square, diamond, and triangle markers represent the system temperatures of 271, 273, 275, 277, 279, 281, and 283 K, respectively.

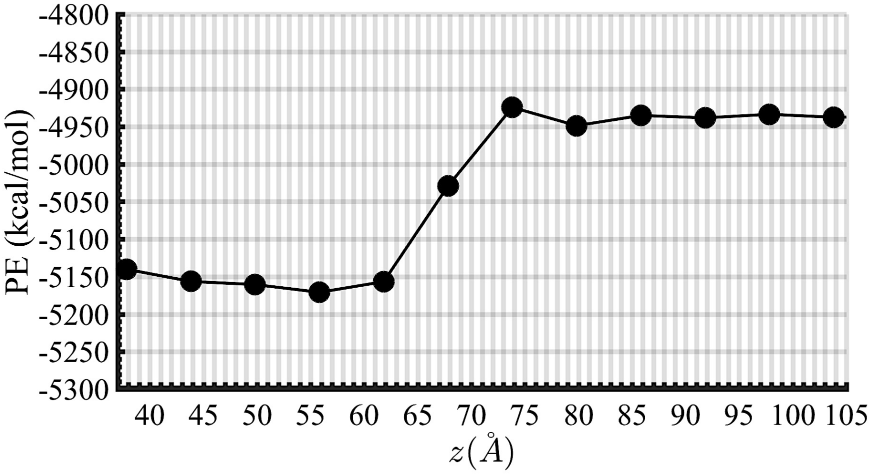

Figure 4.4. Potential energy (kcal/mol) of the system along the z direction at 10 MPa and 275 K. The potential exhibits a sudden upturn from the liquid water phase to the methane hydrate crystal phase.

We divide the simulation box into several slabs to separately perform the interfacial energy calculation for all slabs. Each slab holds the same planar area in the x-y plane with a constant length along the z direction. This slab length should be carefully chosen to avoid fluctuations in material properties. The appropriate moving average method and slab length are crucial to fully control the pressure of such crystalline solid-liquid mixture; see Figure 4.5 for representative results on the effect of length scale on the oscillatory behavior of the pressure. Therefore, we systematically increase the slab length from low to high values and calculate the difference of the normal and tangential pressures, which is critical for the interfacial energy calculation. Figure 4.6 shows that 12 Å is the shortest length that damps the fluctuation and provides accurate results. Not surprisingly, this length is equal to the lattice parameter of methane hydrate [1, 63]. That is why a length of 6 Å, which is half the lattice parameter, reveals less fluctuation than 9 Å. This approach allows us to transform a nonplanar crystal surface into a planar surface to resolve the issues of the mechanical definition of interfacial tension.

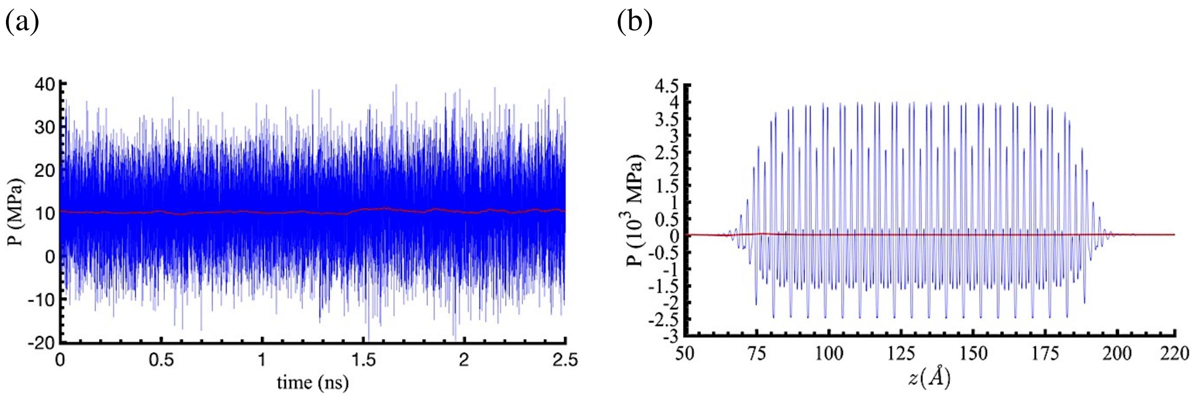

Figure 4.5. Representative pressure oscillations of the methane hydrate-liquid water mixture at 10 MPa and 275 K. In (a), the blue line shows the measured pressure without a damping constant or averaging method. The red line represents the pressure for a system with the use of sufficient damping constant and moving average method. In (b), there is a depiction the intense pressure fluctuations when a short slab length is used. The blue and red represent the local pressure with slab lengths of 0.5 and 12 Å, respectively.

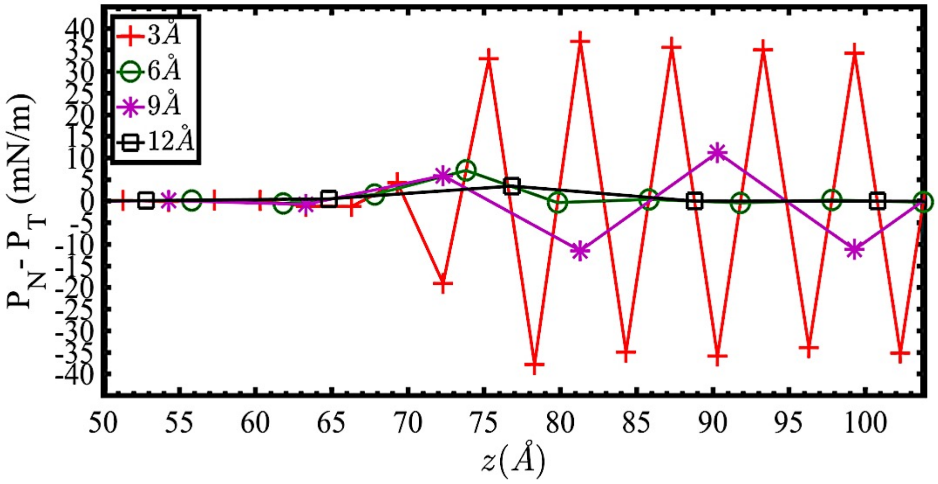

Figure 4.6. Different slab lengths change the difference between the normal and tangential pressures multiplied by the unit length. The temperature of the system is 275 K, and the pressure is 10 MPa. Red plus signs, green circles, purple stars, and black squares represent slab lengths of 3, 6, 9, and 12 Å, respectively.

With the use of an appropriate slab length, we calculate the interfacial energy and its changes with the elastic deformation. As per Eqn. 4.7, we require these two components to calculate the interfacial tension between the water and methane clathrate phases. Figure 4.7 shows that the interfacial energy decreases as we increase the temperature of the system over a wide range of pressure (5-30 MPa). Such a trend for the interfacial energy is observed for the liquid water and methane gas mixtures [33, 36, 37, 64-66]. In contrast to the interfacial energy, the τ contribution increases with the system temperature. The τ values are consistent with the reported results for other crystals and metals [67]. One reasonable explanation is that the temperature rise causes a greater interaction mismatch due to the thermal expansion between the liquid and crystal phases, but the exact calculation of thermal expansion coefficients is beyond the scope of this work. The surface water can be further influenced by the strain, as the structure is better ordered than that of regular liquid water, which could possibly adjust the increase in the lattice and thermal stress which originated from the hydrate phase with temperature increase. This effect understandably corroborates the contribution of the thermal strain in the interfacial tension. Therefore, different pressure regimes at constant temperature reveal a very similar behavior concerning the interfacial crystal elasticity, except for the system with a pressure of 5 MPa because of naturally intense fluctuations in MD simulations of the systems at low pressures.

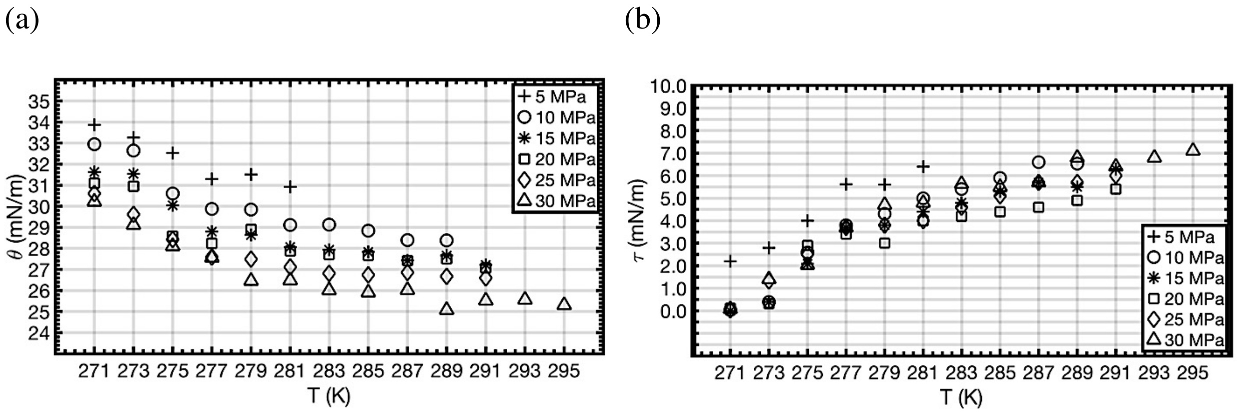

Figure 4.7. (a) Depiction of the interfacial energy decreases with the system temperature at different pressures. (b) Variation of the interfacial energy under elastic deformation. The plus sign, circle, star, square, diamond, and triangle markers represent system pressures of 5, 10, 15, 20, 25, and 30 MPa, respectively.

We now combine these two interface and elastic energies terms to obtain the interfacial tension for the systems with systematic increases in the temperature and pressure. Figure 4.8a evidently exhibits a monotonic increase in the interfacial tension of a water-methane hydrate mixture with temperature. Such an increase in interfacial tension is also observed for other materials such as liquid crystals and ice-water mixtures [68-75]. However, the interfacial tension decreases as the pressure of the system increases, following the regular classical behavior until it reaches a plateau due to the very limited compressibility of liquid water and crystalline hydrate (see Figure 4.8b). These interfacial tension trends with temperature and pressure are also compatible with the surface energy contribution in Eqn. 4.1 since we already know, from thermodynamics, that the hydrates are more likely to form in a high-pressure and low-temperature regime that imparts a minimum formation work of the surface. Table 4.1 presents the interfacial tension values reported in the literature, and they are in excellent agreement with those predicted and explained in this work in Figure 4.8, with approximately a 1.94% deviation. Please note that this deviation is 7.83% when the contribution of the interfacial elastic deformation is neglected.

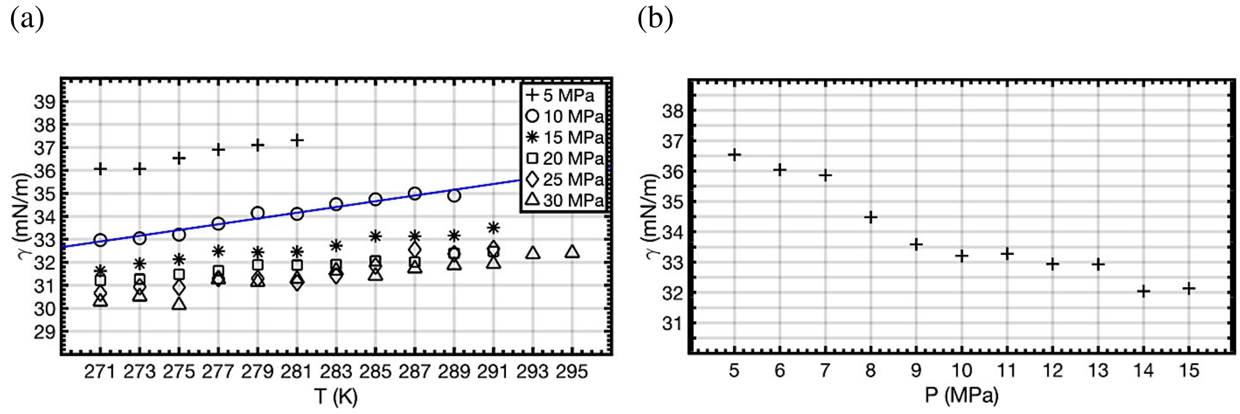

Figure 4.8. Interfacial tension values (mN/m) for the mixture of water and methane hydrate with increasing system temperature (a) and pressure (b). In (b) there are the results of a mixture at 275 K. The plus sign, circle, star, square, diamond, and triangle markers denote pressures of 5, 10, 15, 20, 25, and 30 MPa, respectively. The blue line presents the fitting curve for the system at 10 MPa.

Table 4.1. Interfacial tension at the water-methane hydrate interface

Investigators	Year	P (MPa)	T (K)	Interfacial tension (mN/m)
Naeiji *et al.*[76]	2017	15	275	31.710
Naeiji *et al.*[76]	2017	20	275	30.776
Jacobson *et al.*[77]	2011	6	275	36±2
Anderson *et al.*[78]	2003	10	275	32±3
Uchida *et al.*[79]	2002	10	275	34±6

Direct numerical simulation (DNS) was utilized in this study to calculate the interface excess enthalpy (H^{ex}) in order to verify the interfacial tension trends with temperature and pressure presented in Figure 4.8. Figure 4.9 depicts that the excess enthalpy (H^{ex}) increases with a temperature upturn or with a pressure drop, which is consistent with the interfacial tension increase.

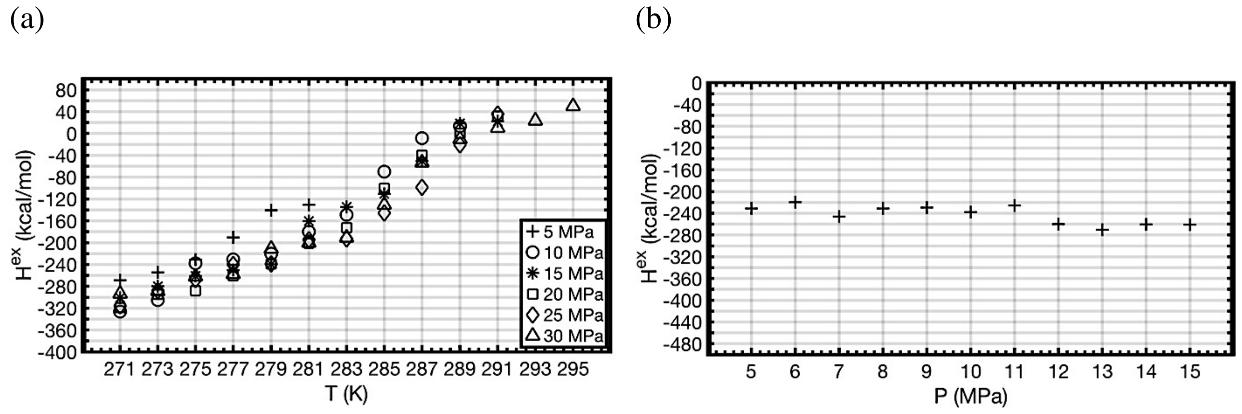

Figure 4.9. Excess enthalpy (kcal/mol) of the system with systematic change of temperature (a) and pressure (b). The system temperature for the results shown in (b) is 275 K. The excess enthalpy increases as the temperature increases or the pressure decreases. The plus sign, circle, star, square, diamond, and triangle markers are systems with pressures of 5, 10, 15, 20, 25, and 30 MPa, respectively.

In addition, the excess enthalpy data allow us to calculate the interface excess entropy (S^{ex}) by the thermodynamic relation for Helmholtz free energy [80]:

$$\gamma A = H^{ex} - (PV)^{ex} - TS^{ex} \tag{4.8}$$

Moreover, we can exploit the fundamental thermodynamic equations and seek more insights into the excess entropy of the mixture in units of kcal/mol using appropriate unit conversions:

$$S^{ex} = -\left(\frac{\partial G}{\partial T}\right)_{A,P} = -\left(\frac{\partial \gamma}{\partial T}\right)_{A,P} \tag{4.9}$$

Hence, we first fit the interfacial tension data of the mixture at 10 MPa with a linear master curve to report the increasing tension (in units of mN/m):

$$\gamma = 0.12\,T - 0.99 \tag{4.10}$$

Figure 4.10 shows that the excess entropy values obtained from these two distinct methods deviate by 0.88%, which shows very good agreement between the theory and direct computational thermodynamics. As the system temperature increases, the molecular orientation at the interface becomes less disordered with low fluctuation that consequently weakens the surface entropy and promotes the interfacial tension. In comparison to the water bulk phase, the well-ordered water molecules at the interface inhibit the water molecular rotations, which lessen the dielectric constant of the interfacial liquid water adjacent to the crystal surface [81]. Subsequently, this lower water dielectric constant coincides with a tension increase [82, 83]. Interestingly, such anomalous behavior does not obey the regular classical entropic effects, which normally shows an increase with the temperature.

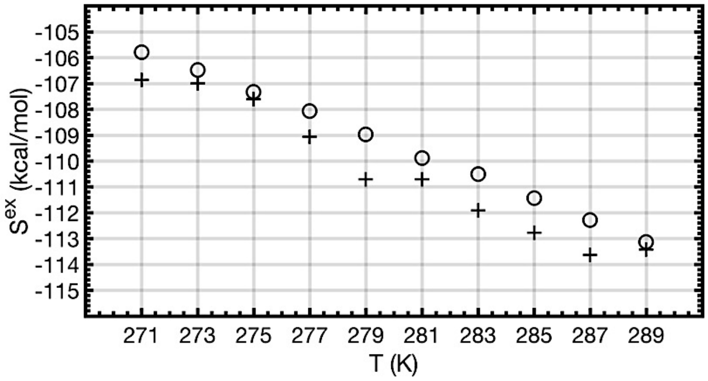

Figure 4.10. Interfacial excess entropy decreases as the temperature increases. The plus sign and circle markers represent the data obtained from theory and computational thermodynamics, respectively.

The intermolecular attractions at the interface can suppress the force imbalance leading to the tension decrease. Therefore, an investigation of the interfacial adsorption of the molecules could explain the irregular increase in the interfacial tension with the temperature. Figure 4.11 depicts that the adsorption of the water molecules onto the water-methane hydrate interface disappears with a temperature increase or pressure decrease. We choose a slab length of 1 Å to obtain an accurate local density profile. The density fluctuations on the right side refer to the crystalline structure of the methane clathrate phase.

Physical van der Waals forces, not chemical interactions, between the guest methane molecules and the host water molecules inside the hydrogen-bonded hydrate cavities provide a sufficiently stable fully occupied crystalline solid. From a microscopic point of view, the temperature increase at constant pressure leaves the solubility in the hydrate phase unaffected with nearly constant cohesive forces in the bulk and yet creates larger thermal activity of the water molecules at the interface to disperse the adhesive action, which allows the interfacial tension readily to grow [92]. On the other hand, the increase of system pressure at constant temperature minimizes the tension at the interface by rearranging the interfacial molecules such that they maximize their contacts inside the surrounding environment.

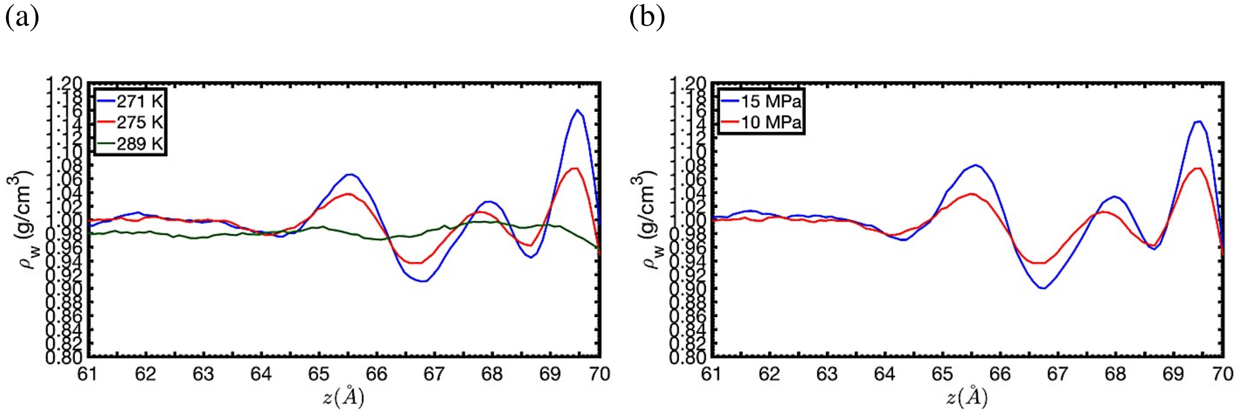

Figure 4.11. Local density profile of the water molecules demonstrates the interfacial adsorption. The molecular adsorption at the interface vanishes as the temperature increases and the pressure decreases. Please note that the interfacial center exists at z ≈ 66 Å with the liquid water phase on the left and the crystalline methane hydrate phase on the right side. The blue, red, and green lines in (a) represent system temperatures of 271, 275, and 289 K, respectively, at 10 MPa. The blue and red lines in (b) denote system pressures of 15 and 10 MPa, respectively, at 275 K.

Next, we report the radial pair distribution function (g) to examine the structure of the water molecules in the bulk and the interfacial region. Figure 4.12a shows that the water molecules become dispersed and disordered as we move from the structured order of the hydrate bulk to the water bulk organization, which is concluded from short and fewer peaks, respectively. This transition influences the interfacial adsorption of the surface water molecules. In addition to what has been discussed, Figure 4.12b represents the interfacial distribution functions between the methane molecules and the oxygen and hydrogen atoms of the water molecules. A higher peak for the oxygen atoms suggests a water molecule orientation with the negative charge toward the methane molecules near the interface.

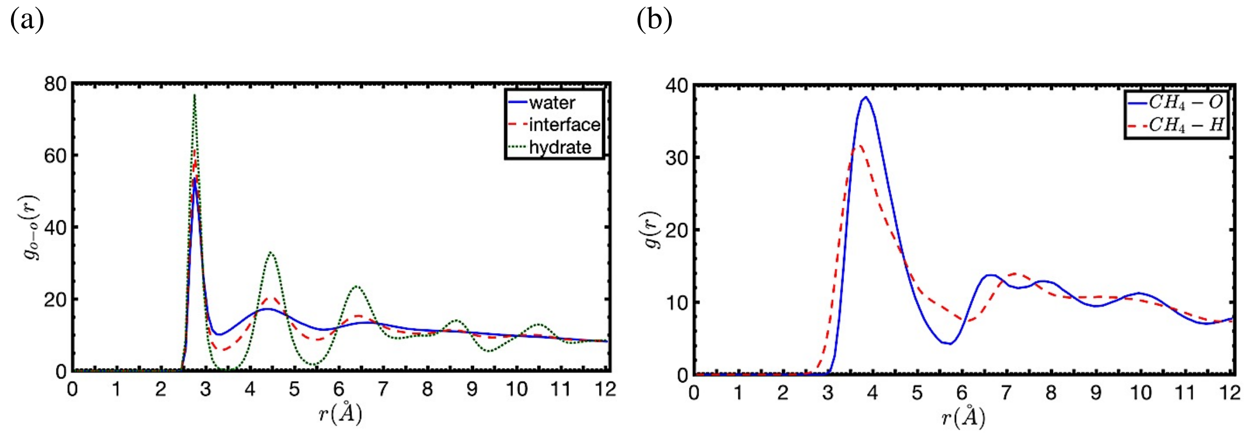

Figure 4.12. (a) Radial pair distribution function between the oxygen atoms in the water bulk (the solid blue line), interface (the dashed red line), and methane hydrate bulk (the dotted green line). (b) Radial pair distribution function between the methane molecules and the oxygen atoms (the solid blue line) and the methane molecules and the hydrogen atoms (the dashed red line) at the interface. The temperature and pressure of the mixture are 275 K and 10 MPa.

Additional important insights are gleaned from the hydrogen-bonding density near the interface at different temperatures and pressures. We define the distance and angle between the acceptor and donor of the hydrogen bonds subject to constraints. The criterion is that the O···O−H angle and distance between oxygen atoms must be less than 30° and 3.5 Å, respectively. The hydrogen-bonding network near the interface might indirectly affect the surface free energy through the interfacial adsorption and the incompatible interaction with the hydrate lattice. A favorable interaction between the hydrogen bonds and the molecules at the interfacial zone leads to the molecular adsorption. In the liquid water-methane gas mixture, a peak in the number of hydrogen bonds has been observed to explain adsorption onto the interface [33, 64, 66, 84]. Conversely, Figure 4.13 shows a minimum in the hydrogen bond density profile near the interface of the liquid water-methane clathrate mixture at the different temperature and pressure regimes. Temperature increases trigger larger thermal fluctuations at the interface that diminish the stable hydrogen-bonding network and, consequently, its favorable interaction with the bulk water molecules, which leads to less molecular adsorption and higher tension. Furthermore, the interfacial hydrogen bonding seems to be independent of the pressure of the system.

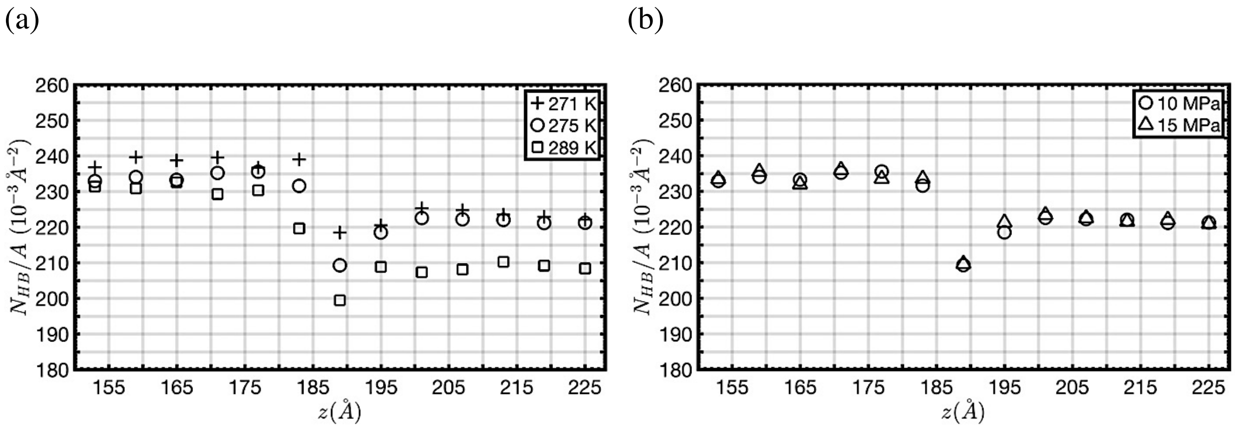

Figure 4.13. Hydrogen bond density profiles across the simulation box averaged over 1000 configurations at equilibrium at different system temperatures (a) and pressures (b). The interfacial center exists at z ≈ 184 Å with the liquid water phase on the left and the crystalline methane hydrate phase on the right side. In (a), the plus sign, circle, and square markers represent temperatures of 271, 275, and 289 K, respectively, at 10 MPa. In (b), the circle and triangle markers denote pressures of 10 and 15 MPa, respectively, at 275 K.

Finally, we characterize the interfacial polarization charge density to validate the interfacial tension results. Figure 4.14 clearly demonstrates that a temperature rise or a pressure drop penalizes the interfacial energy by decreasing the interface charge. This reverse proportionality is attributed to the negative electric charge contribution in the tangential pressure tensor component at the interface that has been previously reported [85-88]. The interfacial energy contribution of this unique property can be used to manipulate (i.e., inhibit or promote) the crystal nucleation and growth process via applying an external electric field [89-91].

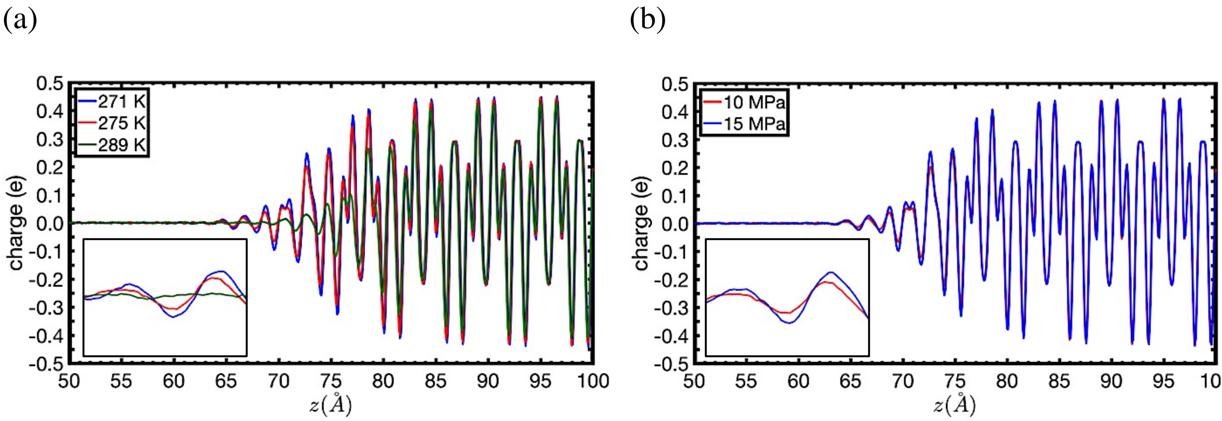

Figure 4.14. Interfacial charge distribution in units of electron charge at different temperatures (a) and pressures (b). The center of the interface is at z ≈ 66 Å with the water and hydrate phases on the left and right sides, respectively. The blue, red, and green lines in (a) denote the mixtures at 10 MPa and temperatures of 271, 275, and 289 K, respectively. The red and blue lines in (b) represent the mixtures at 275 K and pressures of 10 and 15 MPa, respectively. The charge density profiles are enlarged in the insets to better distinguish the lines.

4.7. Conclusions

In the present work, we used molecular dynamics as a computational technique to study the mixture of liquid water and methane hydrate crystal, particularly at the interface. We calculated the potential energy and local density profile of the system at different temperatures and pressures to seek the structure-property relations. The system anisotropy required the application of a novel NP_NAT ensemble and appropriate lattice parameter equal to the methane hydrate lattice parameter to provide an accurate platform for interfacial tension calculations for a nonplanar surface, as per the mechanical definition, in order to obtain the most reliable and comprehensive molecular-level information on this important interface. We accounted for a correction based on the Shuttleworth equation to look into the elastic strain contribution to the interfacial tension. The interfacial tension showed a slight increase with temperature increase or pressure decrease from 271 K and 30 MPa, respectively, until the melting point pertaining to the methane clathrate-water phase diagram. Such a strongly anomalous temperature effect on the interfacial tension defies the standard classical behavior.

In conjunction with the computational approach, we used direct numerical simulation techniques to validate the results on the basis of available experimental data. We investigated the excess enthalpy and entropy and concluded that the molecular orientation at the interface becomes less disordered as the temperature increases. Furthermore, a series of complex calculations on the adsorption, radial pair distribution function, hydrogen bonding density, and charge distribution at the interface generated a full molecular-level characterization and confirmed the interfacial tension variation trend with the system temperature and pressure.

As we increased the temperature or decreased the pressure, the interfacial polarization charge density, minimum number of hydrogen bonds, and intermolecular attractions further perturbed the force balance at the interface and led to the interfacial tension increase. Furthermore, the interfacial water became less disordered with lower molecular rotation in comparison to bulk water, which significantly dropped the water dielectric constant near the crystal surface and, subsequently, added to the interfacial tension.

In summary, the results reported provide a sound foundation for the characterization of the water and hydrate interfaces with respect to gas hydrate formation studies. Furthermore, the discussed methods can be extended to the interfacial energy calculations of many industrial, environmental, and biological processes, which deal with the water-crystal mixtures.

4.8. Acknowledgments

The authors are grateful for the financial support of the Natural Sciences and Engineering Research Council (NSERC), the McGill Engineering Doctoral Awards (MEDA), and the James McGill Professorship appointment. This research is also made possible by the technical and grant support from Compute Canada and Calcul Québec.

4.9. References

1. Sloan Jr, E.D. and C. Koh, *Clathrate hydrates of natural gases*. 2007: CRC press.
2. Jendi, Z.M., P. Servio, and A.D. Rey, *Ideal strength of methane hydrate and ice Ih from first-principles.* Crystal Growth & Design, 2015. **15**(11): p. 5301-5309.
3. Vlasic, T.M., P. Servio, and A.D. Rey, *Atomistic modeling of structure II gas hydrate mechanics: Compressibility and equations of state.* AIP Advances, 2016. **6**(8): p. 085317.
4. Vlasic, T.M., P.D. Servio, and A.D. Rey, *Effect of guest size on the mechanical properties and molecular structure of gas hydrates from first-principles.* Crystal Growth & Design, 2017. **17**(12): p. 6407-6416.

5. Carroll, J., *Natural gas hydrates: a guide for engineers*. 2014: Gulf Professional Publishing.

6. Demirbas, A., *Methane gas hydrate*. 2010: Springer Science & Business Media.

7. Klauda, J.B. and S.I. Sandler, *Global distribution of methane hydrate in ocean sediment.* Energy & Fuels, 2005. **19**(2): p. 459-470.

8. Bai, X.-M. and M. Li, *Test of classical nucleation theory via molecular-dynamics simulation.* The Journal of chemical physics, 2005. **122**(22): p. 224510.

9. Lupi, L., B. Peters, and V. Molinero, *Pre-ordering of interfacial water in the pathway of heterogeneous ice nucleation does not lead to a two-step crystallization mechanism.* The Journal of chemical physics, 2016. **145**(21): p. 211910.

10. Warrier, P., et al., *Overview: Nucleation of clathrate hydrates.* The Journal of chemical physics, 2016. **145**(21): p. 211705.

11. Knott, B.C., et al., *Homogeneous nucleation of methane hydrates: Unrealistic under realistic conditions.* Journal of the American Chemical Society, 2012. **134**(48): p. 19544-19547.

12. Sarupria, S. and P.G. Debenedetti, *Homogeneous nucleation of methane hydrate in microsecond molecular dynamics simulations.* The journal of physical chemistry letters, 2012. **3**(20): p. 2942-2947.

13. Kashchiev, D. and A. Firoozabadi, *Nucleation of gas hydrates.* Journal of Crystal Growth, 2002. **243**(3–4): p. 476-489.

14. Kashchiev, D., *Nucleation : basic theory with applications*. 2000, Butterworth Heinemann: Oxford ;.

15. Aman, Z.M. and C.A. Koh, *Interfacial phenomena in gas hydrate systems.* Chemical Society Reviews, 2016. **45**(6): p. 1678-1690.

16. Bagherzadeh, S.A., et al., *Influence of hydrated silica surfaces on interfacial water in the presence of clathrate hydrate forming gases.* The Journal of Physical Chemistry C, 2012. **116**(47): p. 24907-24915.

17. Bai, D., et al., *How properties of solid surfaces modulate the nucleation of gas hydrate.* Scientific Reports, 2015. **5**: p. 12747.

18. Liang, S. and P.G. Kusalik, *The nucleation of gas hydrates near silica surfaces.* Canadian Journal of Chemistry, 2014. **93**(8): p. 791-798.

19. Sloan, E.D., *Fundamental principles and applications of natural gas hydrates.* Nature, 2003. **426**(6964): p. 353-363.

20. Khadem, S.A. and R.B. Boozarjomehry, *Development of systematic framework for an intelligent decision support system in gas transmission network.* Industrial & Engineering Chemistry Research, 2015. **54**(43): p. 10768-10786.

21. Faramawy, S., T. Zaki, and A.-E. Sakr, *Natural gas origin, composition, and processing: A review.* Journal of Natural Gas Science and Engineering, 2016. **34**: p. 34-54.

22. Koh, C.A., et al., *Fundamentals and applications of gas hydrates.* 2011.

23. Osborn, S.G., et al., *Methane contamination of drinking water accompanying gas-well drilling and hydraulic fracturing.* proceedings of the National Academy of Sciences, 2011. **108**(20): p. 8172-8176.

24. Harriss, R.C., et al., *Sources of atmospheric methane in the south Florida environment.* Global Biogeochemical Cycles, 1988. **2**(3): p. 231-243.

25. Khadem, S.A., et al., *Pressure and temperature functionality of paraffin-carbon dioxide interfacial tension using genetic programming and dimension analysis (GPDA) method.* Journal of Natural Gas Science and Engineering, 2014. **20**: p. 407-413.

26. Busch, A. and A. Amann-Hildenbrand, *Predicting capillarity of mudrocks.* Marine and petroleum geology, 2013. **45**: p. 208-223.

27. Nourbakhsh, A., *Determination of capillary pressure, relative permeability and pores size distribution characteristics of coal from Sydney basin-Canada.* 2012.

28. Binks, B.P. and J.H. Clint, *Solid wettability from surface energy components: relevance to pickering emulsions.* Langmuir, 2002. **18**(4): p. 1270-1273.

29. Vázquez, U.O.M., et al., *Calculating the surface tension between a flat solid and a liquid: a theoretical and computer simulation study of three topologically different methods.* Journal of Mathematical Chemistry, 2009. **45**(1): p. 161-174.

30. Chaplin, M., *Theory vs experiment: what is the surface charge of water?* Water Journal Multidisciplinary Research Journal 1, 2009: p. 1-28.

31. Eisenberg, D., D.S. Eisenberg, and W. Kauzmann, *The structure and properties of water*. 2005: Oxford University Press on Demand.

32. Biscay, F., et al., *Monte Carlo simulations of the pressure dependence of the water− acid gas interfacial tensions.* The Journal of Physical Chemistry B, 2009. **113**(43): p. 14277-14290.

33. Biscay, F., et al., *Monte Carlo calculation of the methane-water interfacial tension at high pressures.* The Journal of chemical physics, 2009. **131**(12): p. 124707.

34. Ikeguchi, M., *Partial rigid-body dynamics in NPT, NPAT and NPγT ensembles for proteins and membranes.* Journal of computational chemistry, 2004. **25**(4): p. 529-541.

35. Noya, E.G., C. Vega, and E. de Miguel, *Determination of the melting point of hard spheres from direct coexistence simulation methods.* The Journal of chemical physics, 2008. **128**(15): p. 154507.

36. Kvamme, B., T. Kuznetsova, and K. Schmidt. *Experimental measurements and numerical modelling of interfacial tension in water-methane systems*. in *Presentation at the International Conference of Computational Methods in Sciences and Engineering, Chania, Greece*. 2006.

37. Schmidt, K.A., G.K. Folas, and B. Kvamme, *Calculation of the interfacial tension of the methane–water system with the linear gradient theory.* Fluid Phase Equilibria, 2007. **261**(1): p. 230-237.

38. Kirkwood, J.G. and F.P. Buff, *The statistical mechanical theory of surface tension.* The Journal of Chemical Physics, 1949. **17**(3): p. 338-343.

39. Bahadur, R. and L.M. Russell, *Effect of surface tension from MD simulations on size-dependent deliquescence of NaCl nanoparticles.* Aerosol Science and Technology, 2008. **42**(5): p. 369-376.

40. Ghoufi, A. and P. Malfreyt, *Calculation of the surface tension and pressure components from a non-exponential perturbation method of the thermodynamic route.* The Journal of chemical physics, 2012. **136**(2): p. 024104.

41. Nair, A.R. and S.P. Sathian, *A molecular dynamics study to determine the solid-liquid interfacial tension using test area simulation method (TASM).* The Journal of Chemical Physics, 2012. **137**(8): p. 084702.

42. Butt, H.-J.r., K. Graf, and M. Kappl, *Physics and chemistry of interfaces*. 2nd, rev. and enl. ed. ed. Physics textbook. 2006, Weinheim: Wiley-VCH.

43. Erbil, H.Y., *Surface chemistry of solid and liquid interfaces*. 2006, Oxford, UK ;: Blackwell Pub.

44. Ibach, H., *Physics of surfaces and interfaces*. 2006, Springer: Berlin ;.

45. Soustelle, M., *Thermodynamics of surfaces and capillary systems*. 2016, ISTE, Ltd. ;
John Wiley & Sons: London, UK; Hoboken, NJ.

46. Bico, J., É. Reyssat, and B. Roman, *Elastocapillarity: When surface tension deforms elastic solids.* Annual Review of Fluid Mechanics, 2018. **50**: p. 629-659.

47. Qi, X., T. Balankura, and K.A. Fichthorn, *Theoretical Perspectives on the Influence of Solution-Phase Additives in Shape-Controlled Nanocrystal Synthesis.* The Journal of Physical Chemistry C, 2018. **122**(33): p. 18785-18794.

48. Hecquet, P., *Surface energy and surface stress on vicinals by revisiting the Shuttleworth relation.* Surface Science, 2018. **670**: p. 58-67.

49. Lee, J.-Y., et al., *The surface energy and stress of metals.* Surface Science, 2018. **674**: p. 51-68.

50. Xu, Q., R.W. Style, and E.R. Dufresne, *Surface elastic constants of a soft solid.* Soft matter, 2018. **14**(6): p. 916-920.

51. Shuttleworth, R., *The surface tension of solids.* Proceedings of the physical society. Section A, 1950. **63**(5): p. 444.

52. Tolman, R.C., *Consideration of the Gibbs theory of surface tension.* The journal of chemical physics, 1948. **16**(8): p. 758-774.

53. Plimpton, S., *Fast parallel algorithms for short-range molecular dynamics.* Journal of computational physics, 1995. **117**(1): p. 1-19.

54. Jorgensen, W.L., J.D. Madura, and C.J. Swenson, *Optimized intermolecular potential functions for liquid hydrocarbons.* Journal of the American Chemical Society, 1984. **106**(22): p. 6638-6646.

55. Horn, H.W., et al., *Development of an improved four-site water model for biomolecular simulations: TIP4P-Ew.* The Journal of chemical physics, 2004. **120**(20): p. 9665-9678.

56. Hockney, R.W. and J.W. Eastwood, *Computer simulation using particles*. 1988: crc Press.

57. Isele-Holder, R.E., W. Mitchell, and A.E. Ismail, *Development and application of a particle-particle particle-mesh Ewald method for dispersion interactions.* The Journal of chemical physics, 2012. **137**(17): p. 174107.

58. Ghiass, M. and A.D. Rey, *Interfacial thermodynamics of compressible polymer solutions*. 2008, AIP.

59. Rowlinson, J.S. and B. Widom, *Molecular theory of capillarity*. 2013: Courier Corporation.

60. Blokhuis, E., et al., *Tail corrections to the surface tension of a Lennard-Jones liquid-vapour interface.* Molecular Physics, 1995. **85**(3): p. 665-669.

61. Chapela, G.A., et al., *Computer simulation of a gas–liquid surface. Part 1.* Journal of the Chemical Society, Faraday Transactions 2: Molecular and Chemical Physics, 1977. **73**(7): p. 1133-1144.

62. Grest, G.S., et al., *Substructured multibody molecular dynamics*. 2006, Sandia National Laboratories.

63. Jendi, Z.M., A.D. Rey, and P. Servio, *Ab initio DFT study of structural and mechanical properties of methane and carbon dioxide hydrates.* Molecular Simulation, 2015. **41**(7): p. 572-579.

64. Mirzaeifard, S., P. Servio, and A.D. Rey, *Molecular dynamics characterization of temperature and pressure effects on the water-methane interface.* Colloid and Interface Science Communications, 2018. **24**: p. 75-81.

65. Sachs, W. and V. Meyn, *Pressure and temperature dependence of the surface tension in the system natural gas/water principles of investigation and the first precise experimental data for pure methane/water at 25°C up to 46.8 MPa.* Colloids and Surfaces A: Physicochemical and Engineering Aspects, 1995. **94**(2): p. 291-301.

66. Sakamaki, R., et al., *Thermodynamic properties of methane/water interface predicted by molecular dynamics simulations.* The Journal of chemical physics, 2011. **134**(14): p. 144702.

67. Cammarata, R.C. and K. Sieradzki, *Surface and interface stresses.* Annual Review of Materials Science, 1994. **24**(1): p. 215-234.

68. Ambler, M., et al., *Solid–liquid interfacial free energy of ice Ih, ice Ic, and ice 0 within a mono-atomic model of water via the capillary wave method.* The Journal of chemical physics, 2017. **146**(7): p. 074701.

69. Gránásy, L., T. Pusztai, and P.F. James, *Interfacial properties deduced from nucleation experiments: A Cahn–Hilliard analysis.* The Journal of chemical physics, 2002. **117**(13): p. 6157-6168.

70. Koop, T. and B.J. Murray, *A physically constrained classical description of the homogeneous nucleation of ice in water.* The Journal of chemical physics, 2016. **145**(21): p. 211915.

71. Němec, T., *Estimation of ice–water interfacial energy based on pressure-dependent formulation of classical nucleation theory.* Chemical Physics Letters, 2013. **583**: p. 64-68.

72. Wood, G. and A. Walton, *Homogeneous nucleation kinetics of ice from water.* Journal of Applied Physics, 1970. **41**(7): p. 3027-3036.

73. Zhang, Y. and J. Khodadadi, *Ice-water interfacial energy between 235.35 and 237.15 K deduced from homogeneous nucleation rate.* Current Applied Physics, 2016. **16**(5): p. 534-538.

74. Chandrasekhar, S., *Liquid Crystals*. 2nd ed. 1992: Cambridge University Press. 80-84.

75. Rey, A.D., *Modeling the Wilhelmy surface tension method for nematic liquid crystals.* Langmuir, 2000. **16**(2): p. 845-849.

76. Naeiji, P., F. Varaminian, and M. Rahmati, *Comparison of the thermodynamic, structural and dynamical properties of methane/water and methane/water/hydrate systems using molecular dynamic simulations.* Journal of Natural Gas Science and Engineering, 2017. **44**: p. 122-130.

77. Jacobson, L.C. and V. Molinero, *Can amorphous nuclei grow crystalline clathrates? The size and crystallinity of critical clathrate nuclei.* Journal of the American Chemical Society, 2011. **133**(16): p. 6458-6463.

78. Anderson, R., et al., *Experimental measurement of methane and carbon dioxide clathrate hydrate equilibria in mesoporous silica.* The Journal of Physical Chemistry B, 2003. **107**(15): p. 3507-3514.

79. Uchida, T., et al., *Effects of pore sizes on dissociation temperatures and pressures of methane, carbon dioxide, and propane hydrates in porous media.* The journal of physical chemistry B, 2002. **106**(4): p. 820-826.

80. Frolov, T. and Y. Mishin, *Temperature dependence of the surface free energy and surface stress: An atomistic calculation for Cu (110).* Physical Review B, 2009. **79**(4): p. 045430.

81. Fumagalli, L., et al., *Anomalously low dielectric constant of confined water.* Science, 2018. **360**(6395): p. 1339-1342.

82. Holmes, C.F., *Relation between surface tension and dielectric constant.* Journal of the American Chemical Society, 1973. **95**(4): p. 1014-1016.

83. Takeuchi, T., *Surface Tension and Dielectric Constant.* Proceedings of the Physico-Mathematical Society of Japan. 3rd Series, 1920. **2**(8): p. 192-194.

84. Mirzaeifard, S., P. Servio, and A.D. Rey, *Molecular Dynamics Characterization of the Water-Methane, Ethane, and Propane Gas Mixture Interfaces.* Chemical Engineering Science, 2019.

85. Goodisman, J., *Surface tension of a charged and polarized system.* The Journal of Physical Chemistry, 1992. **96**(15): p. 6355-6360.

86. Jiménez-Ángeles, F. and A. Firoozabadi, *Induced charge density and thin liquid film at hydrate/methane gas interfaces.* The Journal of Physical Chemistry C, 2014. **118**(45): p. 26041-26048.

87. Kunieda, M., et al., *Self-accumulation of aromatics at the oil− water interface through weak hydrogen bonding.* Journal of the American Chemical Society, 2010. **132**(51): p. 18281-18286.

88. Song, J. and M.W. Kim, *Excess Charge Density and its Relationship with Surface Tension Increment at the Air− Electrolyte Solution Interface.* The Journal of Physical Chemistry B, 2011. **115**(8): p. 1856-1862.

89. Luis, D., E. Herrera-Hernández, and H. Saint-Martin, *A theoretical study of the dissociation of the sI methane hydrate induced by an external electric field.* The Journal of chemical physics, 2015. **143**(20): p. 204503.

90. Yan, J. and G. Patey, *Heterogeneous ice nucleation induced by electric fields.* The Journal of Physical Chemistry Letters, 2011. **2**(20): p. 2555-2559.

91. Yan, J. and G. Patey, *Ice nucleation by electric surface fields of varying range and geometry.* The Journal of chemical physics, 2013. **139**(14): p. 144501.

92. Adamson, A.W. and A.P. Gast, *Physical chemistry of surfaces*. Vol. 15.

Chapter 5. Characterization of Nucleation of Methane Hydrate Crystals: Interfacial Theory and Molecular Simulation

Chapter 5: Characterization of Nucleation of Methane Hydrate Crystals: Interfacial Theory and Molecular Simulation

5.1. Preface

The methane hydrate formation is studied over a range of pressure and temperature to better understand the effect of supersaturation and interfacial energy contribution in the formation process. Different types of interfaces formed between gas-liquid, gas-hydrate, and hydrate-liquid must be considered for the most sensible conclusions. Gas-hydrate interfaces may not follow classical thermodynamic rules, which are investigated. This chapter is reproduced with permission from “Mirzaeifard, S., P. Servio, and A.D. Rey, Characterization of nucleation of methane hydrate crystals: interfacial theory and molecular simulation. Colloid and Interface Science, 2019. 557: p. 556-567”.

5.2. Abstract

Hypothesis: solutions of water and methane gas at favorable thermodynamic conditions lead to the formation of crystalline methane hydrates. In natural and industrial environments, the nucleation process might occur in the solution’s bulk or at the solid-liquid and liquid-gas interfaces, which evolve into distinct morphologies. A complete molecular level understanding and material characterization of preferred nucleation sites and morphologies is required to inhibit or promote crystallization, as required.

Methodology: computational simulations are utilized in this work in combination with analytical theory to calculate the supersaturation and interfacial tension as the driving force and suppressor, respectively, in the hydrate crystal formation process. We employ accurate molecular dynamics (MD) techniques to obtain critical thermodynamic and mechanical properties, and subsequently, analyze the formation using the classical nucleation theory (CNT).

Findings: we report the interfacial tension at all possible interfaces in water-methane gas solutions. We apply both our direct numerical simulation method and Antonow’s rule to find the tension at the methane hydrate and gas interface, and importantly conclude that Antonow’s rule overestimates the values. We calculate the work of formation and nucleation rate of the methane hydrate with and without additives. The nucleation probabilistically forms in the ranked order of film-shaped, cap-shaped, lens-shaped, and homogeneous. We postulate that the premelting of hydrate crystals at the hydrate-gas interface creates an intermediate quasi-liquid layer, which works in favor of the lens-shaped formation compared to homogeneous cases. However, the subtle

difference in surface energy indicates high concentration of water and gas molecules at the interface is the main reason behind lens-shaped clustering. We lastly show that ice properties cannot be used to approximate the hydrate formation work.

5.3. Keywords

Methane hydrate; Surface physics; Interfacial tension; Classical nucleation theory; Computational thermodynamics; Molecular dynamics simulation.

5.4. Introduction

At low temperature and high pressure, liquid water molecules form hydrogen bonded networks that create polyhedral cages, which can encapsulate guest gas molecules such as methane, ethane, and propane so that a new phase of ice-like crystals forms above 0 ºC, known as gas hydrate or clathrate [1]. Depending on the guest gas molecules, the hydrates can form different crystalline structures including structure I [2], structure II [3, 4], and structure H [5]. Gas hydrates have a wide range of industrial applications. They play a very important role in flow assurance (i.e., management of fluid transportation in multiphase flow) as the pipelines are mostly in deep oceans that provide favorable thermodynamic conditions for gas hydrates formation, which consequently causes explosions or blockage inside the pipelines and equipment [6, 7]. The blockage can be extremely costly as it is usually followed by a shutdown in the entire oil and gas processing plants that might take days or weeks to be resolved. Unfortunately, the current techniques that are being used to avoid the blockage are also environmentally damaging. In addition to flow assurance, hydrates can be considered a vastly available clean resource of energy, and also transportation medium for other materials as one volume of gas hydrate contains 164 volumes of gas at standard temperature and pressure condition [1]. Moreover, self-preservation is a unique and poorly understood characteristic of gas hydrates that increases and prolongs its stability, which is desirable for gas storage applications [8].

Methane hydrates are the most common hydrates formed naturally by biogenic methane in marine and under permafrost sediments. These naturally occurring hydrates hold two to three orders of magnitude the amount of energy when compared to global fossil fuels and natural gas reserves, respectively [6-11]. On the other hand, the ubiquitous methane hydrate could be a significant contributor to global warming if methane is released and migrates to the ocean's surfaces. Hence, the significance of methane hydrates in environmental processes has been subjected to intense research [9]. In summary, we seek to understand the methane hydrate formation process in order to eventually find green and robust methods to inhibit or promote these clathrates, depending on the application.

The fundamental thermodynamic conditions to ignite the formation process are high pressure (> 0.6 MPa), low temperature (< 323 K), the presence of guest molecules as the hydrate former, and sufficient amount of water [8, 12]. Additional conditions such as turbulence or agitation, presence of nucleation sites, and additional water molecules might enhance the formation rate [5]. Due to the availability of all these essential parameters in some environments like gas pipelines, the formation probability is substantial. This formation phenomenon includes nucleation and growth processes as the onset of hydrate plugging in flow assurance that has been studied for years, however, there is so much yet to comprehend [13-15].

The thermodynamic temperature and pressure condition for hydrate formation must be in the region of hydrate stability. In general, for a pair of solute-solvent, there exists a relationship for concentration and temperature that defines the metastable limit. This relationship is known as the thermodynamic spinodal and represents the supersaturation limit. However, the formation of metastable hydrates is challenged due to high entropy conditions until the cluster agglomerate reaches a critical crystal nucleus size for steady growth [1]. Supersaturated systems can create a new phase either in the bulk (homogenous) or onto the surface in contact with the bulk (heterogeneous). Depending on the location of the contact interface, heterogeneous nucleation can be further categorized into three models: lens-shaped (gas-liquid), film-shaped (gas-liquid), and cap-shaped (solid-liquid). Figure 5.1 shows a schematic diagram of these formation mechanisms.

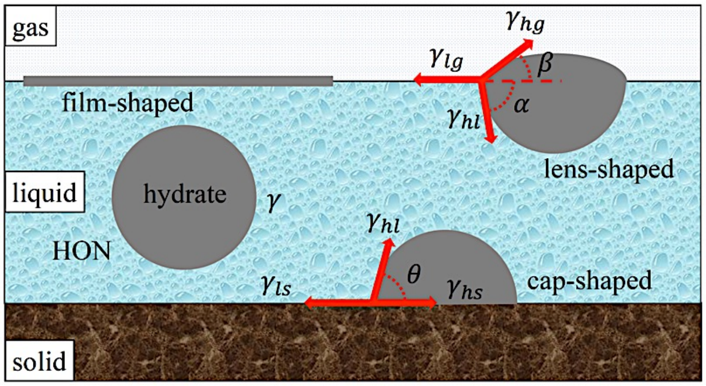

Figure 5.1. Schematics of different hydrate formation morphologies. γ represents the interfacial tension for the homogeneous (HON) formation of methane gas hydrate. γ_{lg}, γ_{hl}, γ_{hg}, γ_{ls}, and γ_{hs} indicate the interfacial tension at the liquid-gas, hydrate-liquid, hydrate-gas, liquid-solid, and hydrate-solid interfaces, respectively.

Among all the theories in crystallography, the classical nucleation theory (CNT) is still the foundation of most state-of-the-art nucleation models, which fruitfully describes the gas hydrate or ice formation work [1, 16-18]. According to the CNT, this work equals a spontaneous formation of a new hydrate cluster consisting of n crystal unit cells associated with an interfacial energy cost [19]. This formation work $W(n)$ is given by:

$$W(n) = -n\Delta\mu + c(nv_h)^{\frac{2}{3}}\gamma \tag{5.1}$$

where $\Delta\mu$ (J) measures the supersaturation (i.e., difference in chemical potentials) as a function of pressure and temperature, c is a shape factor, v_h (m^3) is the volume of a hydrate building unit, and γ ($\mathrm{J/m}^2$) accounts for the interfacial energy.

5.4.1. Motivation

It has been assumed that the interfacial boundaries between different phases dictate the ideal mechanism and location for clathrate formation [19, 20], but the accuracy of this assumption needs to be critically examined. It is known that the formation of hydrate crystals, irrespective of the hydrate promoters and system pressure [21], mainly depends on the nucleation period, which is influenced by the driving forces and interfacial energy [20, 22, 23], but the molecular-level understanding of these contributions remains incomplete.

In particular, the characterization of interfacial tensions at water-methane hydrate, water-methane gas, and methane hydrate-methane gas interfaces in the range of 271-289 K and 5-15 MPa, which is the methane hydrate stability and formation region [11], is essentially missing or very limited. More specifically, to obtain the interfacial tension between methane gas and liquid phases, the Antonow's (Antonoff's) rule has been proposed [19], while the reliability of such classical thermodynamic relation in complex crystalline hydrate surfaces is very uncertain. This substantial lack of information on the interfacial tension, as well as supersaturation data, generate significant questions in our understanding of hydrate formation process: Is it homogeneous [24-26], cap-shaped [27-30], or lens-shaped [30, 31]? In the case of lens-shaped morphology, it is also unclear what causes this type of formation. This can be due to the role of interface in the Gibbs free energy of nucleation or simply higher concentrations of both water and methane molecules at the water-gas interface. Nonetheless, the water mole fraction in bulk gas and gas mole fraction in aqueous phase are less than 0.05 and 0.001, respectively [1], which impedes the homogeneous formation, however, previous works reported the possibility of such formation process [25, 32-35].

In the case of full occupancy of hydrate cages, 85 mol% of the crystal hydrate is still made of water molecules [12], which may result in similar physical and thermodynamic behaviors for ice and methane hydrate. Therefore, some researchers suggested the use of ice properties to circumvent the need of critically important hydrate data [19, 36, 37]. Despite many ice-hydrate analogies, some properties such as mechanical strength, heat capacity, and thermal conductivity are different [6-8]. Therefore, we need to investigate the possibility of using ice parameters in hydrate formation studies to ensure accurate results and conclusions.

Hence, the leading motivation of this work is to characterize the supersaturation and interfacial energy contributions in the nucleation process of methane gas hydrates, and subsequently, reveal the theoretical physics behind the most probable formation process in order to promote or suppress it subject to the above-mentioned technological applications. To the best of our knowledge, this is the first work that attempts to simultaneously study the water-gas, water-hydrate, and hydrate-gas mixtures to answer all these crucial questions in hydrate science. Furthermore, based on the interfacial characterization, we deduce features of the homogeneous and heterogeneous nucleation of methane hydrates.

The organization of this paper is as follows. In the next section, we briefly describe the computational methodology and models, MD computer simulations, and analytical theory, which include a novel approach for the calculation of supersaturation and interfacial tension at the liquid-gas, hydrate-liquid, and hydrate-gas interfaces. In the results and discussion section, we calculate and analyze the interfacial tension, supersaturation, hydrate formation work, and crystal nucleation rate at different pressure and temperature. In addition, we investigate the effect of additives in the water-methane solution. We also evaluate substituting hydrate parameters with ice when the interfacial tension is unknown. Lastly, we articulate the main conclusions, significance, and novelty of this work.

5.5. Methodology

The nature of interfacial interactions and thermodynamic stability is of great significance to investigate the phase transitions, nucleation, morphology, and nucleation rate of gas hydrates, which demands modern experimental methods, theoretical modeling, or computational characterization [20, 38-42].

Clathrate hydrate formation is a nanoscale, rapid, and stochastic process, while the performed experiments cannot resolve these key characteristics [13]. In addition, the experimental characterization may be inaccurate owing to the sample impurities and absence of necessary molecular-level measurements, and furthermore, it is relatively complex and expensive to provide the crucial thermodynamic conditions (high pressure and low temperature), specifically in cases of the predominant natural gas hydrates in pipelines [43, 44]. Some of the current theoretical work has also not fully explained the hydrate formation owing to assumptions that will be explained later in this paper. In this work, we show that a combination of analytical theory and computational simulations can elucidate the thermodynamic and kinetic aspects of hydrate formation in both microscopic and macroscopic scales. Therefore, we attempt to accurately model clathrate hydrates to find more insights regarding the supersaturation and interfacial energy contributions in nucleation and growth processes. We use molecular dynamic (MD) techniques in conjunction with interfacial thermodynamics to quantitatively and qualitatively explore the formation work, nucleation rate, and equilibrium configurations. Nevertheless, molecular simulations of different mixtures including liquid, gas, and solid crystals encounter other challenges to obtain reliable results. For instance, robust hydrogen and ion bonding, discontinuity of macroscopic fields, sudden local density variation, interfacial elastic deformation, topological disturbance, spontaneous interfacial expansion or contraction, and sufficient length and time scales. The key aspect of our approach is to employ appropriate methods to overcome these issues by tailoring realistic models [45, 46].

5.5.1. Model

In this study, we follow the standard procedure to create the different possible mixtures of interest: water-gas, water-hydrate, and hydrate-gas [47, 48]. In a 48×48×200 Å three-dimensional simulation box with periodic boundary conditions, we surround one phase with another phase at each side in order to construct three distinct interfaces of the water-methane hydrate, water-methane gas, and methane hydrate-methane gas (see Figure 5.2). Table 5.1 reports the number of molecules located in the initial configuration for each set of simulations. The hydrate crystal phase contains water and methane molecules with 100% cage occupancy. We adopt initial Cartesian coordinates of the methane hydrate unit cell at the lowest energy configuration and zero dipole moment based on the X-ray diffraction analysis [49] and high-resolution neutron diffraction experiments [50].

We choose such phase-by-phase breakdown as an alternative to the regular three-phase system [51] to ensure more accurate results of the interfacial tension. This approach is of great importance for the hydrate surfaces since the interfacial elastic deformation differentiates the surface free energy and surface tension [52, 53], which demands distinct simulation and computation methods, not applied for liquid-gas interfaces. Moreover, this method creates two interfaces between each couple of phases, which allows us to average over two values obtained from both interfaces to increase the accuracy. The choice of pressure and temperature in this study is based on a region of phase diagram so that all three phases can coexist to guarantee equilibrium states for all the binary mixtures [1, 11].

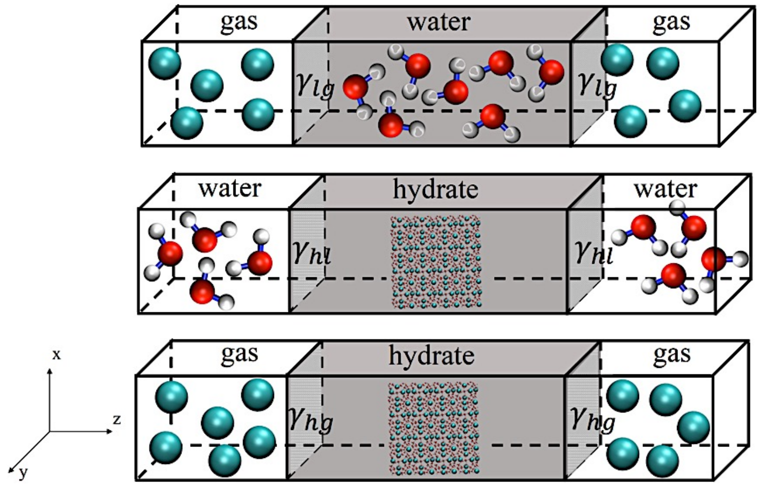

Figure 5.2. Schematic showing the simulation template including the methane gas, water, and methane hydrate molecules to represent the gas, liquid, and hydrate phases, respectively. The red, white, and green particles denote the oxygen and hydrogen atoms, and methane molecules, respectively.

Table 5.1. Number of molecules for the initial configuration

mixtures	phases			
	gas	liquid	hydrate	
gas-water	1,328 CH_4	13,104 H_2O	-	
water-hydrate	-	5,468 H_2O	1,328 CH_4	7,636 H_2O
gas-hydrate	660 CH_4	-	1,016 CH_4	5,842 H_2O

In this work, we use the united atom optimized potentials for liquid simulations (OPLS-UA) [54] and transferable intermolecular potential with the four points (TIP4P) models [55] to create force fields for the methane and water molecules, respectively, employing the LAMMPS software [56]. We choose TIP4P as opposed to other water models, such as SPC/E, TIP3P, and TIP5P, which is more compatible with mixtures of water and hydrophobic solutes [57-59]. To include the Coulombic electrostatic interactions, we execute the TIP4P-optimized particle-particle particle-mesh (PPPM) package with an accuracy of 10^{-5} for the force computation following the introduced approach by Hockney and Eastwood [60, 61]. In addition, the Lennard-Jones (LJ) potential with Lorentz-Berthelot mixing rule is used to implement the intermolecular interactions:

$$U_{LJ}(r) = 4\varepsilon\left[\left(\frac{\sigma}{r}\right)^{12} - \left(\frac{\sigma}{r}\right)^{6}\right] \tag{5.2}$$

$$\varepsilon_{ij} = \sqrt{\varepsilon_{ii}\varepsilon_{jj}}\ ,\ \sigma_{ij} = \frac{\sigma_{ii}+\sigma_{jj}}{2} \tag{5.3}$$

where ε, σ, and r denote the well depth, finite distance at zero potential, and particles distance, respectively, as reported in Table 5.2 [54, 55]. We choose a cut-off distance of 12 Å for both Coulombic electrostatic and LJ interactions. We also constrain the bond lengths and angles integrated in the water molecules by means of the Shake algorithm to avoid any substantial variation throughout the simulations.

Table 5.2. Simulation parameters including the molecular and structural properties of the water and methane molecules

	mass (g/mol)	σ (Å)	ε (kcal/mol)	charge (e)
CH_4	16.042	3.733	0.294	0
O	15.999	3.164	0.163	-1.0484
H	1.0080	0	0	0.5242
H-O-H angle		104.52°		
O-H bond length		0.9572 Å		
O···M distance		0.125 Å		

5.5.2. Simulation

We apply the Verlet algorithm with a time step of 2 fs to incorporate the non-Hamiltonian equations of motion. Accordingly, Nosé-Hoover thermostat and Parrinello-Rahman barostat adjust the pressure and temperature with 4 ps damping constant for the characteristic fluctuations. We sample the system configurations using the isothermal-isobaric (*NPT*) and isothermal-isobaric-isointerface area (NP_NAT) ensembles. The novel and effective NP_NAT ensemble, which requires constant normal pressure (P_N) and cross-sectional area (A) can precisely capture interfacial phenomena under different temperature and pressure regimes. The NP_NAT ensemble controls the normal pressure in the z direction (P_{zz}) by the barostat. The system volume, and subsequently, the densities of coexisting-components can change towards equilibration to attain a desired target pressure. The ensemble also holds constant the surface area by fixing the simulation box length in both x (L_x) and y (L_y) directions (i.e., $A_S = L_xL_y$) with independent contraction or dilation in only the z dimension. The box length in the z direction (L_z) freely fluctuates to adjust the system volume for the prescribed bulk density of each phase so that the knowledge on the initial value of L_z is not necessary.

We start the simulations with an initial configuration, and run for 300 ns under the standard *NPT* ensemble to attain equilibrium and appropriate lattice parameters for cases with a hydrate phase. We continue to perform the MD simulations for further 10 ns until the thermodynamic equilibrium is guaranteed by the correlation factor calculations on thermodynamic and mechanical properties, namely, potential energy, temperature, and local densities of water and methane molecules. Thenceforth, we interchangeably employ the adaptive NP_NAT and *NPT* ensembles throughout the simulations following the method fully descried in our previous work [62] to collect the required data throughout 5 ns of MD simulation. We only analyze and report the information obtained from the last nanosecond to ensure the most accurate results.

5.5.3. Analytical Theory

According to Eqn. 5.1, any analysis on the formation work demands the calculation of the supersaturation and interfacial tension contributions. Supersaturation of an isothermal and isobaric regimes is calculated from the following equation [19]:

$$\Delta\mu_{isothermal} = k_BT\, ln\left[\frac{\varphi(P,T)P}{\varphi(P_e,T)P_e}\right] + (n_w v_w - v_h)(P - P_e) \qquad (5.4)$$

where k_B, T, n_w, v_w, P, and P_e are the Boltzmann constant, system temperature, stoichiometric hydration number defined as the ratio of the number of water to gas molecules (5.75, for methane hydrate [19]), which is a function of formation condition [9], volume of water molecules in the solution (≈ 0.03 nm^3 [19]), system pressure, and equilibrium pressure, respectively. We choose pressure and temperature close to their equilibrium values and Peng-Robinson equation of state to obtain the fugacity coefficient (φ) [63].

We employ the standard mechanical definition devised by Bakker *et al.* [64, 65] to compute the interfacial tension (γ_B). In addition, a method for the tail or long range correction developed by Blokhuis *et al.* [66] is included to compensate the truncation error triggered by applying a cut-off distance in the interatomic interactions [66-68]. In cases involving the crystalline hydrate phase, implementation of the Shuttleworth equation is also required to account for the elastic deformation of the solid surface [52, 69]. To account for this deformation requires the sequential use of the *NPT* and *NP$_N$AT* ensembles to attain sensible results as completely described in our preceding work [62]. The total interfacial tension is given by:

$$\gamma = \overbrace{\frac{1}{2}\int_{-\infty}^{+\infty}\left(P_{zz}-\left(\frac{P_{xx}+P_{yy}}{2}\right)\right)dz}^{\gamma_B} + \overbrace{\int_0^1\int_{r_c}^{\infty}12\pi\varepsilon\sigma^6\Delta\rho_{ij}{}^2\left(\frac{3s^3-s}{r^3}\right)cot\left(\frac{rs}{t}\right)dsdr}^{\gamma_{tail}}$$

$$+\overbrace{A_s\frac{\partial(\gamma_B+\gamma_{tail})}{\partial A_s}}^{\gamma_e} \quad (5.5)$$

where P_{zz} and $(P_{xx}+P_{yy})/2$, r_c, t, s, $\Delta\rho_{ij}$, and A_S represent the normal pressure, tangential pressure, cut-off distance, interfacial thickness, position, molecular density difference between the i and j phases, and the cross-sectional area, respectively.

It should be noted that γ is equal to the surface energy of methane hydrate-liquid interface (γ_{hl}) for the case of homogenous nucleation as shown in Figure 5.1. γ for heterogeneous nucleation (HEN), which might occur at the interface of liquid-solid (cap-shaped) or liquid-gas (lens-shaped), is lower than γ_{hl} obeying the following relationship [19]:

$$\gamma = \Psi\gamma_{hl} \quad (5.6)$$

where Ψ is in a range of 0-1 to characterize different shapes of heterogeneous nucleation. For cap-shaped clusters, Ψ can be calculated from [19]:

$$\Psi_{cap-shaped} = \left[\frac{(2+cos\,\theta)(1-cos\,\theta)^2}{4}\right]^{\frac{1}{3}} \quad (5.7)$$

where θ is called the wetting angle of hydrate-solid interface. This angle can range from 0 (complete wetting) to 180° (no wetting, which is HON). The Young equation relates θ to the surface energies of the liquid-solid (γ_{ls}) and hydrate-solid (γ_{hs}) interfaces by the following equation [37]:

$$\cos\theta = \frac{(\gamma_{ls}-\gamma_{hs})}{\gamma_{hl}} \quad (5.8)$$

Since the interaction with a solid substrate is not the scope of this work, we simply assign two candidates for the θ: 60º as an acute angle and 120º as an obtuse angle. Figure 5.3 shows how the wetting angle alters the interfacial energy contribution via the parameter Ψ.

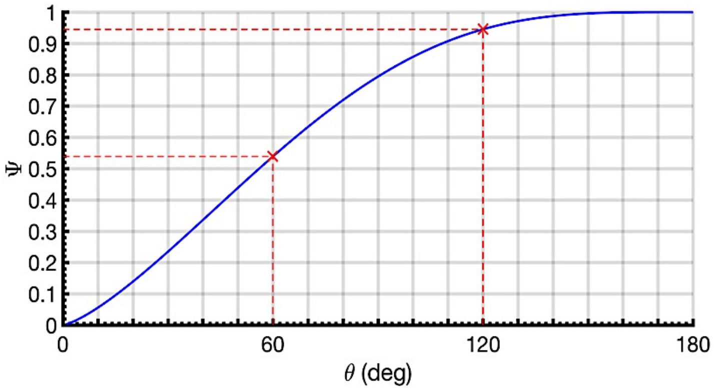

Figure 5.3. Characterization factor versus wetting angle with values between 0 to 180° for cap-shaped clusters.

For lens-shaped clusters, Ψ is [19]:

$$\Psi_{lens-shaped} = \left[\frac{(2+\cos\alpha)(1-\cos\alpha)^2+(2+\cos\beta)(1-\cos\beta)^2\left(\frac{\sin\alpha}{\sin\beta}\right)^3}{4}\right]^{\frac{1}{3}} \tag{5.9}$$

similarly, α and β are related to the surface energies of the liquid-gas (γ_{lg}) and hydrate-gas (γ_{hg}) interfaces by the following expressions [19]:

$$\cos\alpha = \frac{\left(\gamma_{lg}^2+\gamma_{hl}{}^2-\gamma_{hg}^2\right)}{2\gamma_{lg}\gamma_{hl}}, \cos\beta = \frac{\left(\gamma_{lg}^2-\gamma_{hl}{}^2+\gamma_{hg}^2\right)}{2\gamma_{lg}\gamma_{hg}} \tag{5.10}$$

According to Eqn. 5.9, $\Psi_{lens-shaped}$ is zero when α and β are infinitesimal, which eliminates the interfacial energy contribution from Eqn. 5.1. Such scenario effectively reveals the limit of lens-shaped formation denoted as film-shaped nucleation to seek insights when only spontaneous nucleation occurs in order to highlight the role of interfacial energy in hydrate formation work. Please note that the direct assignment of α and β is not necessary. These angles are intrinsically used to estimate the $\Psi_{lens-shaped}$ by the values of surface energy. Whenever possible, we validate the reliability of these methods and estimations with available experimental and computational data.

5.6. Results and Discussion

First, we calculate the interfacial tension for the liquid-gas and hydrate-liquid contact interfaces. We presented all the details for the calculation methods of these two mixtures in our previous work [62, 70, 71]. We may obtain the interfacial energy associated with the interface between the methane gas and hydrate phases following a direct computation as explained earlier (γ_{hg}) or using the well-known Antonow's rule (γ^*_{hg}) proposed by Kashchiev *et al*. owing to the lack of data on the interfacial tension [19, 72, 73]:

$$\gamma^*_{hg} = \gamma_{hl} + \gamma_{lg} \tag{5.11}$$

Figure 5.4 reports the values of the interfacial tension between all the involved phases as required for the work calculation of methane hydrate formation. To evaluate the results, we compare them with the few existing studies on the water-methane hydrate and water-methane gas interfacial tensions in the pressure and temperature of interest (see Table 5.3). This work demonstrates a great agreement with an average deviation of 1.49%. The hydrate-liquid interfacial tension in this work also compares well with the interfacial tension of cyclopentane hydrate-liquid hydrocarbon and CH_4/C_2H_6 hydrate-liquid hydrocarbon mixtures, which are 47±5 mN/m [20, 74] and 53.3±0.5 mN/m [75], respectively. The interfacial tension at the liquid-gas interface decreases with temperature from 271 K to 289 K, while this temperature increase triggers a slight tension increase at the hydrate-liquid interface (see Figure 5.4a). However, the temperature does not seem to affect the interfacial tension at the hydrate-gas interface. On the other hand, the interfacial tension at all the interfaces monotonically decreases with pressure from 5 MPa to 15 MPa (see Figure 5.4b).

Table 5.3. The available interfacial tension at the water-methane gas and methane hydrate-water interfaces

Investigators	Year	P (MPa)	T (K)	γ_{lg} (mN/m)	γ_{hl} (mN/m)
Naeiji *et al.* [60]	2017	6	275	67.3	39.3
		10		64.7	33.4
		15		60.8	31.7
Kvamme *et al.* [61]	2011	6	275	68.7	
		10		62.7	
Schmidt *et al.* [62]	2003	5	275	69.9	
		6		68.5	
		7		65.5	
		8		63.9	
		9		62.7	
		10		61.5	
Jho *et al.* [63]	2002	5	275	68.1	
		6		66.0	
		7		64.6	
		8		63.3	
		9		62.1	
		10		60.0	
Jacobson *et al.* [64]	2011	6	275		36±2
Anderson *et al.* [65]	2003	10	275		32±3
Uchida *et al.* [66]	2002	10	275		34±6

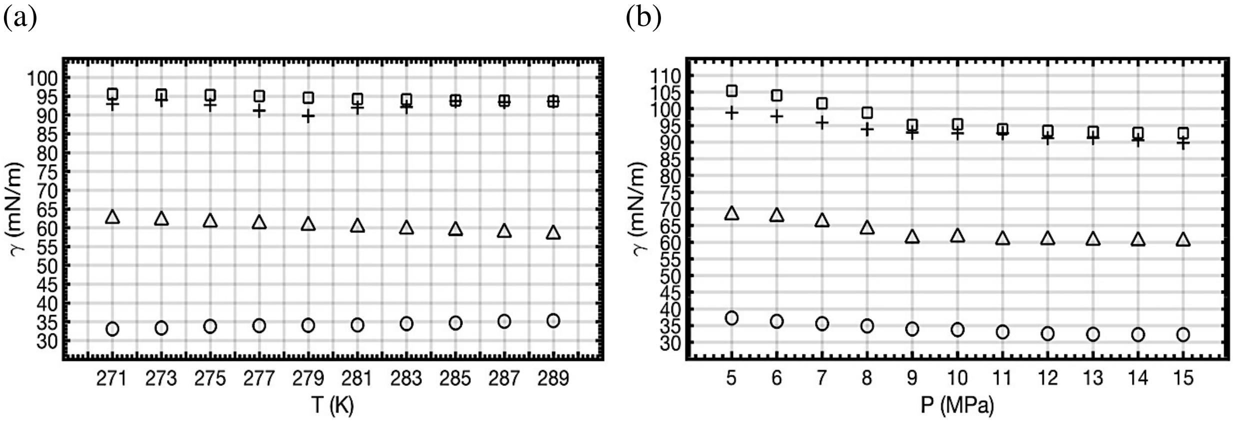

Figure 5.4. The interfacial tension at different temperature (a) and pressure (b). The triangle, circle, plus sign, and square markers represent γ_{lg}, γ_{hl}, γ_{hg}, and γ^{*}_{hg}. The interfacial energy associated with the interface between the methane hydrate and gas phases are obtained from the direct computation (γ_{hg}) and Antonow's rule (γ^{*}_{hg}).

However, the two calculation methods of interfacial tension between the methane hydrate and gas phases reveal the same trends with temperature and pressure in analogous manner to the ice-air interfacial tension [83-85], the direct approach seems to continuously provide lower values at different pressure and temperature. To guarantee the most reliable results for formation work, we need to find the reason behind the deviation, and subsequently, select the correct values for the subsequent calculations.

Figure 5.5 shows a snapshot of the methane gas and hydrate mixture at 275 K and 10 MPa. We visually observe a narrow liquid-like phase of water molecules between the crystalline hydrate and gas molecules originated from the premelting of the hydrate molecules at its surface [86, 87]. The existence of such intermediate quasi-liquid layer has been reported for both ice [88-90] and hydrates [91] mixtures, which explains the function of the Antonow's rule by some means. Herein, we postulate that the presence of this thin layer may relate to the discussed deviation between the two calculation routes of hydrate-gas interfacial tension.

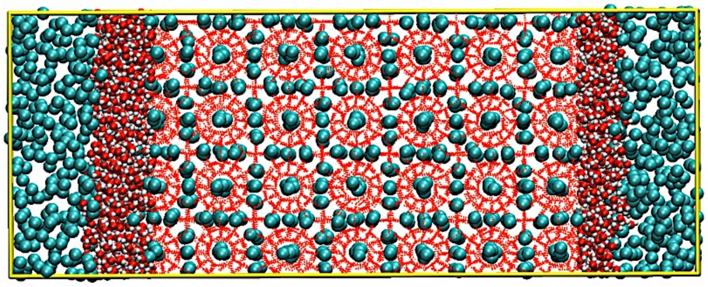

Figure 5.5. Snapshot of a mixture configuration composed of methane hydrate and gas phases. The green, red, and white particles represent the methane molecules, oxygen atoms, and hydrogen atoms, respectively. The red lines denote the hydrogen bonding between the water molecules forming the structure I methane hydrate. The transitional liquid-like phase can be readily distinguished at the methane hydrate-gas interface.

Hence, we evaluate the attractive and repulsive interactions between the methane gas and hydrate boundary surfaces through a series of calculations on the disjoining pressure (Π) [92, 93] to obtain the film spreading coefficient (S) [94, 95], which measures the spontaneous spreading of the quasi-liquid layer:

$$\Pi = P_{QL} - P_{\infty} \tag{5.12}$$

$$S = \int_{\delta_{QL}}^{\infty} \Pi \mathrm{d}\delta_{QL} \tag{5.13}$$

where P_{QL}, P_{∞}, and δ_{QL} represent the internal pressure in the transitional quasi-liquid layer, the bulk pressure, and the quasi-liquid layer thickness, respectively. Therefore, we require the quasi-liquid layer thickness in a range of pressures and temperatures. We systematically increase the system temperature from 271 K up to 295 K to find the temperature, at which hydrate dissociation continues to a full melting process. Hence, we establish the melting temperature (T_m) at 289 K to measure the subcooling (i.e., $\Delta\mathrm{T}_m = T_m - T$). We measure the intermediate liquid-like layer thickness from the charge and local density fluctuations across the interface (see Figure 5.6a). Since the water, methane, and hydrate molecules can be distinguished by their density and charge quantities, we use these criteria to determine the boundaries of this layer. For instance, as we move from the methane gas to hydrate phase in the z-direction, the local molecular densities of water and methane gas at 275 K and 10 MPa simultaneously shift from approximately 0 and 0.16 g/cm^3 to near 1 and 0 g/cm^3, respectively, which represent the boundary of liquid-like layer. Thereafter, the density undulation of crystalline hydrate structure identifies the other boundary of this layer. The charge distribution also follows the density variations and moves from a nonpolar methane gas phase to polar liquid phase. Figure 5.6b shows such thickness decreases with pressure, while it increases with rising temperature (lower subcooling). Please note that this thickness decrease is limited in any temperature and pressure regime, and the layer never vanishes. The reported thickness influenced by the subcooling agrees with the previous work by Jiménez-Ángeles *et al*. at the established melting temperature of 287±1 K [91].

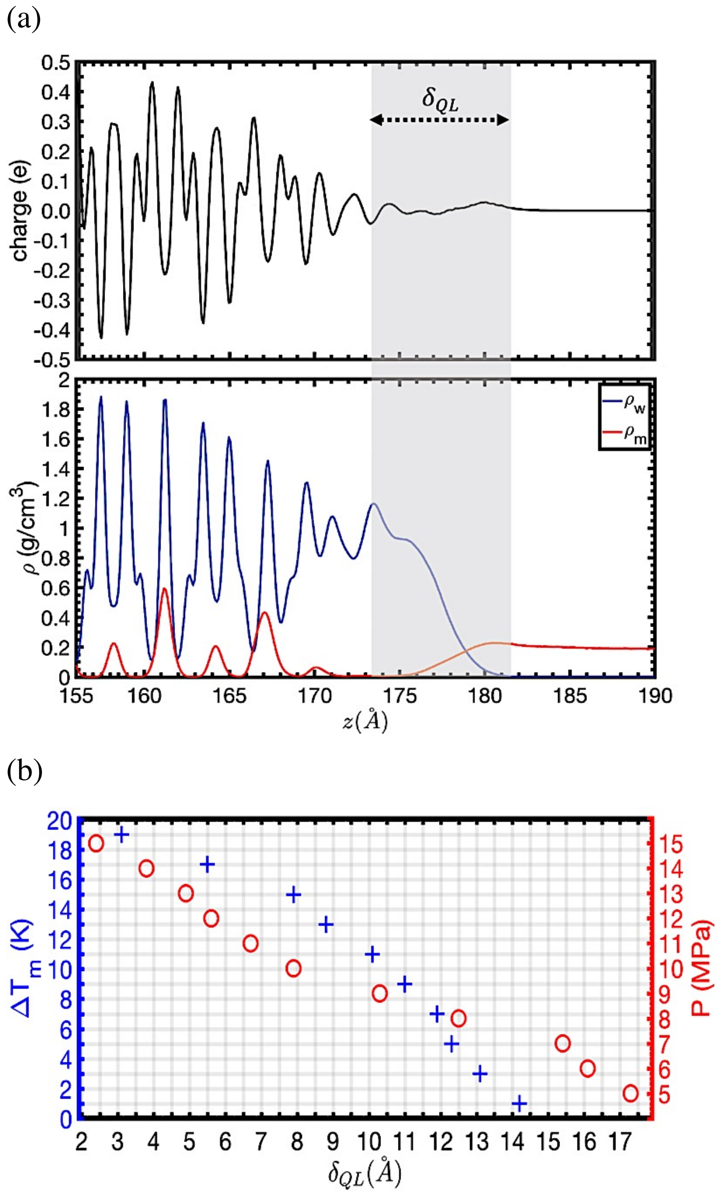

Figure 5.6. The plot (a) shows the charge and local density across the hydrate-gas interface at 275 K and 10 MPa to determine the quasi-liquid layer thickness. The blue and red lines represent the local density of water and methane molecules, respectively. The thickness of the intermediate quasi-liquid layer (b) formed between the methane gas and hydrate phases at different pressure (circle signs) and subcooling level (plus signs). The blue and red data are for

the systems at constant 10 MPa and 275 K, respectively. This thickness decreases with pressure and subcooling.

Figure 5.7 shows the disjoining pressure of the methane hydrate and gas mixture at different temperature and pressure as per Eqn. 5.12. The imbalance between the attractive and repulsive forces of the broken bonds at the hydrate and gas interfaces causes a series of negative Π, which means these interfaces experience an increasingly attractive force when they approach each other. This disjoining pressure increases with temperature increase or pressure drop. We may insert the disjoining pressure and thickness data into the well-known Hamaker's formula [96] to obtain the Hamaker constant (A), and consequently, validate our results:

$$\Pi = -\frac{A}{6\pi {\delta_{QL}}^{3}} \tag{5.14}$$

The average Hamaker constant in this work is 3.11×10^{-19} J, which is consistent with the value of 1.140×10^{-19} J for methane hydrates in vacuum [97] or 3×10^{-19} J [98] and 4×10^{-19} J [99] obtained for similar water-metal mixtures conforming to the resemblance of crystalline structure of methane hydrates to metals.

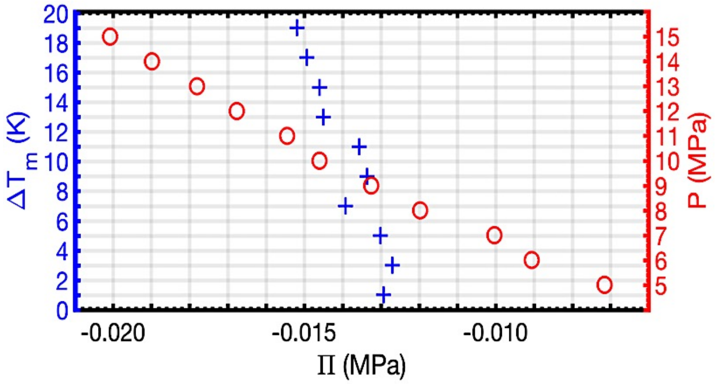

Figure 5.7. The disjoining pressure at different pressure (circle signs) and temperature (plus signs) regimes. The blue and red data are for the systems at constant 10 MPa and 275 K, respectively. High pressure or subcooling drops this pressure.

Depending on the definition of the spreading coefficient S and the material properties and structure in the interfacial region, the spreading coefficient might be zero, positive, or negative [100, 101]. We find that S is negative in the methane hydrate and gas mixture owing to the perpetual negative disjoining pressure at temperature and pressure ranges of 271-289 K and 5-15 MPa, respectively. Negative spreading coefficient is required for the premelting process at the interface [86].

In addition to Eqn. 5.13, the classical definition of the spreading coefficient is [94, 100, 102]:

$$S = \gamma_{hg} - \gamma_{hg}^{*} \tag{5.15}$$

This relation combined with the negative S implies that γ_{hg} must always be lower than γ_{hg}^{*}. Hence, we conclude that the usage of the approximating Antonow's rule interfacial tension at the methane hydrate-gas interface suggested by Kashchiev *et al.* [19] yields inaccurate results because of the liquid-like film that forms on the interface. Please note that this conclusion is based on the negative spreading coefficient at the interface of sI methane hydrate-methane gas, while this layer can play a different role in a system with a different structure. Next, with the known interfacial tensions at the different interfaces, we proceed to calculate the work of cluster formation.

Figure 5.8 represents the formation work after numerical calculation for different nucleation scenarios of the pure methane hydrate at two sets of system temperature and pressure with a typical set of parameters, which are $c = \sqrt[3]{36\pi}$ for spherical clusters and $v_h = 0.216$ nm^3 [19, 36]. The lowest work belongs to a complete surface wetting that forms a film or disk-like interface as the interfacial energy does not intervene in this form of nucleation morphology. In addition to the effect of favorable thermodynamic regime (i.e., high pressure and low temperature), the cap-shaped cluster with more wetting surface (small θ) lowers the work needed for formation of methane hydrates. We increase the formation work with the wetting angle until we utterly lose the wetting concept to reach the work equal to homogeneous nucleation scenario. Interfacial energy at different surfaces of lens-shaped nucleation controls the formation so that the morphology is analogous to the homogeneous case, which triggers similar formation work. For instance, the α and β of the system at 275 K and 10 MPa are 151.61° and 9.99°, respectively. $\alpha+\beta=161.6°$ leads to a cluster submerged mostly in the water phase, rather than the gas phase. Not to mention that the lens-shaped nucleation is energetically more favorable compared to homogenous nucleation. Using Antonow's rule concludes the same work of formation for both lens-shaped and homogeneous forms [19], however the negative spreading parameter in the intermediate quasi-liquid layer between the gas and hydrate phases causes deviation from the Antonow's rule, which lowers the interfacial tension, and thus, the formation work. Hence, the premelting methane hydrate crystal at the hydrate-gas interface works in favor of the lens-shaped hydrate formation.

In conclusion, the methane solution theoretically tends to initiate nucleation in the ranked order of film-shaped, cap-shaped, lens-shaped, and lastly homogeneous. Nevertheless, the subtle difference between the formation work of homogeneous and lens-shaped configurations implies that the abundance of water and methane gas molecules at the interface of methane gas and liquid phases, not the interfacial energy contribution, is the main reason underlying higher thermodynamic probability of the lens-shaped nucleation, against homogeneous clustering, so that the labile hydrate clusters are adsorbed and agglomerated on the gas-liquid interface to form local structures of nucleation.

As discussed above, high supersaturation as the driving force of the cluster formation reduces its work. With hydrate crystal expansion, the interfacial energy contribution prevails over the supersaturation effect hindering the formation until the number of unit cells reaches the point that the energy role reversal occurs in the favor of formation by the driving force. Such critical number of crystal unit cells, corresponding to a critical radius of hydrate phase, and its maximum formation work can be mathematically calculated by taking the first derivative of the expression for work of cluster formation with respect to n:

$$n^* = \frac{8c^3 v_h^2 \gamma^3}{27\Delta\mu^3} \tag{5.16}$$

$$W^* = \frac{4c^3 v_h^2 \gamma^3}{27\Delta\mu^2} \tag{5.17}$$

Figure 5.9 demonstrates that the lens-shaped or cap-shaped heterogeneous clustering with a small wetting angle are more favorable than homogeneous nucleation in order to physically reduce the energy barrier of formation. As per Eqn. (16) and (17), the $n*$ and $W*$ for the film-shaped case equal to zero, which lead to a formation process with no critical nucleus and induction period. While, this low energy cost theoretically supports the high possibility of hydrate film formation as previously shown [23, 103], we neglect this scenario in the calculation of critical size and work as it may obey a different set of formulations. Furthermore, Figure 5.10 summarizes how this formation barrier is minimized by the pressure and temperature, regarded as the most important thermodynamic conditions in hydrate crystal nucleation. In agreement with the experiments [1], low temperature and high pressure provide the perfect setting for the hydrate crystal nucleation to occur.

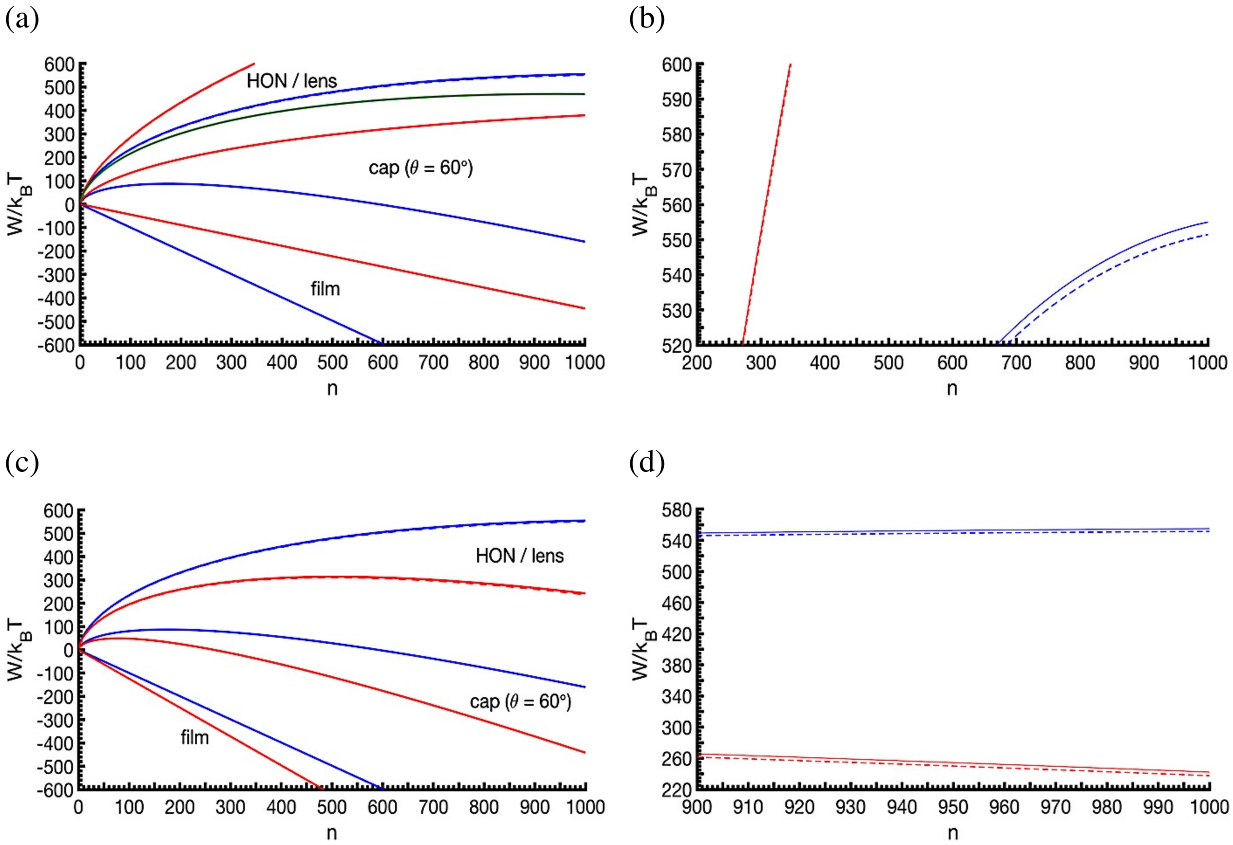

Figure 5.8. Work of methane hydrate nucleation under different formation scenarios and thermodynamic conditions. The plot (a) is for a system at 275 K (blue line) and 281 K (red line) with the constant pressure of 10 MPa. The green line shows the work for the cap-shaped clustering with θ of 120°. The formation work increases as the system temperature increases. The film-shaped, cap-shaped, and lens-shaped nucleation lower the work of formation compared to the homogeneous case. The plot (b) distinguishes the difference between homogeneous (solid) and lens-shape (dashed) nucleation work. The plot (c) is for a system at 10 MPa (blue line) and 15 MPa (red line) with the constant temperature of 275 K. The work of formation decreases with pressure. The plot (d) magnifies the variation between the work of lens-shape (dashed) and homogeneous (solid) formation.

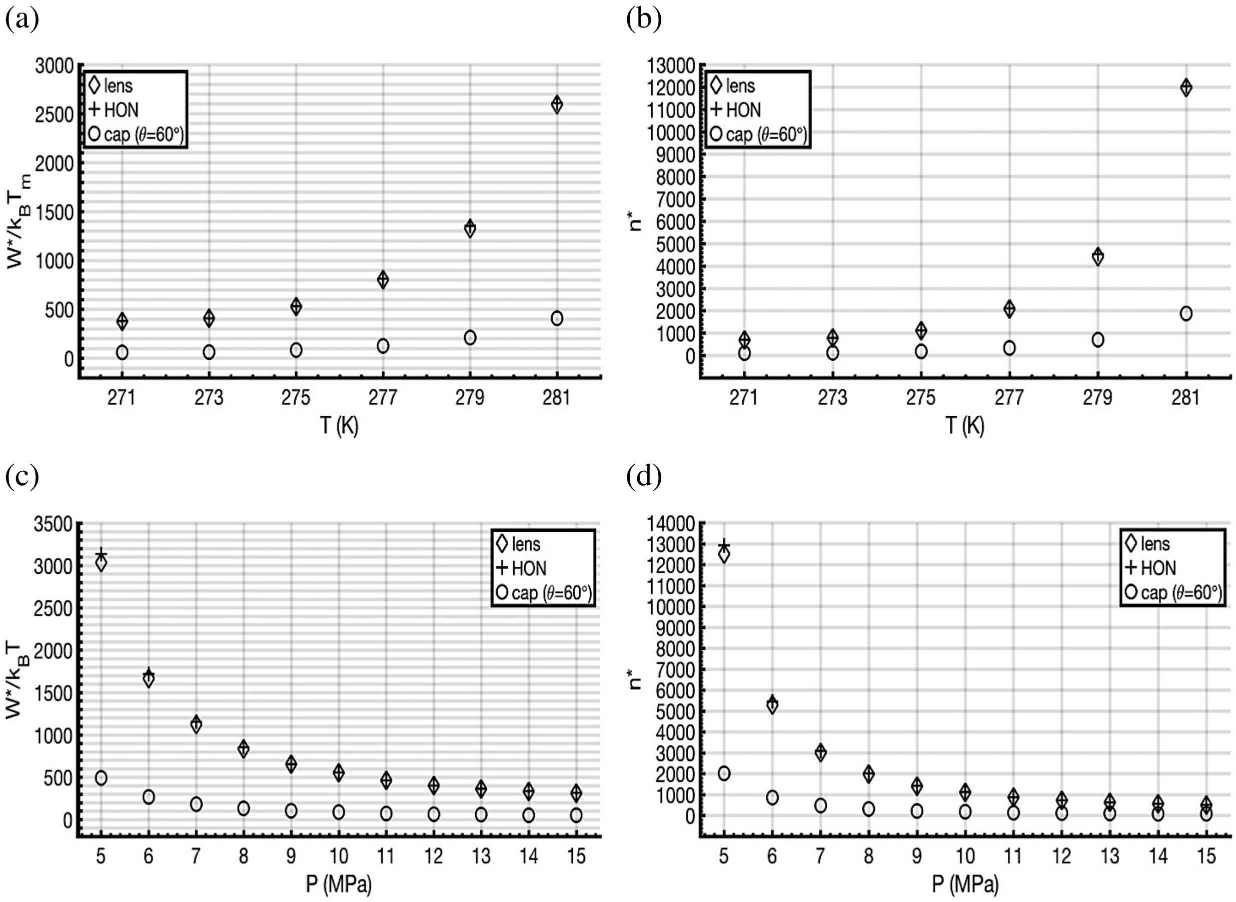

Figure 5.9. Maximum formation work and its corresponding number of crystal unit cells depend on the cluster formation shape (homogenous or heterogeneous), temperature (a and b) at 10 MPa, and pressure (c and d) at 275 K. The system with high pressure, low temperature, and heterogeneous clustering with a small wetting angle requires lower work of formation. Furthermore, lens-shaped heterogeneous formation is narrowly favorable compared to the homogeneous nucleation.

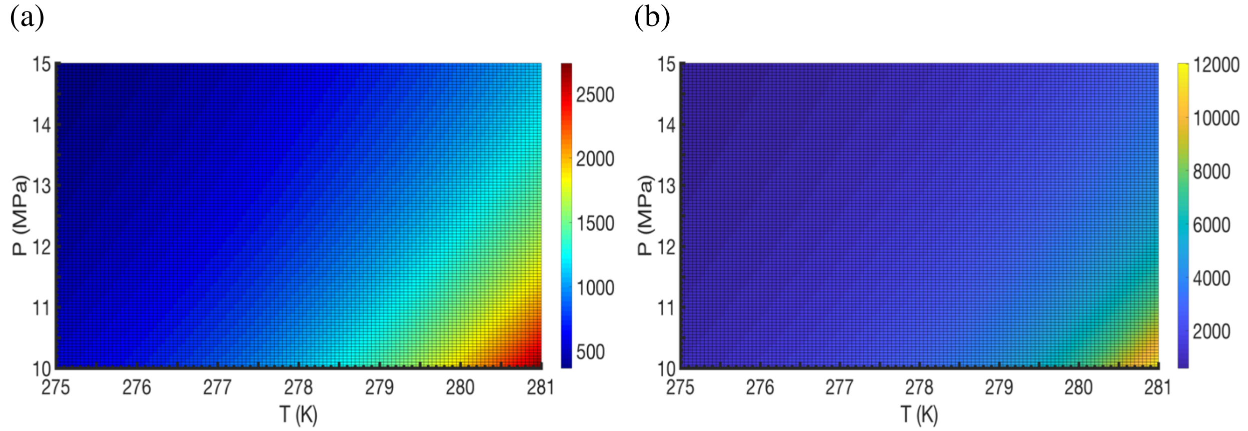

Figure 5.10. The maximum formation work in units of k_BT (a) and critical number of crystal unit cells (b) for homogeneous nucleation at different pressure and temperature. Low temperature and high-pressure thermodynamic conditions require minimum formation work and critical size, which vastly facilitate the hydrate nucleation process.

Next, we determine the rate of hydrate cluster formation in order to study the effect of the involved surfaces in the crystal nucleation rate. We consider the general expression in single-component gas hydrate system [19]. Hence, the nucleation rate (J) in units of $1/m^3s$ can be obtained from:

$$J = A exp\left(\frac{\Delta\mu}{k_BT} - \frac{4c^3v_h^2\gamma^3}{27k_BT\Delta\mu^2}\right) \tag{5.18}$$

where A ($1/m^3s$) is the kinetic factor that accounts for the attachment mechanism of the crystal unit cells to the cluster depending on the nucleation type (HON or HEN). This factor is independent of the supersaturation condition. In addition, we include additives in the solution obeying the Langmuir adsorption isotherm to evaluate the covering effect on the cluster active surface (i.e., the involved surface in the formation process). Please note that the impact of additives on the surface energy is not the concern of this work. Therefore, the nucleation rate of hydrate clusters with a fraction of the active surface is calculated by the expression below:

$$J = \left(\frac{A}{1+k_nC_a}\right) exp\left(\frac{\Delta\mu - W^*}{k_BT}\right) \tag{5.19}$$

where k_n (m^3) and C_a ($1/m^3$) are the Langmuir adsorption constant and the additive concentration, respectively. Please note that we choose k_n so that the additive adsorption is assumed to be independent of the system temperature and pressure. Figure 5.11 depicts how the nucleation morphology and the additive concentration contribute in the crystalline nucleation rate. The reported trend and magnitude of nucleation rates are consistent with previous experimental analysis performed for methane hydrates [104]. All heterogeneous nucleation forms including film, cap, and lens shapes expectedly increase the nucleation rate in different pressure and temperature regimes. According to these nucleation rate results, the ranked order of nucleation shapes reconciles with the results obtained from the formation work.

Herein, one may inhibit the hydrate formation with supplying an additive in the solution provided that the additives are strongly adsorbed on the surface of the hydrate cluster, and do not generate new nucleation sites. High concentration of the surface covering additives might be used as kinetic inhibitor to solve the issue of pipeline blockage in petroleum industry. This current work on additives merely reveals the inhibiting effect due to the applied assumptions, while some additives promote the nucleation rate. Hence, there needs to be more focus on the significance of the additives on the surface energy, creation of new nucleation sites, and the attachment strength to mimic a more realistic model.

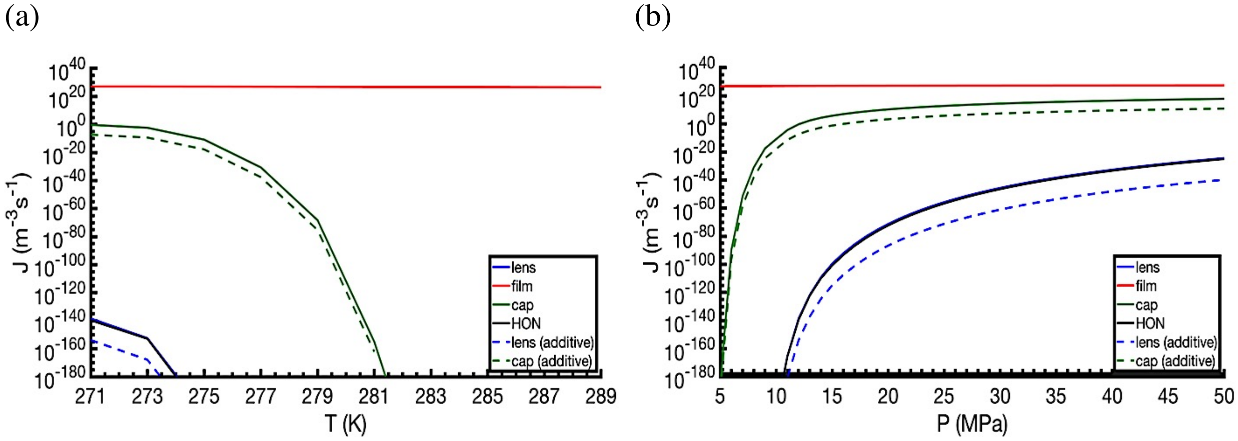

Figure 5.11. Gas hydrate nucleation rate in different temperature (a) and pressure (b) regimes with (dashed) or without (solid) additives. The constant pressure of plot (a) and temperature of plot (b) are 10 MPa and 275 K, respectively. A is assumed to be 10^{35} and 4×10^{26} 1/m^{3}s for HON and HEN nucleation processes, respectively [19]. Blue, red, green, and black lines represent the lens-shaped, film-shaped, cap-shaped, and homogeneous forms of clustering, respectively. In this work, we adopt the arbitrary values of 10^{-18} m^3 and 10^{25} 1/m^3 for k_n and C_a, respectively.

Finally, we apply the ice-water interfacial tension of 29.1 mN/m [105] as a substitute to the hydrate-water interfacial tension for a system at 275 K and different pressures. Figure 5.12 clearly shows that a slight change in such interfacial tension escalates the formation nucleation rate by orders of magnitude. Therefore, we inevitably need to use the interfacial tension values of methane hydrate to obtain the most sensible results.

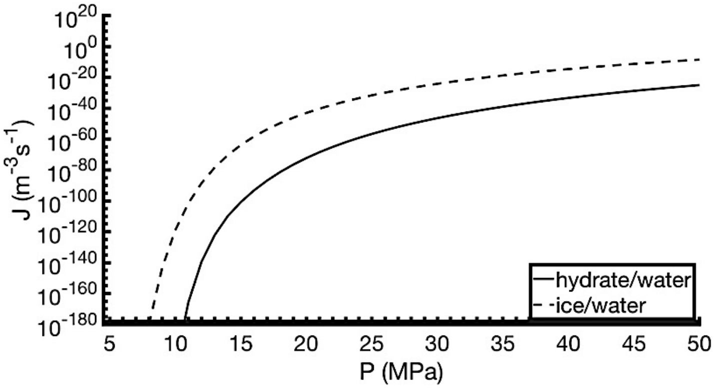

Figure 5.12. The formation nucleation rate using the interfacial tension of methane hydrate-water (solid line) and ice-water (dashed line) at 275 K. The rate is prodigiously higher when the ice-water properties are applied.

5.7. Summary and Conclusions

The interaction of methane gas and water at low temperature and high pressure may cause methane hydrate formation. In both industrial and natural environments, the nucleation appears in the solution bulk or at the solid-liquid and liquid-gas interfaces forming different morphologies. To promote or inhibit this nucleation process, we are able to further understand the work, location, and morphology of the formation through classical nucleation theory. Therefore, we employed a combination of molecular dynamics technique and theoretical computation to obtain the formation work. The main focus is on the interfacial energy contribution in the nucleation process of methane gas hydrates that has not been well studied before, while, it has shown a large effect in the widespread applications of clathrate hydrates, specifically in flow assurance owing to the chemical composition of natural gas.

We first computed the interfacial tension at water-methane hydrate and water-methane gas interfaces, and afterwards, applied our method and Antonow's rule to find the interfacial tension at the interface between methane hydrate and the gas phase. We showed that a quasi-liquid layer was formed between the hydrate and gas phases due to the premelting process of crystalline hydrate in contact with the methane gas molecules. The existence of this thin intermediate layer causes the Antonow's rule to overestimate the interfacial tension, and consequently it cannot be used to estimate the tension values at the hydrate-gas interface, which was proposed by Kashchiev *et al*. [19]. With the necessary interfacial properties at hand we then calculated the formation work and nucleation rate of methane hydrate. We concluded that nucleation was more favorable in low temperature and high pressure regimes, and likewise, at the water-methane hydrate interface in a shape of a film or disk. The other formation morphologies in order of occurrence likelihood were cap-shaped, lens-shaped, and homogeneous forms of nucleation, respectively. We proposed that the existence of a quasi-liquid layer between the methane hydrate and gas surfaces causes lower formation work for the lens-shaped formation compared to homogeneous. Nonetheless, high concentration of methane gas and water molecules at the surface, not the interfacial energy contribution as pointed by Aman *et al*. [20], is found to be the leading reason of lens-shape formation as opposed to homogeneous. In addition, we demonstrated that the presence of additives in the mixture of water-methane gas reduces the nucleation rate, which inhibited the hydrate formation process. Lastly, we presented the nucleation rate employing the interfacial tension at the ice surfaces, instead of hydrate, which led to significantly larger nucleation rates. This large discrepancy prevents the usage of ice properties from estimating the interfacial energy in hydrate studies.

In summary, the reported results on different aspects of methane hydrate critically deliver a qualitative and quantitative set of information in gas hydrate formation through the characterization of the water-hydrate, water-gas, and hydrate-gas interfaces. We anticipate this work will significantly contribute to a better understanding of the kinetics of clathrate hydrate formation in different thermodynamic pressure and temperature regimes and to the many technological processes that rely on interfacial science. However, other possible morphologies of methane hydrate nucleation such as sII methane hydrate may lead to distinct interfacial structures and shape factors, and consequently, alter the conclusions of this work. Moreover, a deeper analysis on the impact of surface covering additives on the surface energy, the attachment strength, and creation of new nucleation sites is necessary for surfactants applications. In addition to the study on the interfacial energy contribution, their needs to be more work performed on the modeling of methane hydrate formation through the classical nucleation theory in regards to the supersaturation contribution into the nucleation process.

5.8. Acknowledgements

This research is financially supported by the McGill Engineering Doctoral Awards (MEDA), James McGill Professorship appointment (ADR), and Natural Sciences and Engineering Research Council (NSERC). The authors are also grateful to Compute Canada and Calcul Québec for the access to the supercomputers Graham and Cedar, and their technical assistance.

5.9. References

1. Sloan Jr, E.D. and C. Koh, Clathrate hydrates of natural gases. 2007: CRC press.
2. Jendi, Z.M., P. Servio, and A.D. Rey, Ideal strength of methane hydrate and ice Ih from first-principles. Crystal Growth & Design, 2015. 15(11): p. 5301-5309.
3. Vlasic, T.M., P. Servio, and A.D. Rey, Atomistic modeling of structure II gas hydrate mechanics: Compressibility and equations of state. AIP Advances, 2016. 6(8): p. 085317.
4. Vlasic, T.M., P.D. Servio, and A.D. Rey, Effect of guest size on the mechanical properties and molecular structure of gas hydrates from first-principles. Crystal Growth & Design, 2017. 17(12): p. 6407-6416.
5. Carroll, J., Natural gas hydrates: a guide for engineers. 2014: Gulf Professional Publishing.
6. Ginley, D.S. and D. Kahen, Fundamentals of materials for energy and environmental sustainability. 2012, Cambridge; New York: Cambridge University Press.
7. Riedel, M., E.C. Willoughby, and S. Chopra, Geophysical characterization of gas hydrates. 2010, Tulsa, OK: Society of Exploration Geophysicists.
8. Koh, C.A., et al., Fundamentals and applications of gas hydrates. 2011.
9. Englezos, P. and J.D. Lee, Gas hydrates: A cleaner source of energy and opportunity for innovative technologies. Korean Journal of Chemical Engineering, 2005. 22(5): p. 671-681.
10. Klauda, J.B. and S.I. Sandler, Global distribution of methane hydrate in ocean sediment. Energy & Fuels, 2005. 19(2): p. 459-470.
11. Demirbas, A., Methane gas hydrate. 2010: Springer Science & Business Media.

12. Sloan, E.D., Fundamental principles and applications of natural gas hydrates. Nature, 2003. 426(6964): p. 353-363.

13. Fandiño, O. and L. Ruffine, Methane hydrate nucleation and growth from the bulk phase: Further insights into their mechanisms. Fuel, 2014. 117, Part A: p. 442-449.

14. Sloan, E.D., Natural gas hydrates in flow assurance. 2011.

15. Zerpa, L.E., et al., Surface chemistry and gas hydrates in flow assurance. Industrial & Engineering Chemistry Research, 2011. 50(1): p. 188-197.

16. Bai, X.-M. and M. Li, Test of classical nucleation theory via molecular-dynamics simulation. The Journal of chemical physics, 2005. 122(22): p. 224510.

17. Lupi, L., B. Peters, and V. Molinero, Pre-ordering of interfacial water in the pathway of heterogeneous ice nucleation does not lead to a two-step crystallization mechanism. The Journal of chemical physics, 2016. 145(21): p. 211910.

18. Warrier, P., et al., Overview: Nucleation of clathrate hydrates. The Journal of chemical physics, 2016. 145(21): p. 211705.

19. Kashchiev, D. and A. Firoozabadi, Nucleation of gas hydrates. Journal of Crystal Growth, 2002. 243(3–4): p. 476-489.

20. Aman, Z.M. and C.A. Koh, Interfacial phenomena in gas hydrate systems. Chemical Society Reviews, 2016. 45(6): p. 1678-1690.

21. Tanaka, R., R. Sakemoto, and R. Ohmura, Crystal growth of clathrate hydrates formed at the interface of liquid water and gaseous methane, ethane, or propane: variations in crystal morphology. Crystal Growth & Design, 2009. 9(5): p. 2529-2536.

22. Asserson, R.B., et al., Interfacial tension measurement of freon hydrates by droplet deposition and contact angle measurements. Journal of Petroleum Science and Engineering, 2009. 68(3–4): p. 209-217.

23. Sun, C.Y., et al., Studies on hydrate film growth. Annual Reports Section "C" (Physical Chemistry), 2010. 106(0): p. 77-100.

24. Koop, T. and B.J. Murray, A physically constrained classical description of the homogeneous nucleation of ice in water. The Journal of chemical physics, 2016. 145(21): p. 211915.

25. Sarupria, S. and P.G. Debenedetti, Homogeneous nucleation of methane hydrate in microsecond molecular dynamics simulations. The journal of physical chemistry letters, 2012. 3(20): p. 2942-2947.

26. Knott, B.C., et al., Homogeneous nucleation of methane hydrates: Unrealistic under realistic conditions. Journal of the American Chemical Society, 2012. 134(48): p. 19544-19547.

27. Bagherzadeh, S.A., et al., Influence of hydrated silica surfaces on interfacial water in the presence of clathrate hydrate forming gases. The Journal of Physical Chemistry C, 2012. 116(47): p. 24907-24915.

28. Bai, D., et al., How properties of solid surfaces modulate the nucleation of gas hydrate. Scientific Reports, 2015. 5: p. 12747.

29. Liang, S. and P.G. Kusalik, The nucleation of gas hydrates near silica surfaces. Canadian Journal of Chemistry, 2014. 93(8): p. 791-798.

30. Koga, T., et al., Hydrate formation at the methane/water interface on the molecular scale. Langmuir, 2010. 26(7): p. 4627-4630.

31. Zhao, J., et al., Microstructural characteristics of natural gas hydrates hosted in various sand sediments. Physical Chemistry Chemical Physics, 2015. 17(35): p. 22632-22641.

32. Davies, S.R., et al., Studies of hydrate nucleation with high pressure differential scanning calorimetry. Chemical Engineering Science, 2009. 64(2): p. 370-375.

33. Englezos, P., et al., Kinetics of formation of methane and ethane gas hydrates. Chemical Engineering Science, 1987. 42(11): p. 2647-2658.

34. Vatamanu, J. and P.G. Kusalik, Observation of two-step nucleation in methane hydrates. Physical Chemistry Chemical Physics, 2010. 12(45): p. 15065-15072.

35. Zhang, Z. and G.-J. Guo, The effects of ice on methane hydrate nucleation: a microcanonical molecular dynamics study. Physical Chemistry Chemical Physics, 2017. 19(29): p. 19496-19505.

36. Kashchiev, D. and A. Firoozabadi, Driving force for crystallization of gas hydrates. Journal of Crystal Growth, 2002. 241(1–2): p. 220-230.

37. Kashchiev, D. and A. Firoozabadi, Induction time in crystallization of gas hydrates. Journal of crystal growth, 2003. 250(3-4): p. 499-515.

38. Khadem, S.A. and A.D. Rey, Thermodynamic modelling of acidic collagenous solutions: from free energy contributions to phase diagrams. Soft matter, 2019. 15(8): p. 1833-1846.

39. Kashchiev, D., Nucleation : basic theory with applications. 2000, Butterworth Heinemann: Oxford ;.

40. Khadem, S.A. and R.B. Boozarjomehry, Development of systematic framework for an intelligent decision support system in gas transmission network. Industrial & Engineering Chemistry Research, 2015. 54(43): p. 10768-10786.
41. Khadem, S.A., et al., Pressure and temperature functionality of paraffin-carbon dioxide interfacial tension using genetic programming and dimension analysis (GPDA) method. Journal of Natural Gas Science and Engineering, 2014. 20: p. 407-413.
42. Khadem, S.A. and A. Rey, Theoretical Platform for Liquid-Crystalline Self-assembly of Collagen-Based Biomaterials. Frontiers in Physics, 2019. 7: p. 88.
43. Binks, B.P. and J.H. Clint, Solid wettability from surface energy components: relevance to pickering emulsions. Langmuir, 2002. 18(4): p. 1270-1273.
44. Vázquez, U.O.M., et al., Calculating the surface tension between a flat solid and a liquid: a theoretical and computer simulation study of three topologically different methods. Journal of Mathematical Chemistry, 2009. 45(1): p. 161-174.
45. Chaplin, M., Theory vs experiment: what is the surface charge of water? Water Journal Multidisciplinary Research Journal 1, 2009: p. 1-28.
46. Eisenberg, D., D.S. Eisenberg, and W. Kauzmann, The structure and properties of water. 2005: Oxford University Press on Demand.
47. Kirkwood, J.G. and F.P. Buff, The statistical mechanical theory of surface tension. The Journal of Chemical Physics, 1949. 17(3): p. 338-343.
48. Tolman, R.C., Consideration of the Gibbs theory of surface tension. The journal of chemical physics, 1948. 16(8): p. 758-774.
49. Takeuchi, F., et al., Water proton configurations in structures I, II, and H clathrate hydrate unit cells. The Journal of chemical physics, 2013. 138(12): p. 124504.
50. Gutt, C., et al., The structure of deuterated methane–hydrate. The journal of chemical physics, 2000. 113(11): p. 4713-4721.
51. Conde, M. and C. Vega, Determining the three-phase coexistence line in methane hydrates using computer simulations. The Journal of chemical physics, 2010. 133(6): p. 064507.
52. Soustelle, M., Thermodynamics of surfaces and capillary systems. 2016, ISTE, Ltd. ; John Wiley & Sons: London, UK; Hoboken, NJ.
53. Erbil, H.Y., Surface chemistry of solid and liquid interfaces. 2006, Oxford, UK ; Blackwell Pub.

54. Jorgensen, W.L., J.D. Madura, and C.J. Swenson, Optimized intermolecular potential functions for liquid hydrocarbons. Journal of the American Chemical Society, 1984. 106(22): p. 6638-6646.

55. Horn, H.W., et al., Development of an improved four-site water model for biomolecular simulations: TIP4P-Ew. The Journal of chemical physics, 2004. 120(20): p. 9665-9678.

56. Plimpton, S., Fast parallel algorithms for short-range molecular dynamics. Journal of computational physics, 1995. 117(1): p. 1-19.

57. Krouskop, P.E., et al., Solubility of simple, nonpolar compounds in TIP4P-Ew. The Journal of chemical physics, 2006. 124(1): p. 016102.

58. Tung, Y.-T., et al., The growth of structure I methane hydrate from molecular dynamics simulations. The Journal of Physical Chemistry B, 2010. 114(33): p. 10804-10813.

59. Zielkiewicz, J., Structural properties of water: Comparison of the SPC, SPCE, TIP4P, and TIP5P models of water. The Journal of chemical physics, 2005. 123(10): p. 104501.

60. Hockney, R.W. and J.W. Eastwood, Computer simulation using particles. 1988: crc Press.

61. Isele-Holder, R.E., W. Mitchell, and A.E. Ismail, Development and application of a particle-particle particle-mesh Ewald method for dispersion interactions. The Journal of chemical physics, 2012. 137(17): p. 174107.

62. Mirzaeifard, S., P. Servio, and A.D. Rey, Multiscale Modeling and Simulation of Water and Methane Hydrate Crystal Interface. Crystal Growth & Design, 2019.

63. Firoozabadi, A., Thermodynamics of hydrocarbon reservoirs. 1999: McGraw-Hill.

64. Ghiass, M. and A.D. Rey, Interfacial thermodynamics of compressible polymer solutions. 2008, AIP.

65. Rowlinson, J.S. and B. Widom, Molecular theory of capillarity. 2013: Courier Corporation.

66. Blokhuis, E., et al., Tail corrections to the surface tension of a Lennard-Jones liquid-vapour interface. Molecular Physics, 1995. 85(3): p. 665-669.

67. Chapela, G.A., et al., Computer simulation of a gas–liquid surface. Part 1. Journal of the Chemical Society, Faraday Transactions 2: Molecular and Chemical Physics, 1977. 73(7): p. 1133-1144.

68. Grest, G.S., et al., Substructured multibody molecular dynamics. 2006, Sandia National Laboratories.

69. Qi, X., T. Balankura, and K.A. Fichthorn, Theoretical Perspectives on the Influence of Solution-Phase Additives in Shape-Controlled Nanocrystal Synthesis. The Journal of Physical Chemistry C, 2018. 122(33): p. 18785-18794.

70. Mirzaeifard, S., P. Servio, and A.D. Rey, Molecular Dynamics Characterization of the Water-Methane, Ethane, and Propane Gas Mixture Interfaces. Chemical Engineering Science, 2019.

71. Mirzaeifard, S., P. Servio, and A.D. Rey, Molecular dynamics characterization of temperature and pressure effects on the water-methane interface. Colloid and Interface Science Communications, 2018. 24: p. 75-81.

72. Høiland, S., et al. Wettability of Freon hydrates in crude oil/brine emulsions: The effect of chemical additives. in Proceedings of the 5th International Conference on Gas Hydrates. 2005.

73. Peeters, P., Nucleation and condensation in gas-vapor mixtures of alkanes and water. 2004.

74. Aman, Z.M., et al., Surfactant adsorption and interfacial tension investigations on cyclopentane hydrate. Langmuir, 2013. 29(8): p. 2676-2682.

75. Hu, S. and C.A. Koh, Interfacial properties and mechanisms dominating gas hydrate cohesion and adhesion in liquid and vapor hydrocarbon phases. Langmuir, 2017. 33(42): p. 11299-11309.

76. Naeiji, P., F. Varaminian, and M. Rahmati, Comparison of the thermodynamic, structural and dynamical properties of methane/water and methane/water/hydrate systems using molecular dynamic simulations. Journal of Natural Gas Science and Engineering, 2017. 44: p. 122-130.

77. Kvamme, B., T. Kuznetsova, and K. Schmidt. Experimental measurements and numerical modelling of interfacial tension in water-methane systems. in Presentation at the International Conference of Computational Methods in Sciences and Engineering, Chania, Greece. 2006.

78. Schmidt, K.A., G.K. Folas, and B. Kvamme, Calculation of the interfacial tension of the methane–water system with the linear gradient theory. Fluid Phase Equilibria, 2007. 261(1): p. 230-237.

79. Jho, C., et al., Effect of pressure on the surface tension of water: Adsorption of hydrocarbon gases and carbon dioxide on water at temperatures between 0 and 50 C. Journal of Colloid and Interface Science, 1978. 65(1): p. 141-154.

80. Jacobson, L.C. and V. Molinero, Can amorphous nuclei grow crystalline clathrates? The size and crystallinity of critical clathrate nuclei. Journal of the American Chemical Society, 2011. 133(16): p. 6458-6463.

81. Anderson, R., et al., Experimental measurement of methane and carbon dioxide clathrate hydrate equilibria in mesoporous silica. The Journal of Physical Chemistry B, 2003. 107(15): p. 3507-3514.

82. Uchida, T., et al., Effects of pore sizes on dissociation temperatures and pressures of methane, carbon dioxide, and propane hydrates in porous media. The journal of physical chemistry B, 2002. 106(4): p. 820-826.

83. Djikaev, Y. and E. Ruckenstein, Self-Consistent Determination of the Ice–Air Interfacial Tension and Ice–Water–Air Line Tension from Experiments on the Freezing of Water Droplets. The Journal of Physical Chemistry C, 2017. 121(30): p. 16432-16439.

84. Djikaev, Y.S. and E. Ruckenstein, Dependence of homogeneous crystal nucleation in water droplets on their radii and its implication for modeling the formation of ice particles in cirrus clouds. Physical Chemistry Chemical Physics, 2017. 19(30): p. 20075-20081.

85. Dufour, L. and R. Defay, Thermodynamics of clouds. International geophysics series ; v. 6. 1963, New York: Academic Press.

86. Dash, J., A. Rempel, and J. Wettlaufer, The physics of premelted ice and its geophysical consequences. Reviews of modern physics, 2006. 78(3): p. 695.

87. Wettlaufer, J., Impurity effects in the premelting of ice. Physical Review Letters, 1999. 82(12): p. 2516.

88. Döppenschmidt, A. and H.-J. Butt, Measuring the thickness of the liquid-like layer on ice surfaces with atomic force microscopy. Langmuir, 2000. 16(16): p. 6709-6714.

89. Maruyama, M., et al., Interfacial melting of ice in graphite and talc powders. Journal of crystal growth, 1992. 118(1-2): p. 33-40.

90. Shepherd, T.D., M.A. Koc, and V. Molinero, The quasi-liquid layer of ice under conditions of methane clathrate formation. The Journal of Physical Chemistry C, 2012. 116(22): p. 12172-12180.

91. Jiménez-Ángeles, F. and A. Firoozabadi, Induced charge density and thin liquid film at hydrate/methane gas interfaces. The Journal of Physical Chemistry C, 2014. 118(45): p. 26041-26048.

92. Sedev, R., Fundamentals of Surface Forces. 2014.

93. Rey, A.D., Mechanical theory of structural disjoining pressure in liquid crystal films. Physical Review E, 2000. 61(4): p. 4632.

94. Rey, A.D., Mechanical theory for nematic thin films. Langmuir, 2001. 17(6): p. 1922-1927.

95. Emelyanenko, K., A. Emelyanenko, and L. Boinovich, Spreading and contraction of a benzene lens on water: A description on the basis of the disjoining pressure. Colloids and Surfaces A: Physicochemical and Engineering Aspects, 2017. 522: p. 601-607.

96. Hamaker, H.C., The London—van der Waals attraction between spherical particles. physica, 1937. 4(10): p. 1058-1072.

97. Bonnefoy, O., F. Gruy, and J.-M. Herri, Van der Waals interactions in systems involving gas hydrates. Fluid Phase Equilibria, 2005. 231(2): p. 176-187.

98. Hu, H. and Y. Sun, Molecular dynamics simulations of disjoining pressure effect in ultra-thin water film on a metal surface. Applied Physics Letters, 2013. 103(26): p. 263110.

99. Parsegian, V.A. and G.H. Weiss, Spectroscopic parameters for computation of van der Waals forces. Journal of Colloid and Interface Science, 1981. 81(1): p. 285-289.

100. De Gennes, P.-G., Wetting: statics and dynamics. Reviews of modern physics, 1985. 57(3): p. 827.

101. Sadiki, M., et al., Adsorption and wetting mechanisms at the surface of aqueous hydrocarbon solutions as a possible source of atmospheric pollution. Oil & Gas Science and Technology-Revue de l'IFP, 2006. 61(5): p. 661-676.

102. Loret, B., Fluid Injection in Deformable Geological Formations: Energy Related Issues. 2018: Springer.

103. Li, S.-L., et al., New observations and insights into the morphology and growth kinetics of hydrate films. Scientific reports, 2014. 4: p. 4129.

104. Thoutam, P., et al., Comparative Analysis of Hydrate Nucleation for Methane and Carbon Dioxide. Molecules, 2019. 24(6): p. 1055.

105. Hardy, S., A grain boundary groove measurement of the surface tension between ice and water. Philosophical Magazine, 1977. 35(2): p. 471-484.

Chapter 6. Conclusions and Contributions to Original Knowledge

6.1. Conclusions

We used accurate and efficient computational simulations in combination with analytical theory to calculate the interfacial tension and supersaturation as the main factors in methane hydrate formation process according to the classical nucleation theory (CNT). We employed deterministic molecular dynamics (MD) techniques to characterize thermodynamic and mechanical properties at the bulk and interfacial regions. We found that the interfacial tension at water-gas interface decreases with temperature, while the tension at hydrate-water interface increases with temperature. The effect of temperature on hydrate-gas interface is infinitesimal. The pressure change follows the classical thermodynamic behavior so that the interfacial tension of all these interfaces decreases with pressure. We concluded the ranked order of film-shaped, cap-shaped, lens-shaped, and homogeneous in the nucleation process. We postulated that the presence of an intermediate liquid-like layer at the hydrate-gas interface works in favor of the formation at the liquid-gas interface compared to the solution's bulk. However, a negligible difference in the interfacial energy contribution between lens-shaped and homogeneous formations specifies that the high concentration of gas and water molecules at the interface is the main reason underlying the lens-shaped clustering in the formation process of methane hydrates. The significance is that we provided large amount of genuine information pertaining to insufficient database of hydrate formation and surface science. Moreover, we discovered anomalous interfacial molecular behaviors in water/hydrate/ gas mixtures. More importantly, we found the most probable hydrate nucleation dictated by interfacial energy contributions, which can be considered for production of more economical and efficient inhibitors or promoters. In the following sections, we summarize the chapters 2 to 5 to more elaborate the main conclusions of this thesis.

6.1.1. Molecular Dynamics Characterization of Temperature and Pressure Effects on the Water-Methane Interface

In this work, we used molecular dynamics to characterize the interfacial mechanics, thermodynamics, and chemical composition of liquid water and methane gas interface. Given the chemical asymmetry and mechanical anisotropy of the methane-water interface we used a novel NP_NAT ensemble, that can keep constant normal pressure and constant cross-sectional area, both crucial to obtain reliable properties in interfacial studies. As result of this computational method, this work improved the accuracy of the predicted interfacial property data, showing less deviation from experiments as well as generating a molecular-level characterization. Classical scaling laws were employed, such as the Eötvös rule in conjunction with fundamental thermodynamics to fully characterize the pressure and temperature dependence of the interfacial tension, interfacial thickness, and surface entropy, achieving good agreement with available experimental data. Results also concluded that the surface tension decreases as we increase pressure up to 50 MPa and more susceptibly, the temperature. Using the adaptive ensemble, we demonstrated that the interfacial thickness and longitudinal computational box length can elongate with either temperature increase or pressure decrease. Increasing both methane surface excess and local density near the surface suggests anomalous methane adsorption onto the water-methane surface. On the other hand, the strong hydrogen bonds adjacent to the surface in the water side favorably interact with the methane molecules and restrict them in the gas phase limiting the methane solubility, particularly at high pressure (P>10 MPa). Overall, the comprehensive results provide a quantitative characterization and molecular-level description of the water-methane interface which is of importance to fundamental surface physics and energy and environmental applications.

6.1.2. Molecular Dynamics Characterization of the Water-Methane, Ethane, and Propane Gas Mixture Interfaces

In the current study, we employed molecular dynamics simulations to investigate the interfacial thermodynamics, mechanics, and chemical composition at the interface between natural gas and liquid water. We applied a specific NP_NAT ensemble which holds the cross-sectional area and the perpendicular pressure to the planar interface constant owing to the mechanical anisotropy and chemical asymmetry of the water-natural gas interfaces. Both conditions of this ensemble are critical to achieve reliable results in surface studies. The use of such ensemble improved the accuracy of the interfacial properties such as the surface tension, and diminished the deviation between the experiments and computational methods.

The interfacial density profile, surface excess, radial pair distribution function, and chemical compositions in both phases were computed to generate molecular-level characterization. Increasing the interfacial density and excess, and the distribution of the propane, ethane, and methane molecules near the water-gas interface suggests that the surface adsorbs the gas components in order of their size while heavy alkanes reveal lower solubility into the water phase. Priority in the anomalous adsorption of large saturated hydrocarbons such as propane onto the natural gas-water surface implies that the nucleation of structure II clathrates initiated at the interface is recognized as heterogeneous formation in the classical nucleation theory. After a complete enumeration of all hydrogen bonds adjacent to the interface, we speculated that the favorable interactions between the hydrogen bonds in water phase and hydrophobic hydrocarbons in gas phase can elucidate both high adsorption and low solubility of gas molecules, particularly in high pressure regime (P>10 MPa).

The interfacial tension values were calculated and evaluated on the basis of the available experimental data. In conjunction with the computational results, we used the classical scaling laws, for example, the Eötvös rule originated from fundamental thermodynamics to fully characterize the effects of the temperature and pressure on the interfacial properties including the surface tension, thickness, and entropy. We concluded that interfacial tension decreases with an increase in the system temperature and pressure up to 50 MPa. Given the substantial hydrocarbons adsorption at the interface acting as surfactant, the interfacial tension in a natural gas-water system is more attenuated than the liquid-vapor water or water-pure methane systems at the same temperature and pressure. We employed the adaptive ensemble to capture the elongation of the longitudinal box length and interfacial thickness with either pressure drop or temperature increase.

In summary, these results comprehensively deliver a quantitative and qualitative characterization of the natural gas-water interface which is of great significance to basic surface science and emerging environmental applications.

6.1.3. Modeling and Simulation of Water and Methane Hydrate Crystal Interface

In the present work, we used molecular dynamics as a computational technique to study the mixture of liquid water and methane hydrate crystal, particularly at the interface. We calculated the potential energy and local density profile of the system at different temperatures and pressures to seek the structure-property relations. The system anisotropy required the application of a novel NP_NAT ensemble and appropriate lattice parameter equal to the methane hydrate lattice parameter to provide an accurate platform for interfacial tension calculations for a nonplanar surface, as per the mechanical definition, in order to obtain the most reliable and comprehensive molecular-level information on this important interface. We accounted for a correction based on the Shuttleworth equation to look into the elastic strain contribution to the interfacial tension. The interfacial tension showed a slight increase with temperature increase or pressure decrease from 271 K and 30 MPa, respectively, until the melting point pertaining to the methane clathrate-water phase diagram. Such a strongly anomalous temperature effect on the interfacial tension defies the standard classical behavior.

In conjunction with the computational approach, we used direct numerical simulation techniques to validate the results on the basis of available experimental data. We investigated the excess enthalpy and entropy and concluded that the molecular orientation at the interface becomes less disordered as the temperature increases. Furthermore, a series of complex calculations on the adsorption, radial pair distribution function, hydrogen bonding density, and charge distribution at the interface generated a full molecular-level characterization and confirmed the interfacial tension variation trend with the system temperature and pressure.

As we increased the temperature or decreased the pressure, the interfacial polarization charge density, minimum number of hydrogen bonds, and intermolecular attractions further perturbed the force balance at the interface and led to the interfacial tension increase. Furthermore, the interfacial water became less disordered with lower molecular rotation in comparison to bulk water, which significantly dropped the water dielectric constant near the crystal surface and, subsequently, added to the interfacial tension.

In summary, the results reported provide a sound foundation for the characterization of the water and hydrate interfaces with respect to gas hydrate formation studies. Furthermore, the discussed methods can be extended to the interfacial energy calculations of many industrial, environmental, and biological processes, which deal with the water-crystal mixtures.

6.1.4. Characterization of Nucleation of Methane Hydrate Crystals: Interfacial Theory and Molecular Simulation

The interaction of methane gas and water at low temperature and high pressure may cause methane hydrate formation. In both industrial and natural environments, the nucleation appears in the solution bulk or at the solid-liquid and liquid-gas interfaces forming different morphologies. To promote or inhibit this nucleation process, we are able to further understand the work, location, and morphology of the formation through classical nucleation theory. Therefore, we employed a combination of molecular dynamics technique and theoretical computation to obtain the formation work. The main focus is on the interfacial energy contribution in the nucleation process of methane gas hydrates that has not been well studied before, while, it has shown a big effect in the widespread applications of clathrate hydrates, specifically in flow assurance owing to the chemical composition of natural gas.

We first computed the interfacial tension at water-methane hydrate and water-methane gas interfaces, and afterwards, applied our method and Antonow's rule to find the interfacial tension at the interface between methane hydrate and the gas phase. We showed that a quasi-liquid layer was formed between the hydrate and gas phases due to the premelting process of crystalline hydrate in contact with the methane gas molecules. The existence of this thin intermediate layer causes the Antonow's rule to overestimate the interfacial tension, and consequently it cannot be used to estimate the tension values at the hydrate-gas interface. With the necessary interfacial properties at hand we then calculated the formation work and nucleation rate of methane hydrate. We concluded that the nucleation was more favorable in low temperature and high pressure regimes, and likewise, at the water-methane hydrate interface in a shape of a film or disk. The other formation morphologies in order of likely occurrence were cap-shaped, lens-shaped, and homogeneous forms of nucleation, respectively. We proposed that the existence of a quasi-liquid layer between the methane hydrate and gas surfaces causes lower formation work for the lens-shaped formation compared to homogeneous. Nonetheless, high concentration of methane gas and water molecules at the surface is found to be the leading reason of lens-shape formation as opposed to homogeneous. In addition, we demonstrated that the presence of additives in the mixture of water-methane gas reduces the nucleation rate, which inhibited the hydrate formation process. Lastly, we presented the nucleation rate employing the interfacial tension at the ice surfaces, instead of hydrate, which led to significantly larger nucleation rates. This large discrepancy prevents the usage of ice properties from estimating the interfacial energy in hydrate studies.

In summary, the reported results on different aspects of methane hydrate critically deliver a qualitative and quantitative set of information in gas hydrate formation through the characterization of the water-hydrate, water-gas, and hydrate-gas interfaces. We anticipate this work will significantly contribute to a better understanding of the kinetics of clathrate hydrate formation in different thermodynamic pressure and temperature regimes and to the many technological processes that rely on interfacial science. However, other possible morphologies of methane hydrate nucleation such as sII methane hydrate may lead to distinct interfacial structures and shape factors, and consequently, alter the conclusions of this work. Moreover, a deeper analysis on the impact of surface covering additives on the surface energy, the attachment strength, and creation of new nucleation sites is necessary for surfactants applications. In addition to the study on the interfacial energy contribution, their needs to be more work performed on the modeling of methane hydrate formation through the classical nucleation theory in regards to the supersaturation contribution into the nucleation process.

6.2. Contributions to Original Knowledge

This work properly contributed to the findings of the thermodynamics and kinetics of clathrate hydrate formation at different pressure and temperature regimes. This new series of theoretical and computational studies on different aspects of methane hydrate formation provided large amount of critical information, contributing to the current insufficient database in this area of research. The main focus is on the interfacial energy contribution in the nucleation process of methane hydrate that has not been well studied before, while, it has shown a crucial effect in the widespread applications of clathrate hydrates, specifically in flow assurance owing to the constituents of the natural gas. The output of this study has potential contributions in the environmental and economic dimensions of oil and gas industries. A summary of the contributions to original knowledge are:

- Determined the interfacial tension in a wide range of pressure and temperature at the following interfaces:
    - Methane gas-water
    - Natural gas-water
    - Methane hydrate-water
    - Methane hydrate-methane gas
- Characterized the effect of pressure and temperature on the interfacial tension by employing a sophisticated ensemble for the anisotropic interfaces.
- Computed the structure of natural gas hydrate at different system temperatures and pressures.
- Developed the mechanical definition of surface tension to calculate the elastic deformation at the crystalline hydrate surfaces using the Shuttleworth equation.
- Explicated the anomalous tension increase at methane hydrate-water interface with temperature.
- Proved the existence of a thin quasi-liquid layer between the methane gas-methane hydrate interface and discussed the significance of such layer in the hydrate formation process.
- Found the most probable location and morphology in methane hydrate formation process.
- Studied the inhibiting effect of additives on the nucleation rate of methane hydrates.

- Distinguished the difference between the ice and methane hydrate properties and highlighted the importance of such difference in hydrate formation process.

6.3. Recommendations for Future Works

While this thesis investigates the sI methane hydrate formation using precisely computed interfacial energy and characterizes the key thermodynamic properties at different scales, there is much yet to be done in this field. Therefore, we suggest possible future research in the following avenues to avoid the necessary assumptions used in this thesis:

- To determine supersaturation as a function of temperature and pressure using a combination of molecular dynamics and Monte Carlo techniques using grand canonical ensemble with no need of the imperfect experimental work regarding the cell potential parameters in order to model a real system. Such study is imperative as the experiments cannot obey all the key characteristics of gas hydrate systems. Moreover, using a general thermodynamic equation of state for methane with many assumptions, namely Peng-Robinson, does not perfectly apply to the polar compounds, particularly, water.
- To test and compare the nucleation location and morphology using a non-classical nucleation theory rather than the classical nucleation theory with a complete knowledge of the interfacial energy between the involved phases reported in this work.
- To investigate the effect of the line tension between the phases to the interfacial energy contribution of hydrate formation.
- To simulate the methane hydrate formation in large-scale to estimate a realistic shape factor instead of the assumption of perfect sphere for this factor.